Anisotropy in Reflected Solar Radiation

By
Vincent V. Salomonson

Department of Atmospheric Science
Colorado State University
Fort Collins, Colorado

The research was funded by the National Aeronautics and Space Administration
Contract No. NASr-147
Project director: Dr. William E. Marlett
August, 1968

Colorado State University

Department of Atmospheric Science

Paper No. 128

ANISOTROPY IN REFLECTED SOLAR RADIATION

by

Vincent V. Salomonson

The research described in this report was
funded by the
National Aeronautics and Space Administration
Contract No. NASr-147
Project Director: Dr. William E. Marlatt

Department of Atmospheric Science
Colorado State University
Fort Collins, Colorado
August, 1968

Atmospheric Science Paper No. 128

ABSTRACT

ANISOTROPY IN REFLECTED SOLAR RADIATION

The objective of this study was to observe in some detail the nature of the reflection process for several specific surfaces and show in the case of clouds that the reflection of solar radiation is accomplished by several processes which interact with one another to produce the observed directional reflectance distributions. The first portion of this study utilized an aircraft-mounted satellite radiometer to observe the reflected radiances over stratus clouds, white sand, snow, a dry desert lake bed, a grassland-sod surface, a swampy-dense vegetation surface, and water. The second portion of this study involved the utilization of existing scattering theory to numerically examine the influence of droplet size distribution and droplet concentrations on single scattering results representative of that occurring in the clouds over which the observations of reflected solar radiation were taken. This portion of the study also compared theoretical results involving multiple scattering with the results actually observed over stratus clouds.

Anisotropy in the reflected solar radiation was observed in varying degrees for all the surfaces studied. The anisotropy for all surfaces increased with increasing solar zenith angle. At large solar zenith angles forward scattering or reflection was the predominant feature over

stratus clouds and snow. Reflection back toward the sun was the major feature describing the anisotropy observed over soil and vegetative surfaces. The scattering from stratus clouds was observed to be a function of the thickness of the clouds and the reflectivity of the surface beneath the clouds.

The computed single scattering results were found to be most sensitive at scattering angles near 0 and 100 degrees to changes in the droplet size distribution and associated droplet concentration in a cloudy volume. It was found that multiple scattering smooths the anisotropy and other effects suggested by single scattering results. Remarkably good agreement was evident in comparisons of the anisotropy predicted by some theoretical results including multiple scattering and that actually observed over stratus clouds.

ACKNOWLEDGEMENTS

The author wishes to thank Dr. William E. Marlatt for his patience, time, and support during the time required to accomplish the research described in this report. Appreciation is also expressed to Professors Lewis O. Grant, Norman A. Evans, and Bradford R. Bean for taking the time to read and comment on the manuscript.

The professional and conscientious contributions toward acquisition of the data that were made by the pilot of the aircraft, Mr. Dwain D. Adam, are greatly appreciated. Mr. Donald W. Hill and Mr. Gary M. Cobb made essential contributions to the final results through their technical knowledge and assistance. Mrs. Sandra Olson is commended for her care and attention to detail in typing the manuscript.

The funding of this research by the National Aeronautics and Space Administration through Contract No. NASr-147 is gratefully acknowledged.

TABLE OF CONTENTS

TABLE OF CONTENTS CONTINUED

LIST OF TABLES

LIST OF FIGURES

LIST OF SYMBOLS

a = radius of a particle or droplet

a_o = positive constant in general droplet distribution

a_1, a_2 = lower and upper limits of integration over a droplet size distribution

$a_\ell^{(s)}$ = coefficient for the scattered electromagnetic field

a_m = modal droplet radius

A = area

${}^mA_\ell, {}^eA_\ell$ = coefficients for the transmitted electromagnetic field

b = positive constant in droplet size distribution

$b_\ell^{(s)}$ = coefficient for the scattered electromagnetic field

${}^eB_\ell, {}^mB_\ell$ = coefficients for the scattered electromagnetic field

$\underset{\sim}{B}$ = magnetic induction vector

c = speed of light

C_s = scattering cross section

$\underset{\sim}{D}$ = electric displacement vector

$\underset{\sim}{E}$ = electric field vector

E = amplitude of the electric field

E_ν = radiant energy

${}^eE$ = electric field component of the electric wave

${}^mE$ = electric field component of the magnetic wave

E_θ = component of the electric field vector in the θ direction

E_ϕ = component of the electric field vector in the ϕ direction

E_ρ = component of the electric field vector in the ρ direction

F = net flux

F_o = a function whose independent variable is Φ

$\mathbb{F}$ = net flux column matrix

$\underset{\sim}{H}$ = magnetic field vector

H = amplitude of the magnetic field

^{e}H = magnetic field component of the electric wave

^{m}H = magnetic field component of the magnetic wave

H_θ = component of the magnetic field vector in the θ direction

H_ϕ = component of the magnetic field vector in the ϕ direction

H_ρ = component of the magnetic field vector in the ρ direction

H_p^1 = Hankel function of the first kind

H_p^2 = Hankel function of the second kind

i = $(-1)^{1/2}$

i_1, i_2 = dimensionless intensity functions

I_ℓ = intensity component parallel to the meridional plane passing through the local vertical and the direction of propagation of the intensity vector

I_r = intensity component perpendicular to the plane defined above

I_ν = specific intensity

$\underset{\sim}{j}$ = current density vector

J_p = ordinary Bessel function

J_ν = source function

k_1 = $(\frac{i\varepsilon\omega}{c} - \frac{4\pi\sigma}{c})$

k_2 = $\frac{i\omega}{c}$

k = $-k_1 k_2$

k_o = $\frac{\omega}{c} = \frac{2\pi}{\lambda_o}$

ℓ = integer

m = integer

m_o = complex index of refraction

n = real part of the complex index of refraction

n' = absorptive or imaginary part of the complex index of refraction

$n(a), n_1, n_2, n_3$ = droplet size distributions

N = radiance observed by the radiometer

N_o = radiance observed by the radiometer when its field of view is completely filled by an ideally diffuse reflector of unit reflectivity illuminated by the solar constant at normal incidence

N_λ = spectral radiance observed by the radiometer

N' = droplet concentration in grams per cubic meter

N_p = Neumann function

p = integer

$P_\ell^m(n_o)$ = associated Legendre polynomial

P_j = intensity function for a polydispersed particulate

$p(\cos\Theta)$ = $p(\theta,\phi;\theta;\phi')$ = phase function or indicatrix

$\mathbb{P}$ = phase matrix

POL = polarization

r' = N/N_o = reflectance

r = $r'/\cos\zeta_o$ = reflectance

r_o = integrated directional reflectance

$\bar{r}$ = averaged value of reflectance

$(\bar{r})_o$ = average reflectance observed at $\theta=0^o$

R = a function whose independent variable is ρ

s = length

S = the component of the solar constant normal to the reflecting surface

S' = the total incoming energy measured by the Sol-a-meter

$S_{o\lambda}$ = solar spectral irradiance impinging upon the earth at the mean distance between the sun and the earth

S_λ = the component of $S_{o\lambda}$ normal to, and actually impinging upon the reflecting surface

$\bar{S}$ = time averaged Poynting vector

$\overline{S'}$ = flux produced by the interference of the incident and scattered radiation

$\overline{S^{(s)}}$ = scattered component of the Poynting vector

$\overline{S^{(i)}}$ = incident component of the Poynting vector

$\overline{S_R}$ = radial component of $\bar{S}$

t = time

T = a function whose independent variable is θ

U = an intensity or Stokes parameter related to the plane of polarization

U_1 = electric potential

Debye potentials

U_2 = magnetic potential

V = an intensity or Stokes parameter related to the ellipticity of polarization

W_s = total energy scattered by a sphere

x = $(2\pi a)/\lambda$ = Mie size parameter

x' = one axis of a cartesian coordinate system used in conjunction with the Mie Theory

x_1, x_2 = lower and upper limits of integration over a droplet size distribution using x as the variable of integration

Y = scalar quantity

z = one axis of a cartesian coordinate system perpendicular to a plane parallel atmosphere

z' = one axis of a cartesian coordinate system oriented parallel to the direction of propagation at the incident ray

α = a positive constant in a general droplet size distribution

α_1 = constant

β_ν = volumetric scattering coefficient

β_1 = constant

γ = a positive constant in a general droplet size distribution

ε = dielectric constant

ζ_o = solar zenith angle

$\zeta_\ell^1(z)$ = $(\frac{\pi z}{2})^{1/2} H^1_{\ell+1/2}(z)$

$\zeta_\ell^2(z)$ = $(\frac{\pi z}{2})^{1/2} H^2_{\ell+1/2}(z)$

η = cos θ

η' = cos θ'

η_o = cos Θ

θ = radiometer zenith angle or the angle of the outgoing radiation measured with respect to the outgoing normal to an element of area

θ' = zenith angle of scattered radiation

Θ = scattering angle

κ_ν = mass scattering coefficient

λ = wavelength

λ_o = wavelength in a vacuum

μ = micron (10^{-4} centimeters)

ν = frequency of electromagnetic energy

ξ = permeability

π = 3.1415926536

π_ℓ = angle dependent function in the expressions for the scattered field = $P_\ell^1(\cos\theta)/\sin\theta$

ρ = radius

ρ_o = density of scattering material

ρ' = charge density

$\bar{\rho}$ = $k\rho$

σ = electroconductivity

τ = optical depth

τ_ℓ = angle dependent function in the expressions for the scattered field = $dP_\ell^1(\cos\theta)/d\theta$

ϕ = azimuth or radiometer azimuth

ϕ_o = azimuth of the sun

Φ = azimuth in spherical coordinate system

Φ_o = an unspecified function

Φ_λ = spectral response of the MRIR

ψ = relative azimuth

ψ_ℓ = $(\frac{\pi Z}{2})^{1/2} J_{\ell+1/2}(Z)$

χ_ℓ = $(\frac{\pi Z}{2})^{1/2} N_{\ell+1/2}(Z)$

ω = field frequency

Ω	= solid angle corresponding to the incident radiation
Ω'	= solid angle corresponding to the scattered radiation
$(^{(s)})$	= designates the scattered wave
$(^{(t)})$	= designates the transmitted wave
$(^{(i)})$	= designates the incident wave
$(*)$	= designates the complex conjugate
Re	= indicates the real part of a complex quantity
$(^{(1)})$	= refers to the region outside the scattering sphere
$(^{(2)})$	= refers to the region inside the scattering sphere
$(^{0})$	= degrees

ANISOTROPY IN REFLECTED SOLAR RADIATION

INTRODUCTION

One of the most significant, but still not fully explained, occurrences that takes place in the earth-atmosphere system is the redistribution and transformation of the incoming energy from the sun. A major portion of the solar energy which impinges upon this system is reflected by terrestrial surfaces and eventually does not contribute to the various weather phenomena that are of importance to all aspects of life on earth. It was the objective of this study to observe in some detail the nature of the reflection process for several specific surfaces and show in the case of clouds that the reflection of solar radiation is accomplished by several processes which interact with one another to produce the observed directional reflectance distributions.

The first portion of this study consists of describing and interpreting reflectance observations made with an aircraft-mounted satellite radiometer over seven different types of surfaces. These observations serve to show that appreciable anisotropy in the reflected radiation does exist and that the magnitude of the reflectances varies in isolated portions of the solar spectrum depending upon the surface being observed and its spectral reflectivity. The implications of these observations will be related to the problem of determining the planetary albedo from meteorological satellite radiometers with a limited field of view.

The second portion of this study investigates the processes which produce the observed anisotropy in reflected solar radiation observed over clouds. This choice was made, first of all, because of the wide distribution of clouds throughout the earth's atmosphere and their important contribution to the planetary albedo. Secondly, the possibility of mathematically modeling a cloud, particularly a stratus cloud, and its reflection properties is much greater than for the majority of the other reflecting surfaces considered here. Furthermore, an appreciation of the processes involved in the transfer of radiant energy in a cloud is of great use to the atmospheric scientist insofar as the applicability of this knowledge to other radiative transfer situations that take place in the atmosphere is concerned.

This second portion consists of two sub-parts. The first sub-part will review the necessary and important portions of radiative transfer and electromagnetic theory that are the basis for numerical computations designed to duplicate observed scattering and absorption processes taking place in a cloudy atmosphere. In particular, the basic equation of radiative transfer, the equations for describing the diffraction of an electromagnetic wave by a sphere, and the scattering of electromagnetic energy by polydispersed particulate volumes is described and developed in some detail. The second sub-part describes and illustrates the results of numerical computations involving

single and multiple scattering. These results show the effects of varying droplet size distribution, droplet concentration, and optical depth on reflectances observed at various individual wavelengths and over a portion of the solar spectrum including several wavelengths. In particular, it is shown that the observed results do agree, in general, with published computations including multiple scattering.

In addition to the above, conclusions are drawn and brief recommendations made as to the feasibility and practicality of inferring the characteristics of a cloudy volume from the character of the scattered light. Recommendations are made as to further computations and observations that could and should be made to further verify and substantiate the results and conclusions drawn in this study.

Chapter I

MEASUREMENTS OF ANISOTROPY IN REFLECTED SOLAR RADIATION

1.1. Introduction

The weather satellite has provided meteorologists with the means whereby large portions of the earth's surface and atmosphere can be observed in a relatively short time. As satellite technology has developed, it has become increasingly evident that by using a satellite equipped with suitable radiometers, one can measure the various components of the radiative energy balance. This means that the satellite is capable of providing valuable data enabling one to determine the amount of energy available for driving atmospheric processes on time and distance scales corresponding to the meso and macro scales of motion.

One of the difficulties which has hampered progress in this realm of study is that the radiation reflected from most surfaces is not isotropic. Since the majority of satellite radiometers have a limited field of view, they cannot measure the total energy reflected from a surface in all directions at any particular moment. In order to determine the amount of energy reflected in all directions, it is necessary to either measure the energy reflected in all directions, or to make one measurement and combine it with a prior knowledge of the directional character of the reflected energy. Since present meteorological satellite systems are not capable of measuring reflected energy in all directions simultaneously, the

need for an improved knowledge of surface reflection characteristics was what originally prompted the research reported here (Study Conference on the Global Atmospheric Research Programme, 1967, pp 46-47, 65).

Bandeen, et al. (1965) used satellite measurements to estimate the albedo of the earth. In that study it was necessary to assume that the reflection from all surfaces was isotropic and independent of wavelength. When these assumptions were used, the resulting values of annual planetary albedo did not balance the corresponding reliable values of emitted thermal radiation and incoming solar radiation. Eventually it was necessary to apply a simple correction factor in order to achieve this balance. Viezee and Davis (1965) have also reported on difficulties encountered in using satellite measurements to obtain the albedo of cloudy regions. More recently Ruff et. al. (1968) have reported on a statistical analysis of TIROS IV observations that enabled them to derive reflection patterns representative of the average results from a large number of cloud observations and cloud types. All of the studies mentioned above have served to emphasize that the reflection from most surfaces is neither isotropic nor independent of wavelength. Furthermore, each indicated that the determination of the total reflected solar energy from a surface or surfaces is a very difficult task when using satellite measurements.

Coulson (1966), Coulson, et al. (1965), Hapke and Van Horn (1963), and Chen, et al. (1967) have reported on measurements made in the laboratory of anisotropically reflected radiation from soils, sands, and vegetation. Kozlov and Federova (1962) and Bartman (1967), using airplanes and balloons respectively, have measured anisotropy in solar energy reflected from cloud and snow fields. Griggs and Marggraf (1967) report on measurements of the directional reflectance characteristics of clouds, water, and snow as observed with a polarimeter mounted on an aircraft.

This chapter presents measurements made from an airplane with a radiometer originally designed for a meteorological satellite. Because of the radiometer construction and the lateral and vertical mobility of the airplane, the resulting reflectance measurements made under natural conditions cover a greater range of directions over a reflecting surface than is possible with many other instruments and means of conveyance. Results are presented and discussed for seven different surfaces: stratus clouds, snow, white gypsum sand, a dry desert lake bed, a grassland-sod surface, dense vegetation, and water. These surfaces have widely varying characteristics and are, as a result, representative of many of the terrestrial surfaces reflecting solar radiation. It was also possible to find homogeneous and uniform areas of each surface that were large enough for measurements to be made from an

airplane. It will be seen that the reflectivity is achieved in a different manner for each surface and to a varying degree in different regions of the solar spectrum.

1.2. Instrumentation

The platform used for these measurements was a Piper Twin Comanche. This airplane commonly cruises at approximately 80 meters per second and is capable of flying at altitudes up to 9000 meters.

The radiometer used for these measurements was the NIMBUS F-3 medium resolution radiometer (MRIR)[1]. Of the five channels available on the radiometer, only results from two of the channels will be discussed here. These two channels measure energy in the 0.2 - 4.0μ and 0.55 - 0.85μ portions of the solar spectrum. The 0.2 - 4.0μ channel will be referred to as the broad bandpass and the 0.55 - 0.85μ channel as the narrow bandpass. The radiometer uses a rotating aluminum mirror to scan across surfaces within the view area. The instantaneous field of view is 50 milliradians in cross-section. Energy striking the surface of the mirror is reflected into the chopper and detector systems. The manner in which the

[1]Any information provided in this dissertation pertaining to the manufacture of instruments is for the reader's information only and does not constitute endorsement by the author or his institution.

radiometer was mounted on the airplane and its direction of scan are shown in Fig. 1.2.1. A closer view of the radiometer is seen in Fig. 1.2.2. The time constant of the radiometer is 0.02 seconds.

The radiometer was built and calibrated by the Santa Barbara Research Center, Goleta, California. Several calibration curves (reflectance versus voltage) were obtained for the periods corresponding to the measurements discussed here. The method of calibration has been discussed by Bartman (1966, 1967). The measurement errors associated with a current calibration were ±2%. This excludes the errors associated with the calibration of the albedo source used in the calibration of the MRIR.

For this study, the signals produced by the radiometer were recorded on high speed strip chart recorders. The error in the recorded signal was 0.2% of a full scale reading. The response time of the recorder was 0.2 seconds.

In order to measure the incoming solar energy, a Sol-a-meter (silicon solar cell) was mounted on the top of the Piper Twin Comanche over its center of gravity. The characteristics of the Sol-a-meter are described by Selcuk and Yellott (1962) and by Dirmhirn (1967). The Sol-a-meter was calibrated against an Eppley pyrheliometer before it was mounted on the aircraft and again after it was removed. The Sol-a-meter calibration was

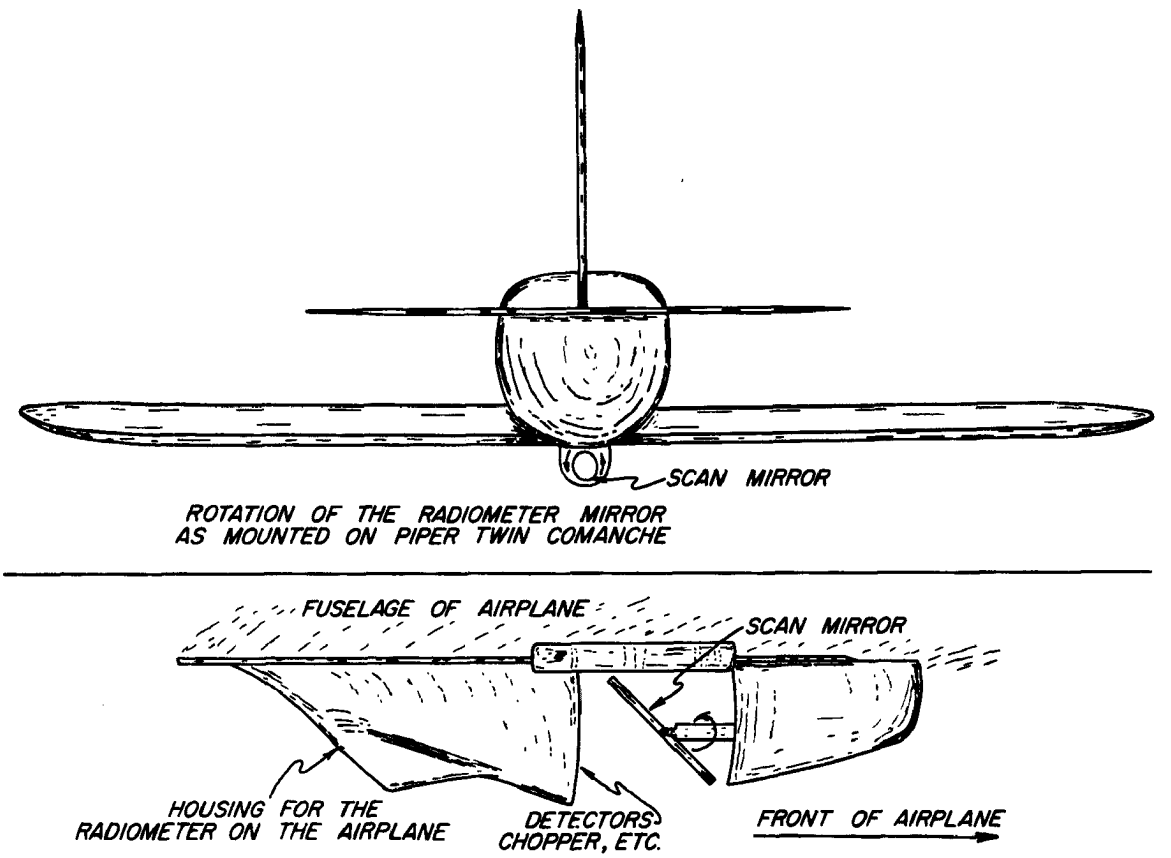

Fig. 1.2.1. A sketch showing how the Nimbus MRIR was mounted on the Piper Twin Comanche.

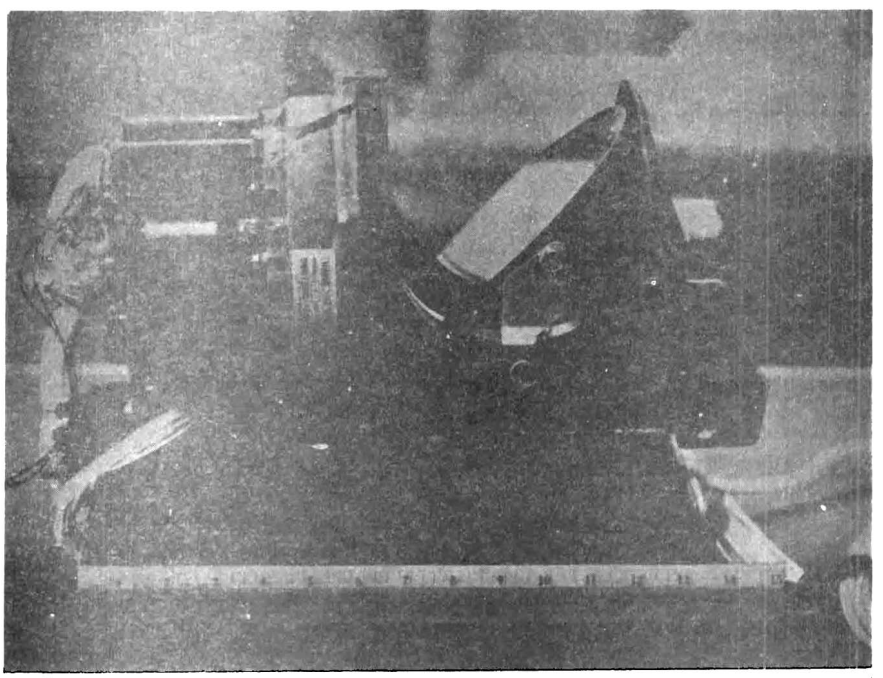

Fig. 1.2.2 Nimbus F-3 medium resolution radiometer (MRIR).

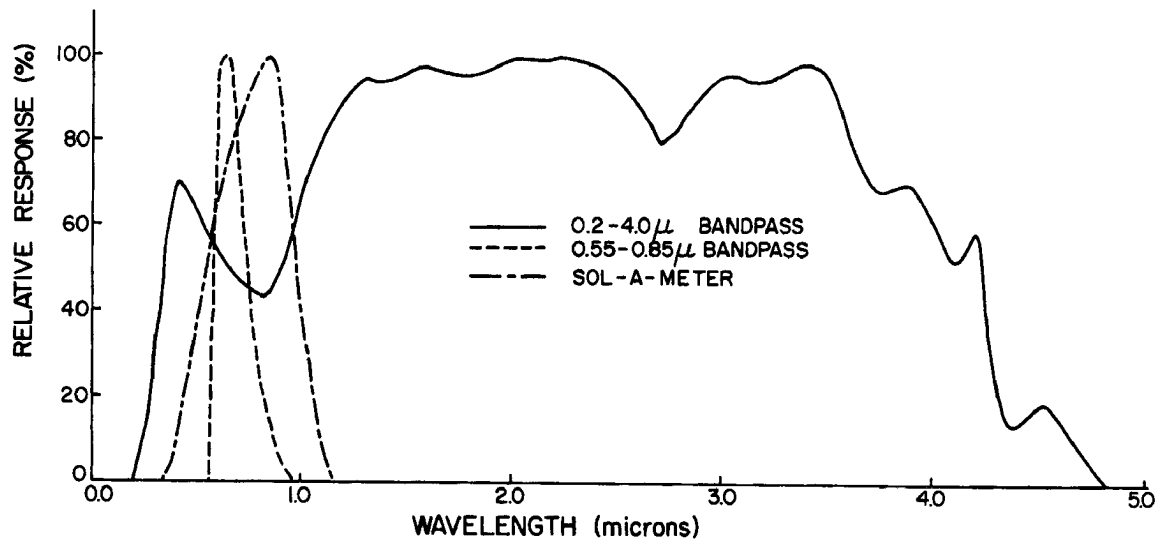

Fig. 1.2.3. Spectral response characteristics of the Sol-a-meter (silicon cell) and the two channels of the Nimbus F-3 MRIR responding to solar radiation.

also checked while it was on the airplane using a specially constructed aircraft test stand. The calibration was not observed to drift during the measurement period reported here. The estimated error associated with this instrument while mounted on the airplane was ±5%. The spectral response curves for the Sol-a-meter and the two MRIR channels are shown in Fig. 1.2.3.

1.3. Assumptions and Definitions

The radiation geometry employed in this analysis is shown in Fig. 1.3.1 along with the descriptive names applied to the various angular measurements used. The principal plane is described by AZBOA. The scattering plane is described by BOCB.

In analyzing the measurements it was assumed that the surface being viewed by the radiometer was uniform in topography and composition. It was further assumed that the scattering or reflection was symmetrical with respect to the principal plane. The actual observations showed that these assumptions were best satisfied in the cases of the dry desert lake bed and white gypsum sand. These assumptions were least approximated by the results describing reflection from a snow surface.

The calibration curves of the radiometer were based on the definition that the reflectance is the ratio of the radiance observed by the radiometer and the radiance the

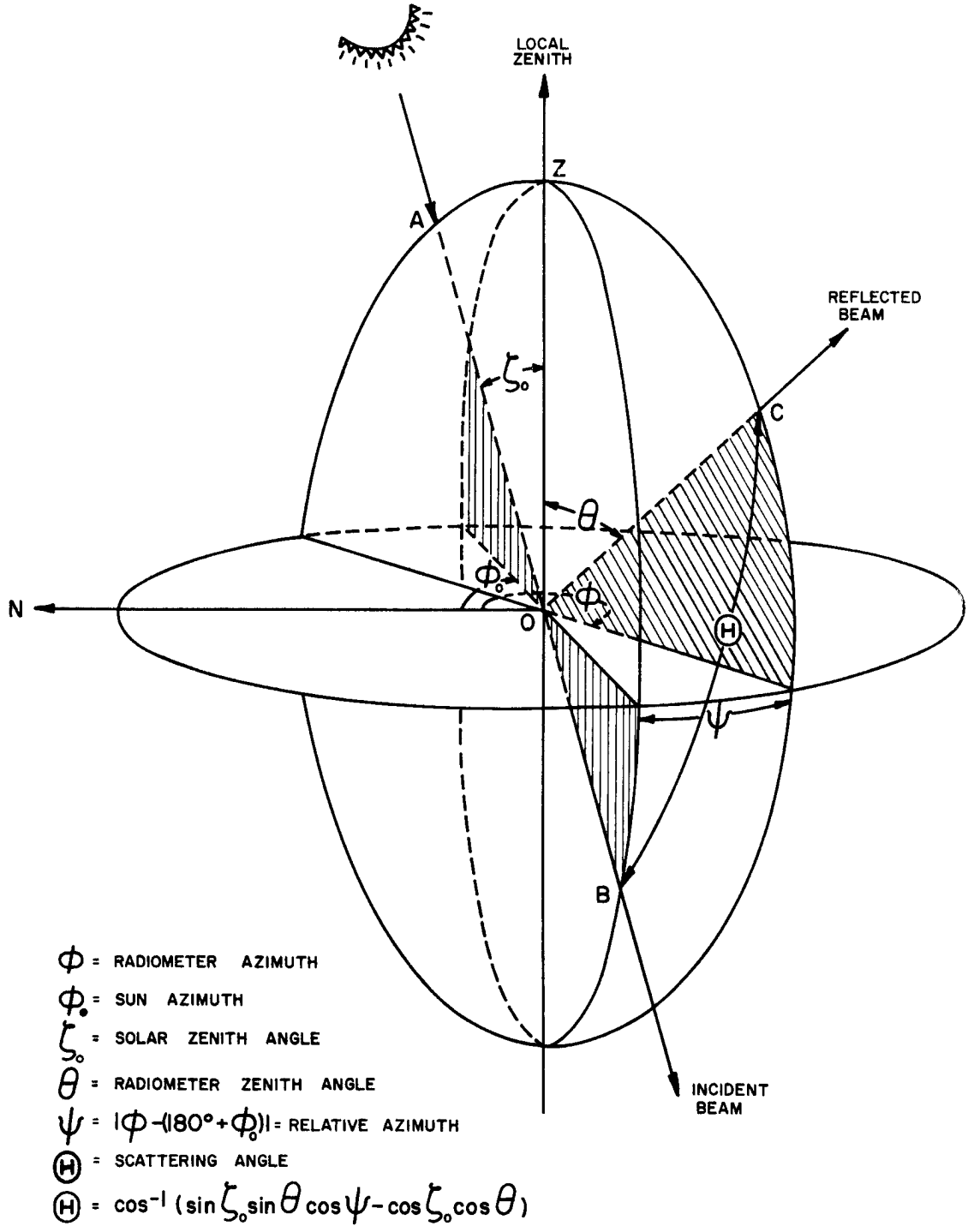

Fig. 1.3.1. Radiation geometry.

radiometer would observe if its field of view were completely filled by an ideally diffuse reflector of unit reflectivity illuminated by the solar constant at normal incidence. This relationship can be expressed as

$$r' = N(\zeta_o, \phi_o; \theta, \phi)/N_o$$

$$= \int_o^\infty N_\lambda \Phi_\lambda d\lambda / (\pi^{-1} \int_o^\infty S_{o\lambda} \Phi_\lambda d\lambda) \ . \qquad 1.3(1)$$

$S_{o\lambda}$ is the solar spectral irradiance impinging upon the earth at the mean distance between the sun and the earth. Φ_λ is the spectral response of the instrument. N_λ is best expressed as being equivalent to

$$N_\lambda = r'_\lambda(\zeta_o, \phi_o; \theta, \phi) S_\lambda \qquad 1.3(2)$$

where S_λ is the component of $S_{o\lambda}$ normal to, and actually impinging upon the reflecting surface. One can further define another reflectance that applies for any solar zenith angle ζ_o as

$$r = r'/\cos\zeta_o . \qquad 1.3(3)$$

It is also useful for checking and comparison purposes to define an integrated directional reflectance r_D that is equivalent to the albedo measured by a 2π pyranometer. This integrated directional reflectance has the mathematical form:

$$r_D = \frac{\int_0^{2\pi} \int_0^{\pi/2} N\cos\theta \sin\theta \, d\theta d\phi}{\int_0^{2\pi} \int_0^{\pi/2} N_o \cos\zeta_o \cos\theta \sin\theta \, d\theta d\phi}. \qquad 1.3(4)$$

Since N_o is an isotropic radiance, the expression above may be rewritten as

$$r_D = (\pi\cos\zeta_o)^{-1} \int_0^{2\pi} \int_0^{\pi/2} (\overline{r'}) \cos\theta \sin\theta \, d\theta d\phi. \qquad 1.3(5)$$

The bar on the reflectance $\bar{r}$ is used to indicate that it is an average of readings taken by the radiometer at various combinations of θ and ψ.

1.4. Field Measurements and Analysis

Different values of radiometer zenith angle θ were obtained through the rotation of the scanning mirror of the radiometer. Only radiometer zenith angles less than or equal to 75^o are presented so as to eliminate readings

from outside the target boundary. Different values of relative azimuth ψ were obtained by changing the heading of the aircraft at predetermined increments relative to the azimuth of the sun. For the first few flights the relative azimuth was varied in 30^{o} increments, thus requiring a total flight time of forty to fifty minutes. In later flights, the relative azimuth was varied by 45^{o} increments. This latter procedure shortened the flight time to less than thirty minutes and also reduced the variation of the solar zenith angle during each flight.

For each value of relative azimuth, the airplane was flown at a prescribed heading until the radiometer had completed ten scans. Occasionally, it was necessary to limit the number of scans to less than ten due to the limited areal extent of the surface.

Two factors were considered in choosing the flight altitude over a surface. On one hand, it was important that the reflecting surface fill the field of view for $\theta \leq 75^{o}$. On the other hand, it was desired that the radiometer field of view integrate over as much of the surface as possible. Over surfaces with limited areal extent the second factor was compromised in favor of the first. Flight altitudes of the aircraft above the surfaces varied from 120 meters over a snow surface to 1200 meters over stratus clouds. This means that when $\theta=0^{o}$, the instantaneous field of view ranged roughly in diameter from 6 to 60 meters.

Once the signal from the radiometer was recorded on an analog strip chart, it was then necessary to obtain reflectance values r' corresponding to predetermined increments of θ. Through the use of an overlay grid, the appropriate values of reflectance were obtained from the analog voltage trace on a strip chart for every fifteen degrees of radiometer mirror rotation (radiometer zenith angle). The position of the mirror was determined from a pulse generated on the analog trace by a small light installed in the radiometer housing at $\theta=180^{o}$. The recorded voltages were converted by computer to reflectance and the average, maximum, minimum, and standard deviation values determined for each pass of the airplane over the reflecting surface. The range in average values at particular values of θ and ψ for successive passes over the same area gives an indication of the relative uniformity of the results that have been obtained. Representative values of this parameter will be given for each flight discussed.

An analysis of errors involved revealed that the total error in r' is ±3%. This figure includes the error associated with the recorders (0.2%), radiometer (2%), obtaining reflectance values from the recorder trace (0.3%), and reading the calibration curves (0.5%). Where large variations in the reflectance occurred rapidly, particularly for $\theta>60^{o}$, the error is somewhat larger due to the difficulty

in determining the exact value of reflectance corresponding to a particular value of ζ_o.

The error in r is strongly dependent on the error in the determination of the solar zenith angle. For an error of $\pm 1^o$ in any individual estimate of ζ_o, the error ranges from $\pm 3\%$ at $\zeta_o = 0^o$ to $\pm 23\%$ at $\zeta_o = 80^o$. During a flight the solar zenith angle varied from $1-10^o$ depending on the time required to complete the flight and the time of day. The reflectances were computed using the solar zenith angle appropriate for each separate pass of the airplane over the reflecting surface. The time required for each pass was approximately 1.5 minutes.

To obtain a value of integrated directional reflectance (r_D) for each flight over a particular surface, it was necessary to use a finite differencing procedure that would utilize reflectance measurements taken at fifteen degree increments in θ and thirty or forty-five degree increments in ψ over the 2π steradians above each surface. As an example, the finite differencing procedure used for 45^o increments in ψ will be given. Eq. 1.3(5) was broken into three integrations and then into summations in order to arrive at the final value of integrated directional reflectance. In the equations below $\theta = 0^o$, $\theta = 15^o$, ..., $\theta = 90^o$.

$$r_D = (\pi\cos\zeta_o)^{-1} \quad \{\int_o^{2\pi}\int_o^{\pi/24} (\overline{r'})\cos\theta\sin\theta\, d\theta d\psi$$

$$+ \int_o^{2\pi}\int_{\pi/24}^{11\pi/24} (\overline{r'})\cos\theta\sin\theta\, d\theta d\psi$$

$$+ \int_o^{2\pi}\int_{11\pi/24}^{\pi/2} (\overline{r'})\cos\theta\sin\theta\, d\theta d\psi \}$$

$$= (\pi\cos\zeta_o)^{-1} \{(\overline{r'})_{\theta=o}\{\pi\sin 2\theta\}_o^{\pi/24} \qquad 1.4(1)$$

$$+ \sum_{i=1}^{8}\sum_{j=2}^{6} (\overline{r'_{ij}})(\cos\theta_j)(\sin\theta_j)(\pi/4)(\pi/12)$$

$$+ \sum_{i=1}^{8} (\overline{r'_{i7}})\cos(23\pi/48)\sin(23\pi/48)(\pi/4)(\pi/24)\}.$$

1.5. Results of Field Measurements

Table 1.5.1 lists the flights made over various reflecting surfaces. Four flights made over a water surface are not listed here because of special difficulties with the measurements. These difficulties will be discussed in the next section. All flights were made under as clear a sky condition as possible. On a few occasions some

TABLE 1.5.1. A SUMMARY OF FLIGHTS AND ASSOCIATED CONDITIONS MADE OVER DIFFERENT REFLECTING SURFACES.

(1)	(2)	(3)	(4)	(5)	(6)	(7)	(8)
FLIGHT NO.	SURFACE	DATE	LOCATION	TIME(LST)	FLIGHT ALT. (meters MSL)	HT. ABOVE SURFACE (m.)	THICKNESS OF CLOUDS (m.)
1	STRATUS	11 JUNE 1965	SAN FRANCISCO, CAL. 37°49'N., 122°35'W.	0646-0734	850	305	335
2	STRATUS	11 JUNE 1965	SAN FRANCISCO, CAL. 37°49'N., 122°35'W.	1146-1226	790	305	150
3	STRATUS	17 JULY 1965	SAN FRANCISCO, CAL. 37°49'N., 122°35'W.	0754-0840	820	304	350
4	STRATUS	17 JULY 1965	SAN FRANCISCO, CAL. 37°49'N., 122°35'W	1137-1225	760	305	240
5	STRATUS	14 DEC. 1966	BAKERSFIELD, CAL. 35°20'N., 119°5'W.	1127-1148	1850	610	850
6	STRATUS	14 DEC. 1966	BAKERSFIELD, CAL. 35°20'N., 119°5'W.	1352-1415	1850	610	850
7	STRATUS	15 DEC. 1966	BAKERSFIELD, CAL. 35°20'N., 119°5'W.	0818-0839	2150	1200	600
8	STRATUS	16 DEC. 1966	LOGAN, UTAH 41°40'N., 111°53'W.	1031-1114	2000	305	150
9	SNOW	10 DEC. 1966	LARAMIE, WYO. 41°00'N., 105°45'W.	0750-0818	2600	120	---
10	SNOW	10 DEC. 1966	LARAMIE, WYO. 41°00'N., 105°45'W.	1040-1112	2600	120	---
11	SNOW	16 DEC. 1966	LOGAN, UTAH 41°40'N., 111°53'W.	1031-1114	2000	610	---
12	WHITE SAND	15 AUG. 1965	ALAMAGORDO, N.M. 33°33'N., 106°20'W.	1120-1153	1500	305	---
13	WHITE SAND	29 OCT. 1966	ALAMAGORDO, N.M. 33°33'N., 106°20'W.	0706-0749	1550	305	---
14	WHITE SAND	29 OCT. 1966	ALAMAGORDO, N.M. 33°33'N., 106°20'W.	0917-0946	1550	305	---
15	WHITE SAND	29 OCT. 1966	ALAMAGORDO, N.M. 33°33'N., 106°20'W.	1155-1231	1550	305	---
16	WHITE SAND	30 OCT. 1966	ALAMAGORDO, N.M. 33°33'N., 106°20'W.	0913-0939	1550	305	---
17	DESERT LAKE BED	15 DEC. 1966	BRISTOL LAKE, CAL. 34°27'N., 115°40'W.	1234-1257	640	460	---
18	DESERT LAKE BED	15 DEC. 1966	BRISTOL LAKE, CAL. 34°27'N., 115°40'W.	1445-1504	640	460	---
19	GRASSLAND	4 NOV. 1965	BRIGGSDALE, COLO. 40°41'N., 104°22'W.	1215-1241	3960	2320	---
20	GRASSLAND	4 NOV. 1965	BRIGGSDALE, COLO. 40°41'N., 104°22'W.	1253-1316	3050	1400	---
21	GRASSLAND	4 NOV. 1965	BRIGGSDALE, COLO. 40°41'N., 104°22'W.	1337-1354	1680	30	---
22	GRASSLAND	25 NOV. 1966	BRIGGSDALE, COLO. 40°41'N., 104°22'W.	0845-0911	3050	1370	---
23	GRASSLAND	25 OCT. 1966	BRIGGSDALE, COLO. 40°41'N., 104°22'W.	0434-0957	2290	610	---
24	GRASSLAND	25 OCT. 1966	BRIGGSDALE, COLO. 40°41'N., 104°22'W.	1606-1630	3050	1370	---
25	VEGETATION -SWAMP	6 JAN. 1967	TALLAHASSEE, FLA. 29°55'N., 84°52'W.	1039-1109	350	350	---
26	VEGETATION -SWAMP	6 JAN. 1967	TALLAHASSEE, FLA. 29°55'N., 84°52'W.	1555-1617	350	350	---

thin cirrus was present, but only on flights 6 and 16 was a thin veil of cirrus observed that obscured the sun.

Columns 5-7 of Table 1.5.1 give the altitude (above mean sea level) of the aircraft, the height of the aircraft above the reflecting surface, and the thickness of the cloud layer. For all the surfaces except stratus clouds the height of the reflecting surface was determined from topographic maps. The altitude of the cloud tops was usually determined by the aircraft altimeter. The thickness of the clouds was commonly determined by knowing the height of the top of the clouds and the height of the bases as reported by nearby weather stations. In the case of stratus clouds over water (11 June and 17 July 1965), one penetration of the cloud layer was made by the aircraft during each flight and the height of the top and bottom of the layer determined from the aircraft altimeter. This was not done for stratus clouds over land due to the low altitudes involved.

The first four flights over stratus clouds were made directly west of San Francisco from 10-30 miles offshore. Three flights were made southwest of Bakersfield, California, over stratus clouds lying in the San Joaquin Valley. The estimated thickness of the stratus clouds is given in Column 8 of Table 1.5.1. The variation in flight altitude above the reflecting surface shown in Column 7 for flights 5 and 6 versus 7 was due to a change in the topography

of the surface of the clouds during the intervening time period. In the intervening time the clouds were under the influence of moderate winds for several hours. This windy condition served to dissipate some of the cloud layer and roughened the surface into a "frothy, whipped cream" appearance. The flight altitude was subsequently raised to allow the radiometer to integrate over as much of the surface as possible and reduce the effect that the roughened cloud surface would have on the recorded reflectance measurements.

Flights 8 and 11 were made in the Cache Valley in northern Utah. They were made under identical atmospheric conditions over locations separated by only a few miles. The northern end of the valley and the town of Logan, Utah, were covered by a layer of stratus clouds approximately 150 meters thick underlain by snow that had been deposited two days before. These flights provided an unusual opportunity for comparative measurements of snow and clouds. The flights near Laramie, Wyoming, were made over snow deposited one day prior to the observations. The homogeneous area of snow was somewhat small; therefore, a low flight altitude of 120 meters above the surface was chosen.

All the flights over white sand were made over the area included in the White Sands Missile Range west of Alamogordo, New Mexico. The majority of flights were made on the west side of the area covered by the white sand. This location was selected because of a more

uniform terrain in this section of the range. The dunes to the south and east of this area were approximately 7 to 10 meters high and oriented northwest-southeast perpendicular to the prevailing winds from the southwest.

Bristol Dry Lake is located northeast of Twenty-nine Palms, California, approximately 20-25 miles. The lake bed is approximately ten miles long and five miles wide oriented northwest-southeast. A salt-mining operation is located on the northern half of the lake. The measurements reported here were taken on the southern end of this lake bed. The height of the airplane above the surface was selected as 460 meters because at this height turbulence which affected the aircraft was not so objectionable as at lower altitudes and the altitude criteria mentioned earlier could still be satisfied.

The grassland-sod surface was located on the Pawnee National Grassland in northeastern Colorado. This surface was comprised of short native grama and buffalo grasses that were sparse enough that small areas of bare soil were still visible. Because of this condition, the measurements were an integrated result comprised of the vegetation and soil surfaces. The altitudes of the flights were varied so as to ascertain whether some variation in reflectance was attributable to a change in flight altitude. This point will be discussed in the next section.

The swampy, dense vegetation surface was located southwest of Tallahassee and east of Panama City, Florida.

Although the area was very swampy, the reflecting surface was completely composed of vegetation. These results are subsequently representative of those to be expected from vegetation as opposed to the dry desert lake bed which was devoid of any vegetation.

Figs. 1.5.1-3 show reflectance distributions observed over stratus clouds at three different locations under differing conditions of illumination and underlying surface. Fig. 1.5.4-8 show representative results for the remaining surfaces when the solar zenith angle was near 60^{o}. These last figures were chosen in this way so as to establish a clearer basis for comparison. Similar figures are in the appendix for all the flights in Table 1.5.1 that are not shown in this chapter. Parts (a) and (b) of each of the figures mentioned above show the ratio of the reflectance $\bar{r}$ at prescribed intervals of θ and ψ to the reflectance observed at $\theta=0^{o}$ designated as $(\bar{r})_{o}$. Part (c) of each figure shows the variation of $\bar{r}$ for $\theta \leq 75^{o}$ in the principal plane. The number of readings comprising each plotted point, other than $\theta=0^{o}$, is given also in part (c). The range given is the difference in the average values of reflectance obtained from successive passes over the reflecting surface.

In Table 1.5.2 data and results are listed which serve to summarize some of the important points to be discussed in the next section. Column 4 gives the incoming solar energy as measured by the Sol-a-meter

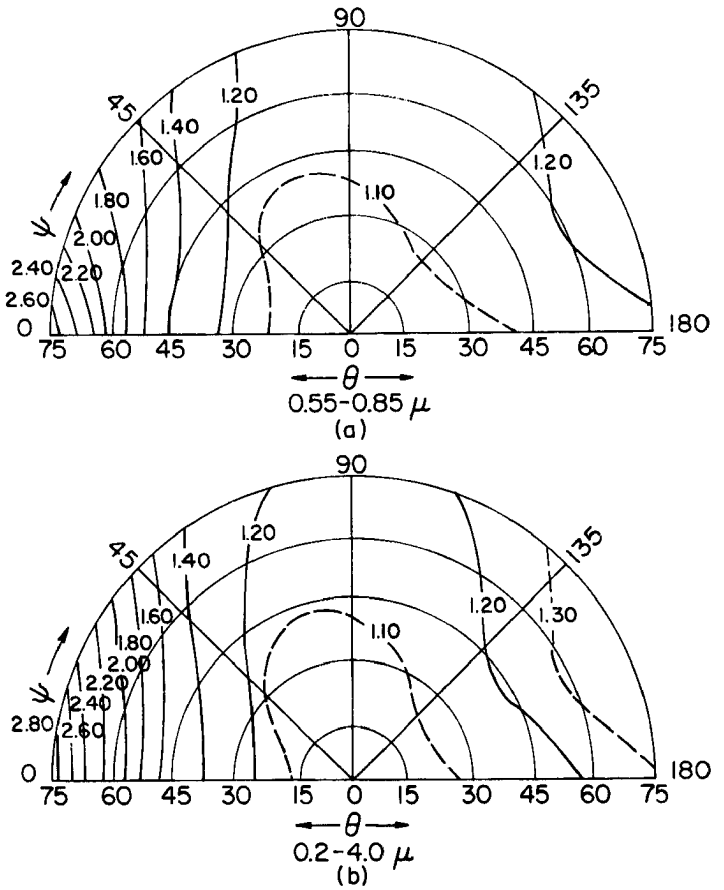

Fig. 1.5.1. Reflectances over stratus clouds near San Francisco, California, on 17 July 1965, 0754-0840 PST (ζ_o =45-54°), showing the hemispheric variation of $\bar{r}/(\bar{r})_o$ versus relative azimuth ψ and radiometer zenith angle θ for the wavelength intervals 0.55-0.85μ(a), and for 0.2-4.0μ(b). Part (c) shows $\bar{r}$ versus θ in the principal plane.

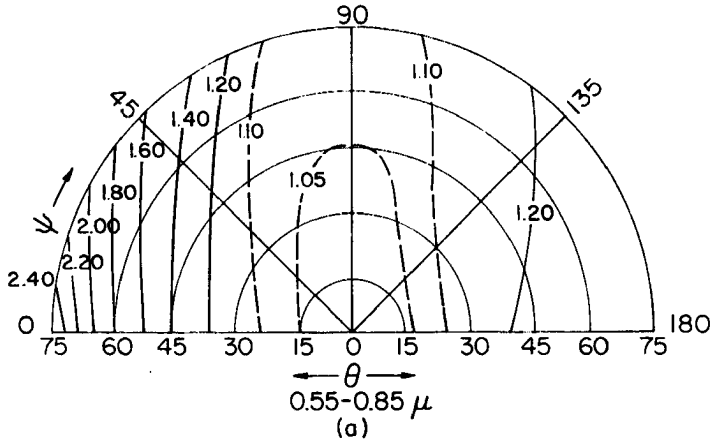

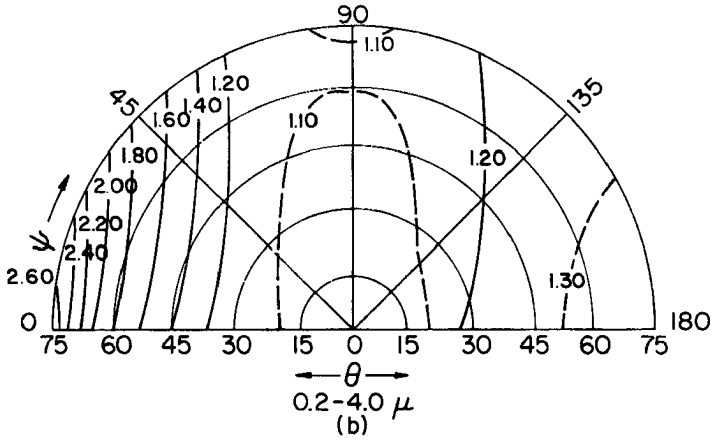

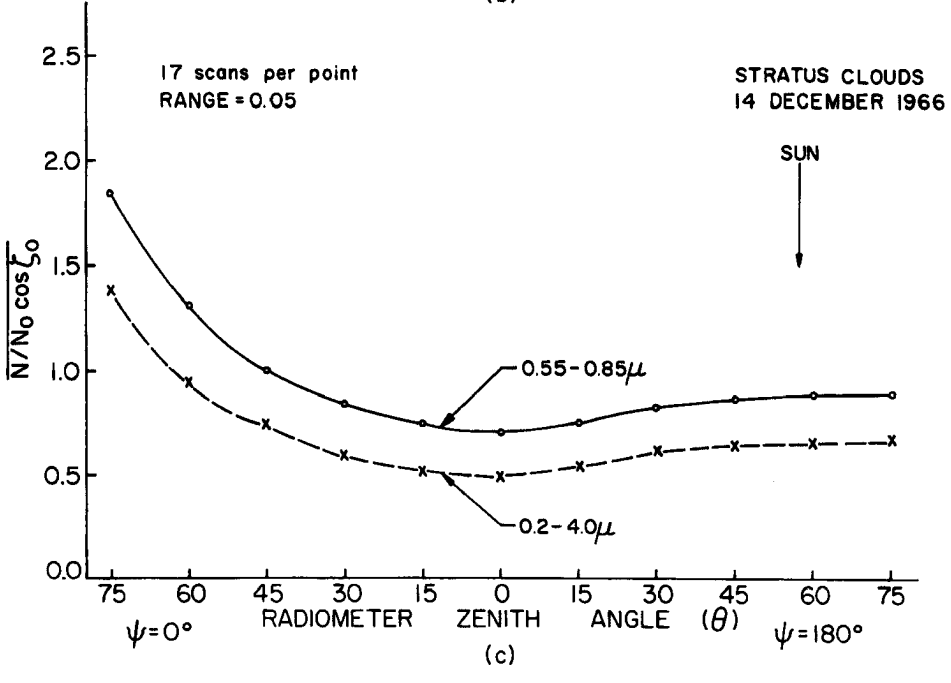

Fig. 1.5.2. Same as Fig. 1.5.1 except that the reflectances are over stratus clouds near Bakersfield, California, on 14 December 1966, 1127-1148 PST (ζ_0=57-58°).

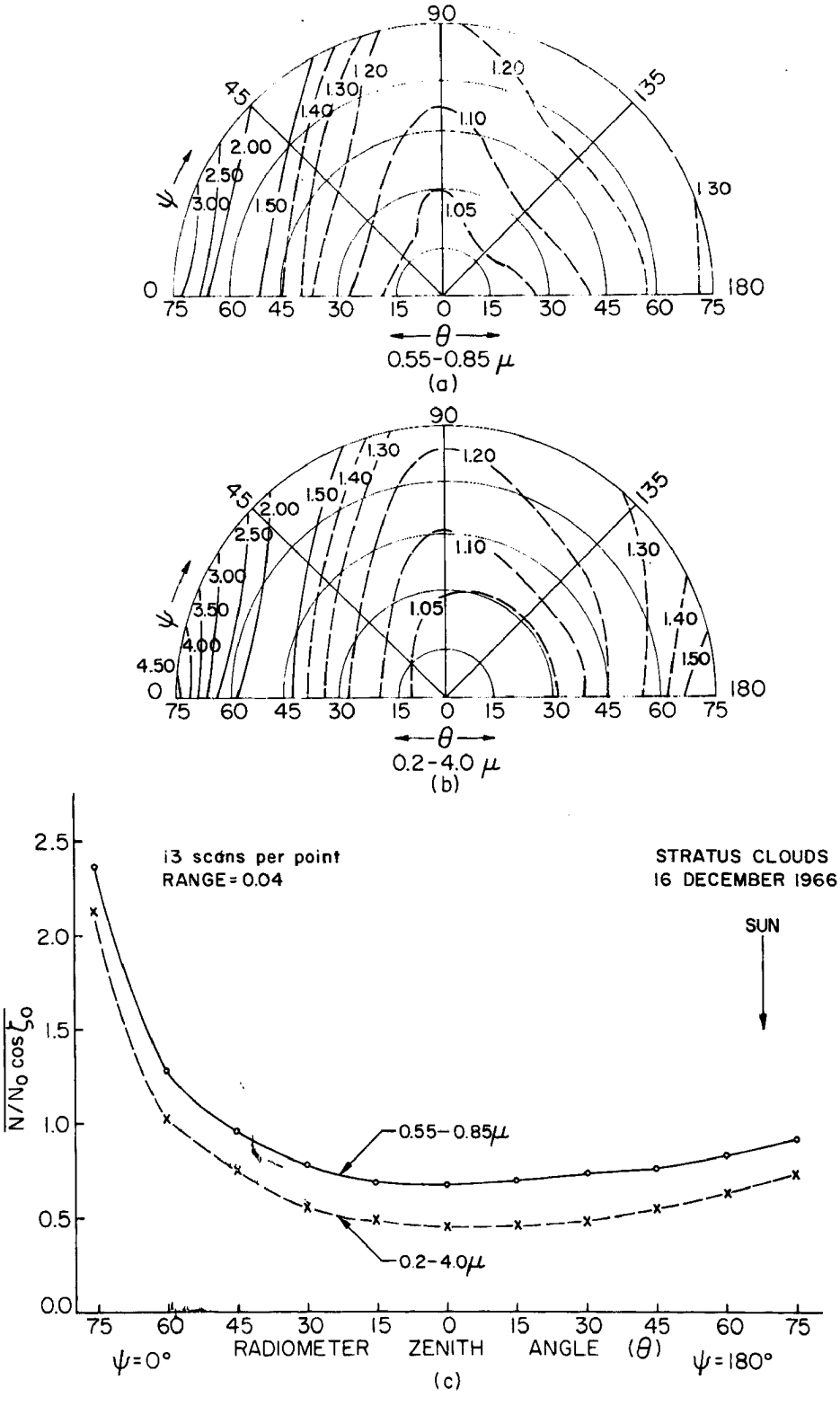

Fig. 1.5.3. Same as Fig. 1.5.1 except that the reflectances are over stratus clouds near Logan, Utah, on 16 December 1966, 1031-1114 MST (ζ_o=66-70^0).

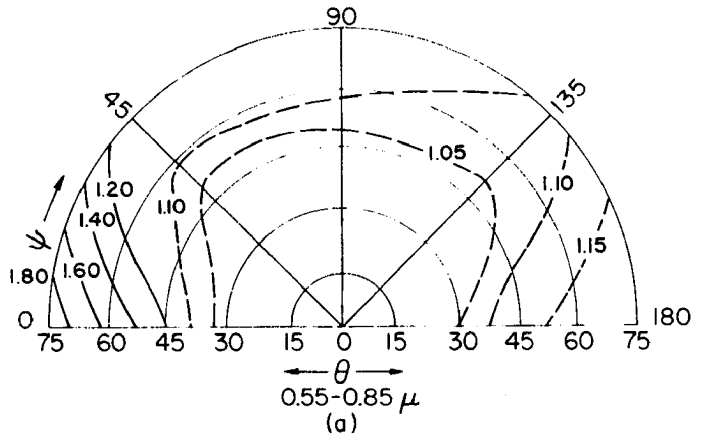

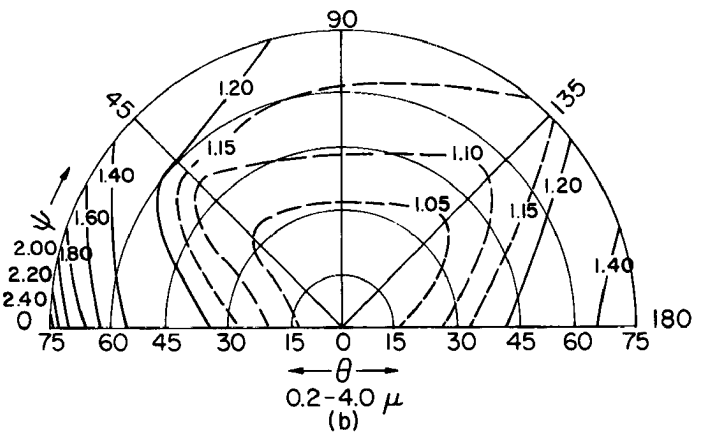

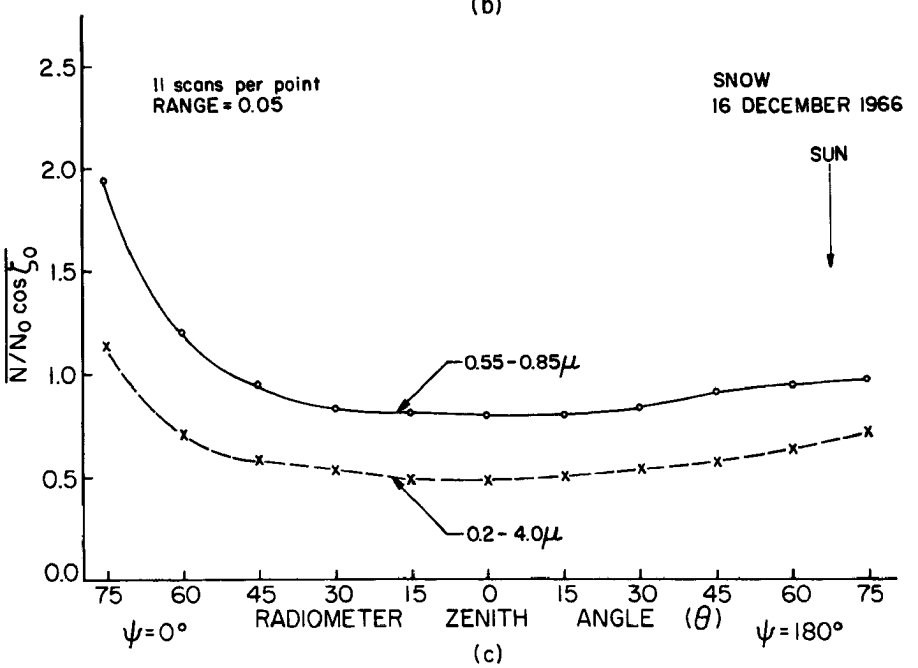

Fig. 1.5.4. Same as Fig. 1.5.1 except that the reflectances are over snow near Logan, Utah, on 16 December 1966, 1031-1114 MST (ζ_0=66-70^0).

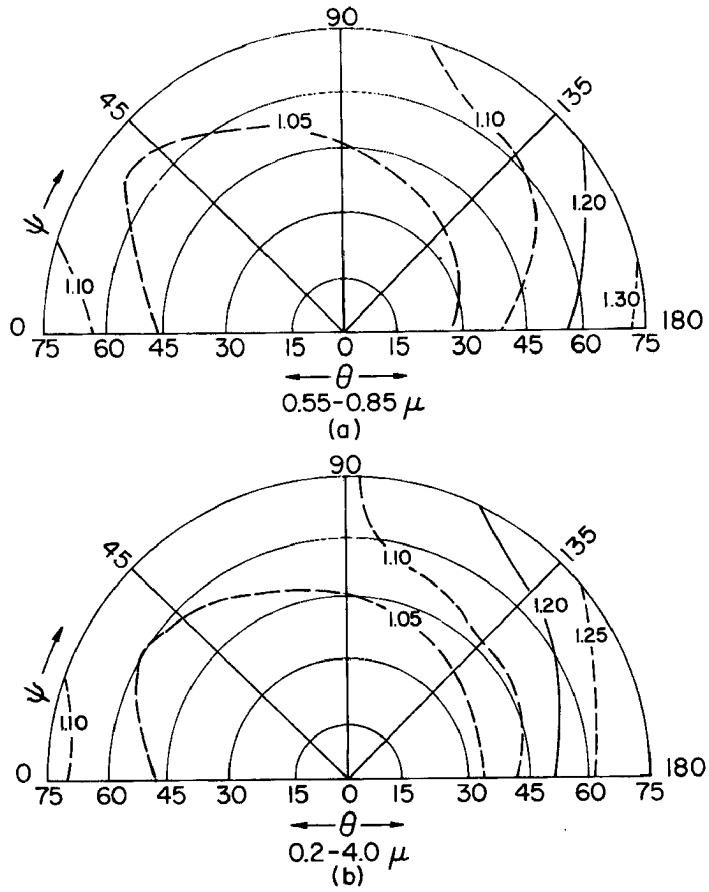

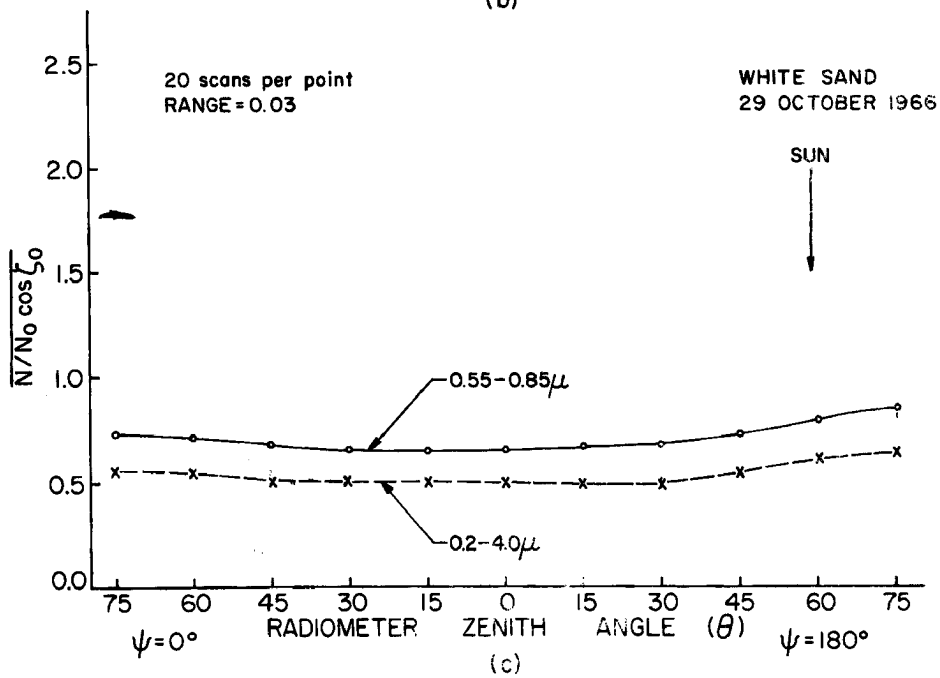

Fig. 1.5.5. Same as Fig. 1.5.1 except that the reflectances are over white gypsum sand near Alamogordo, New Mexico, on 29 October 1966, 0917-0946 MST (ζ_o=57-61°).

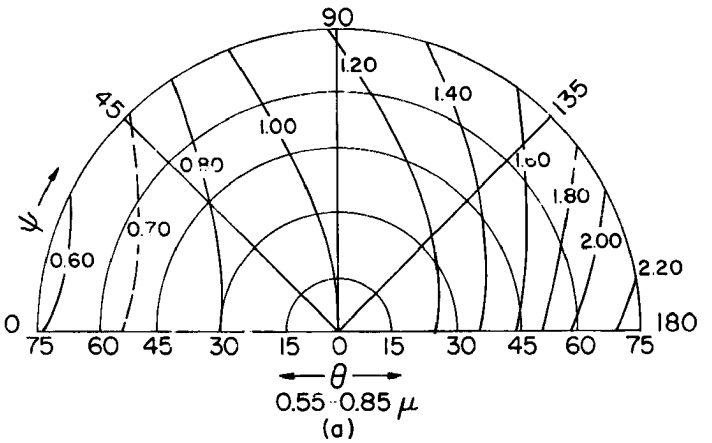

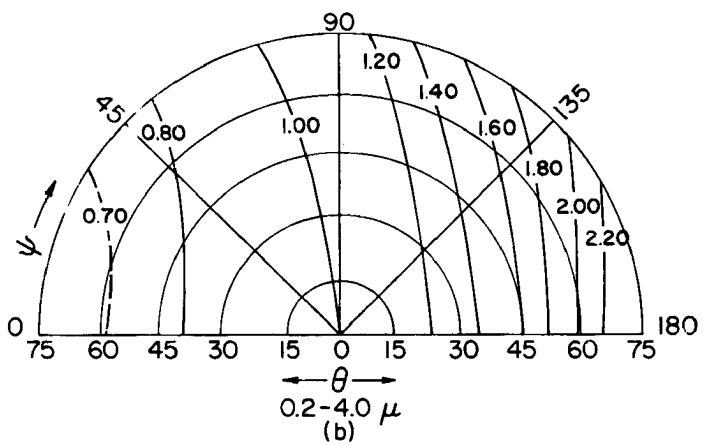

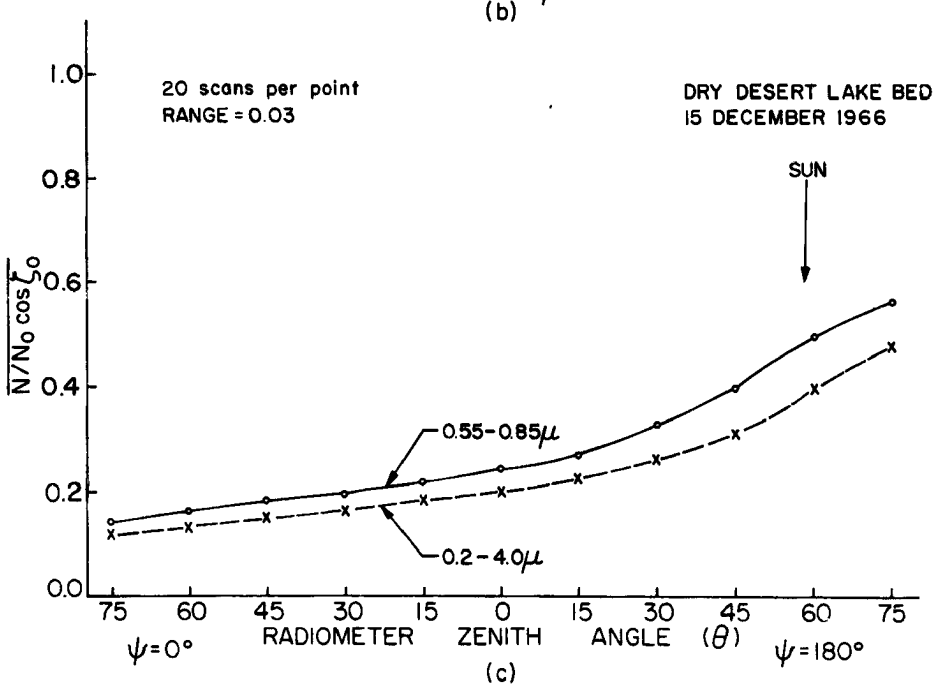

Fig. 1.5.6. Same as Fig. 1.5.1 except that the reflectances are over Bristol Lake, northeast of Twenty-nine Palms, California, on 15 December 1966, 1234-1257 PST (ζ_0=58-59°).

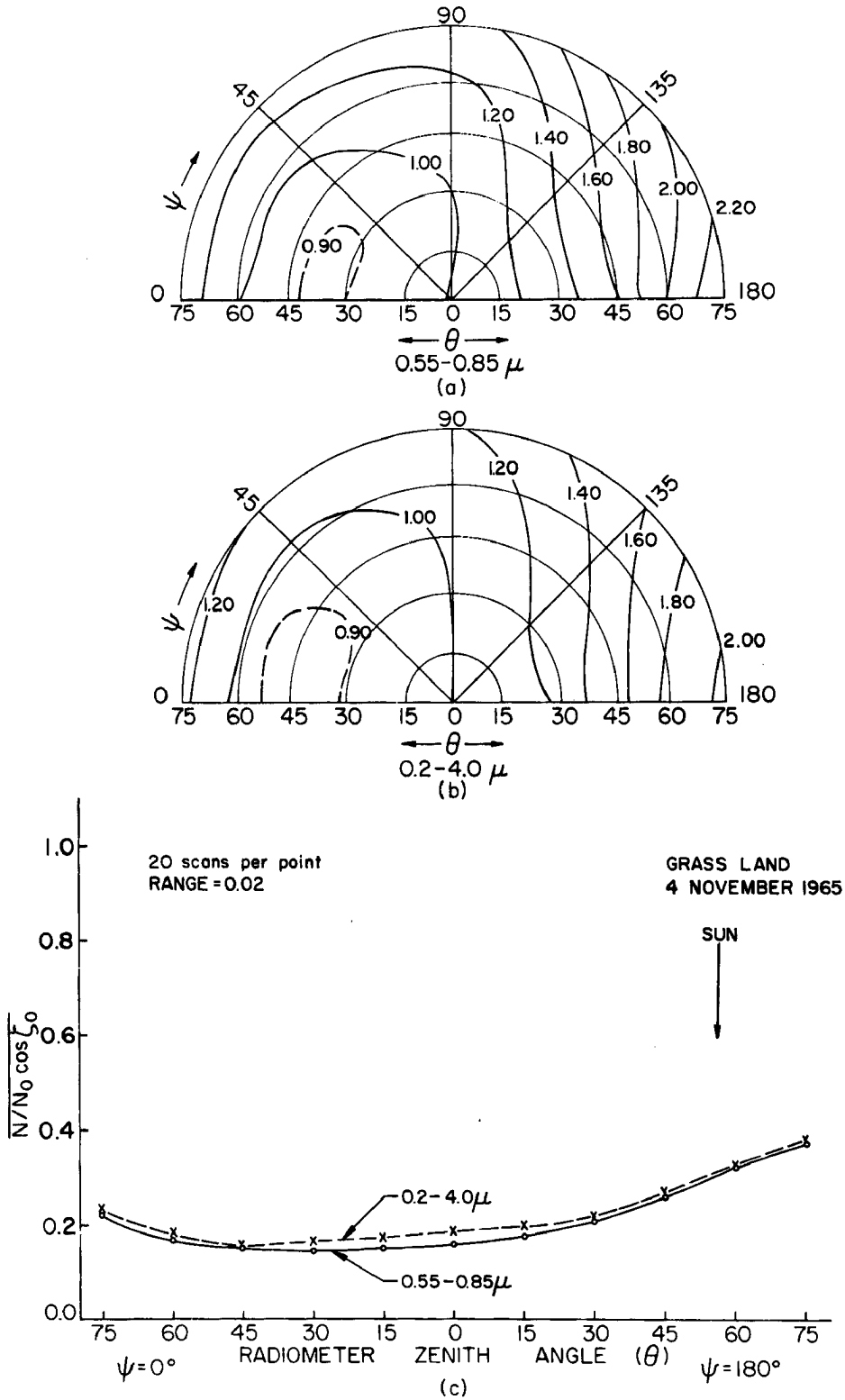

Fig. 1.5.7. Same as Fig. 1.5.1 except that the reflectances are over a grassland-sod surface near Briggsdale, Colorado, on 4 November 1965, 1215-1241 MST (ζ_0=59-63°).

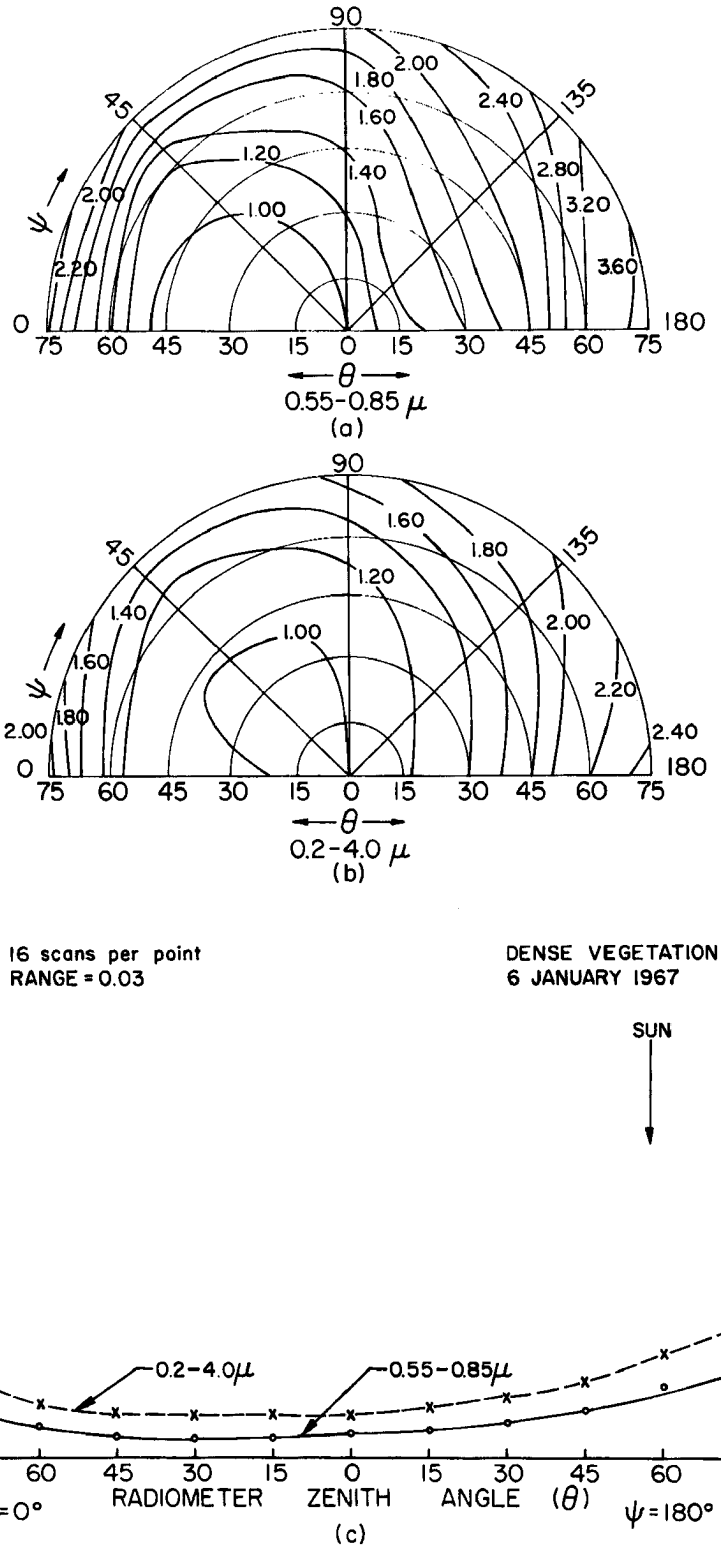

Fig. 1.5.8. Same as Fig. 1.5.1 except that the reflectances are over a swampy, dense vegetation surface near Tallahassee, Florida, on 6 January 1967, 1039-1109 EST (ζ_0=56-61°).

at the top of the airplane. These values of incoming energy were used to correct the integrated directional reflectance values measured in the broad bandpass (Column 7) for the effect of atmospheric attenuation. This correction is necessary in that the broad bandpass reflectances are derived from a comparison to values resulting when the energy in the incident beam is equivalent to the solar constant. Furthermore, the values are affected by the differences in the attenuating air mass at different locations. The correction can mathematically be expressed as

$$\text{corrected } (r_D)_B = (S/S')\ (r_D)_B \ . \qquad 1.5(1)$$

The results are given in Column 9. S' is the total incoming energy measured by the Sol-a-meter and S is the normal component of the solar constant. For solar zenith angles exceeding 70^o, the Sol-a-meter measurements are not reliable and are not presented. Other missing data in Columns 7 and 9 resulted from the Sol-a-meter being inoperative.

Columns 6 and 8 give the ratio of the integrated directional reflectance to the average value of reflectance observed at $\theta=0^o$. These results give an idea of the error that one could make in an estimate of albedo utilizing only one reading of reflectance of the MRIR at one radiometer zenith angle ($\theta=0^o$) and ignoring the anisotropy in reflected solar radiation. This ratio will be referred to

as the relative anisotropy. Values of $r_D/(\bar{r})_o$ are given for both the broad and narrow bandpasses. $(\bar{r})_o$ represents an average of as many as 130 values per flight.

Column 10 (Column 5 minus Column 7) illustrates the combined effect of atmospheric attenuation and the spectral characteristics of surface reflectivity, incoming energy, and bandpass filters on the integrated directional reflectances measured by the narrow and broad bandpasses.

1.6. Discussion of the Results

Several features in Figs.1.5.1-3 showing the observed scattering from stratus clouds are of importance. The most obvious features are the strong forward scattering and the lesser backscattering. As the solar zenith angle increases in Figs. 1.5.1-3 one can see increased reflectances in the forward direction. This result occurs because more and more of the forward scattering peak suggested by scattering theory (to be outlined in Chapter II) can be observed. The minimum reflectance occurs when the radiometer zenith angle is near zero degrees. The degree of forward and backscattering is not as large as that predicted by theoretical results involving single scattering such as those given by Deirmendjian (1964). Differences are certainly to be expected, however, since the experimental results represent integrated effects over a range of wavelengths accompanied by multiple scattering, varying drop size distribution, an varying optical thicknesses. Feigel'son (1966, chapter 2)

gives some discussion of the relative importance of these factors. Further discussion of these matters will be presented in Chapter III as the processes resulting in the observed reflectance distributions are examined in more detail. In particular, it will be shown that when multiple scattering is included, computed results agree rather well with the observed reflectances.

The reflection from the other highly reflective surfaces (snow and white gypsum sand) was not observed to be as anisotropic as that from stratus clouds. In Fig. 1.5.4 it can be seen that at a solar zenith angle between 66 and 70 degrees, the reflection from snow has a quasi-specular peak in the forward direction while the reflection in other directions tends to be isotropic. The peak in the forward direction is termed "quasi-specular" because it occurs at an angle exceeding the angle of incidence. This forward peak disappears rapidly as the solar zenith angle becomes smaller. These results are in general agreement with those of Middleton and Mungall (1952) and Griggs and Marggraf (1967).

The reflection from white sand was the most isotropic of any observed. There was a slight increase in reflection back toward the sun (Fig. 1.5.5). Only when the sun was very near the horizon was any specular component observed. These results agree in substance with those published by Chen, et al. (1967) where the reflectance characteristics of white gypsum sand were observed in a laboratory. One

difference exists, however, in that the maximum in reflectance back toward the sun in the principal plane does not occur at $\theta=\zeta_o$ as it appears to do in Chen's results. No definite explanation for this difference can be offered at this time; however, it is felt that the difference lies in the contrasting environmental conditions surrounding the two sets of measurements. The existence of a combined beam and diffuse illumination condition in the situation surrounding the measurements reported here and the illumination by a beam of light only in the laboratory case should be part of the explanation. Also the portion of the incoming solar radiation reflected by the atmosphere itself must be considered since this component has an increased influence as one scans toward the horizons (Coulson, et al., 1966). Several checks were made of the data presented here to see whether a mistake in the positioning of the reflectance curves might have been made, but no such mistake was found.

In Figs. 1.5.6-8 one can observe the changes in reflectance observed for surface conditions which go from a surface without any vegetation to a surface completely covered by vegetation. In all cases the predominant feature is increased reflection back toward the sun. The minimum for all surfaces occurs in the principal plane in the $\psi=0^o$ direction going from a radiometer zenith angle near 75^o in the case of a dry desert lake bed to an angle near 30^o in the dense vegetation-swamp condition.

This occurrence can be described qualitatively as a shadow effect that appears to be related to the size of the elements creating the reflection.

The results over the dry desert lake bed are particularly noteworthy in that the reflection back toward the sun was very noticeable even when observed with the naked eye or in photographs taken at various angles with respect to the sun. Although there is some resemblance, these results should not be construed as typical of a desert condition. It is felt that the degree of reflection back toward the sun in this case is more than that to be expected over desert sand. A desert sand reflectance distribution would be more likely to have a minimum in reflectance nearer $\theta=0^{o}$ and a less pronounced increase in reflectance back toward the sun.

In Table 1.5.2 the results given in Column 9 will be discussed first. As pointed out earlier in the chapter, the spectral response of the Sol-a-meter lies in a narrow band from 0.3-1.15μ. The Sol-a-meters are commonly calibrated against an Eppley pyrheliometer which has broader (0.2-3.0μ) and flatter response characteristics (MacDonald, 1951). This procedure, under static atmospheric conditions, enables one to get accurate measurements of the total incoming solar energy from the Sol-a-meter. It is clear, however, that this calibration will change as the intervening air mass changes since the Sol-a-meter does not respond to the longer wavelengths of solar radiation (1-3μ) where, for

TABLE 1.5.2. INTEGRATED DIRECTIONAL REFLECTANCE AND RELATIVE ANISOTROPY OBSERVED BY THE NIMBUS F-3 RADIOMETER OVER DIFFERENT SURFACES WITH VARYING SOLAR ZENITH ANGLE.

(1)	(2)	(3)	(4)	(5)	(6)	(7)	(8)	(9)	(10)
FLIGHT NO.	SURFACE	SOLAR ZENITH ANGLE (°)	INCOMING ENERGY (S') (LY/MIN)	$(r_D)_N$	$(r_D)_N/(\bar{r})_o$	$(r_D)_B$	$(r_D)_B/(\bar{r})_o$	$\frac{S}{S'}(r_D)_B$	$(r_D)_N-(r_D)_B$
1	STRATUS	58-68	0.65	0.54	1.45	0.44	1.54	0.61	0.10
2	STRATUS	16-17	1.71	0.45	0.95	0.34	0.96	0.38	0.11
3	STRATUS	45-54	1.08	0.56	1.22	0.44	1.24	0.53	0.12
4	STRATUS	17-18	1.70	0.45	1.05	0.36	1.04	0.43	0.09
5	STRATUS	57-58	0.80	0.87	1.21	0.64	1.26	0.86	0.23
6	STRATUS	63-66	0.56 Thin Ci	0.78	1.32	0.57	1.36	0.88	0.21
7	STRATUS	76-79	-------	0.77	1.74	0.60	1.73	----	0.17
8	STRATUS	66-70	0.50	0.87	1.27	0.61	1.36	0.91	0.26
9	SNOW	82-86	-------	0.73	1.20	0.49	1.19	----	0.24
10	SNOW	63-65	0.64	0.90	1.06	0.58	1.10	0.81	0.32
11	SNOW	66-70	0.50	0.88	1.10	0.55	1.16	0.82	0.33
12	WHITE SAND	20-22	-------	0.65	0.96	0.46	0.96	----	0.19
13	WHITE SAND	76-82	-------	0.73	1.13	0.55	1.13	----	0.18
14	WHITE SAND	57-61	0.80	0.69	1.07	0.53	1.08	0.69	0.16
15	WHITE SAND	47-49	1.04	0.70	1.05	0.54	1.05	0.71	0.16
16	WHITE SAND	57-61	0.62 Thin Ci	0.60	1.07	0.41	1.08	0.71	0.19
17	DESERT LAKE BED	58-59	0.72	0.28	1.13	0.23	1.14	0.33	0.05
18	DESERT LAKE BED	70-73	0.35	0.24	1.23	0.19	1.18	0.34	0.05
19	GRASSLAND	59-63	-------	0.19	1.29	0.19	1.30	----	0.00
20	GRASSLAND	57-59	-------	0.21	1.31	0.19	1.28	----	0.02
21	GRASSLAND	55-57	-------	0.18	1.26	0.19	1.18	----	-0.01
22	GRASSLAND	66-69	0.57	0.23	1.27	0.24	1.30	0.32	-0.01
23	GRASSLAND	59-62	0.72	0.22	1.22	0.22	1.18	0.30	-0.00
24	GRASSLAND	78-82	-------	0.13	2.18	0.16	1.80	----	-0.03
25	VEGETATION -SWAMP	56-61	0.74	0.07	1.68	0.11	1.37	0.16	-0.04
26	VEGETATION -SWAMP	70-73	0.40	0.08	2.45	0.11	1.61	0.18	-0.03

instance, absorption by water vapor takes place. At increasing altitudes above the surface, this effect would result in the instrument giving a reading which is below the true value since the water vapor content tends to decrease rapidly with height. In general, therefore, the corrected broad bandpass reading in Column 9 will be higher than the true values since they were all taken from 120-1200 meters above the reflecting surface. The corrected integrated directional broad bandpass results, however, are much more comparable to true albedoes than the uncorrected readings in that the above effect can produce an error of only a few percent.

Upon examination of the results given in Column 9, it can be ascertained that, although none of the results appear to be outside the range of possibility (List, 1963, pp. 442-443), they do appear to be always on the high side of the expected values. In particular, the results over stratus clouds in flight 5 and 6 and the results near Logan, Utah, are subject to conjecture.

For the flights near Logan, Utah, another factor causing high readings of integrated directional reflectance exists. In this area the reflecting surfaces in the Cache Valley were surrounded by high, snow-covered mountains. It is reasonable to expect that an appreciable portion of the solar radiation reflected from these mountains would strike the stratus and snow surfaces (which were well below the tops of the mountains) in the valley and again be

reflected. This occurrence would result in a higher albedo detected by the aircraft since its flight altitude was near the top of the mountains. This reasoning would indicate that the true reflectance value for the snow near Laramie, Wyoming, was higher than that near Logan, Utah. This conclusion is in agreement with the fact that the snow near Logan, Utah, had been on the ground longer than that at Laramie and would have a lower albedo (List, 1963, pp. 442-443).

The data in Column 9 does indicate that the integrated directional reflectance over stratus clouds increases with increasing solar zenith angle. This conclusion is supported by results given in Feigel'son (1966, p. 103). It is further observed in this column that the underlying surface has an influence on the magnitude of the reflected radiation from stratus clouds. This can be most easily seen when comparing the results for stratus clouds over water with the result given for stratus clouds over snow near Logan, Utah.

The thickness of a cloud also influences the magnitude of the reflectances observed. This may be seen in the flights near San Francisco on 11 June and 17 July 1965. For the flights near San Francisco and Bakersfield, California, the reflectance may be seen to increase markedly as the thickness of the clouds increases (Column 14). The data further suggests that the change in reflectance with increasing cloud thickness is less rapid as the clouds

become thicker. These conclusions and the data in Column 9 agree rather well with those published by Neiburger (1949).

Columns 6 and 8 of Table 1.5.2 present the varying magnitudes of the relative anisotropy parameter. As might be expected from the results reviewed in Figs. 1.5.1-8, the magnitude of this term increases as the solar zenith angle increases. This observation is particularly evident in the case of stratus clouds. The absolute magnitude of this term further shows that the anisotropy in reflected radiation from white gypsum sand is the least of all surfaces. In the case of soils and vegetation covered surfaces, the low magnitude of the reflectances causes a large variation in the relative anisotropy term for a relatively small variation in the magnitude of the reflectances. Still the term serves to illustrate the percentage error that could be made in inferring the albedo of a surface with a limited view radiometer.

It should be pointed out that on an empirical basis, a radiometer zenith angle could be selected in the principal plane which would give a measurement close to the albedo of the surface being examined. As an example, in Fig. 1.5.2 a reading at $\psi=0^{o}$ and $\theta=30^{o}$ would correspond closely to the broad bandpass integrated directional reflectance of 0.64.

In Figs. 1.5.1-8, part (c), and in Column 10 of Table 1.5.2, the difference in reflectance between the narrow and broad bandpasses can be seen to vary for each type of surface. The variation in the difference is primarily the effect of the spectral reflectivity characteristics of the surface. However, it is also an indication of the effect of the spectral characteristics of the incoming energy and the bandpass filter characteristics. The influence of the underlying surface is evident again in Column 10 in the data for stratus clouds. The difference in the bandpass reflectances for stratus clouds over water is clearly less than that determined for other cases, particularly where stratus clouds were underlain by snow. In general, the data in Column 10 is supported by measurements of spectral reflectivity reported by Hovis (1966), Bartman (1967), and Dirmhirn (1967). The apparently anomalous result in this column for flight 9 is attributed either to the appearance of shadows or possibly to insufficient accuracy in the determination of the solar zenith angle.

In the previous section it was noted that an attempt was made to see if a variation in the reflectance over the grassland-sod surface could be detected that was attributable to a change in the flight altitude at which the measurements were made. For the purposes of this comparison it is best to examine the results of flights 22 and 23 in Table 1.5.2 and Figs. 1.6.1-2. The atmospheric and flight conditions on these two flights were optimum

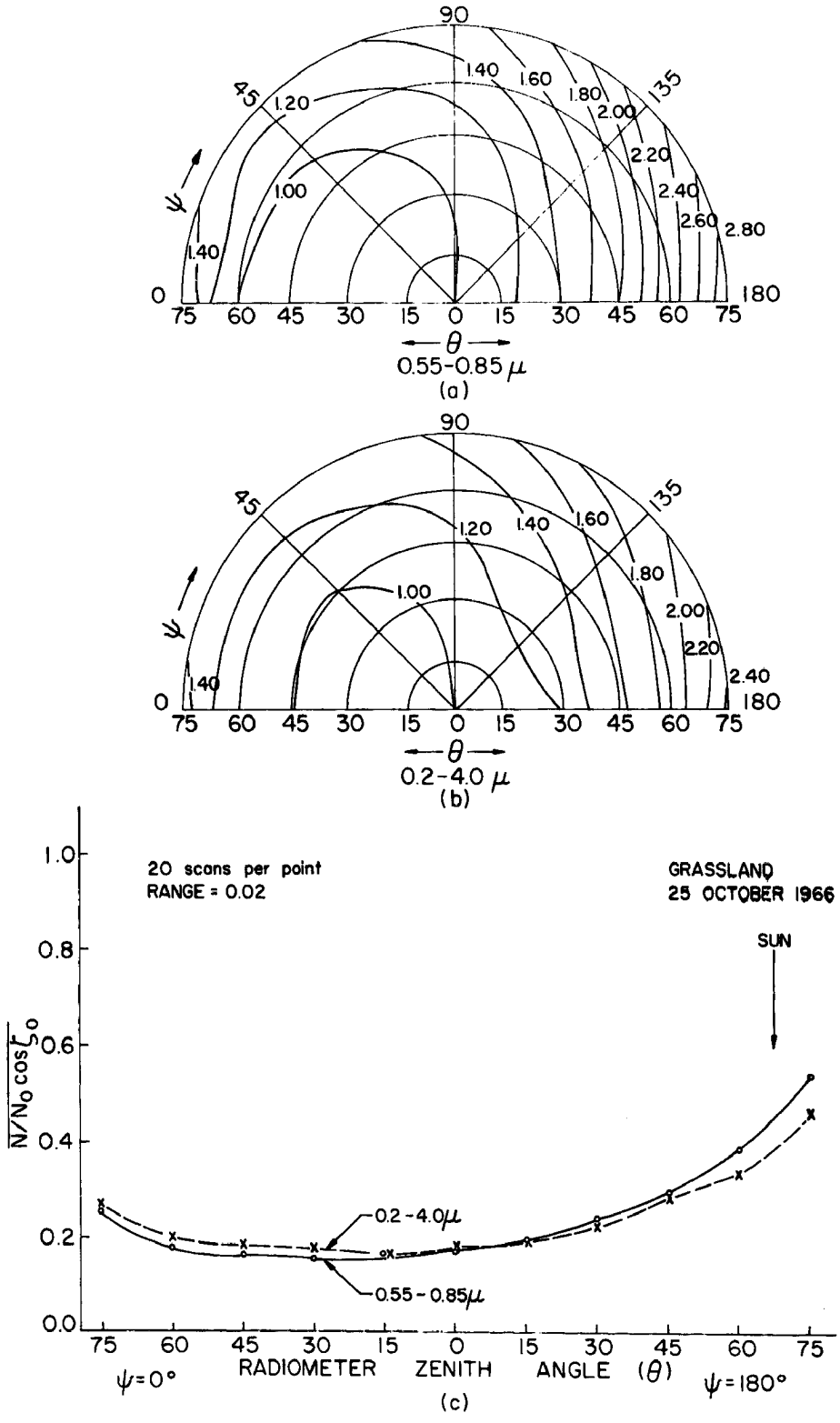

Fig. 1.6.1. Same as Fig. 1.5.1 except that the reflectances are over a grassland-sod surface near Briggsdale, Colorado, on 25 October 1966 (ζ_o=66-69°). The height above the surface was 1370 m.

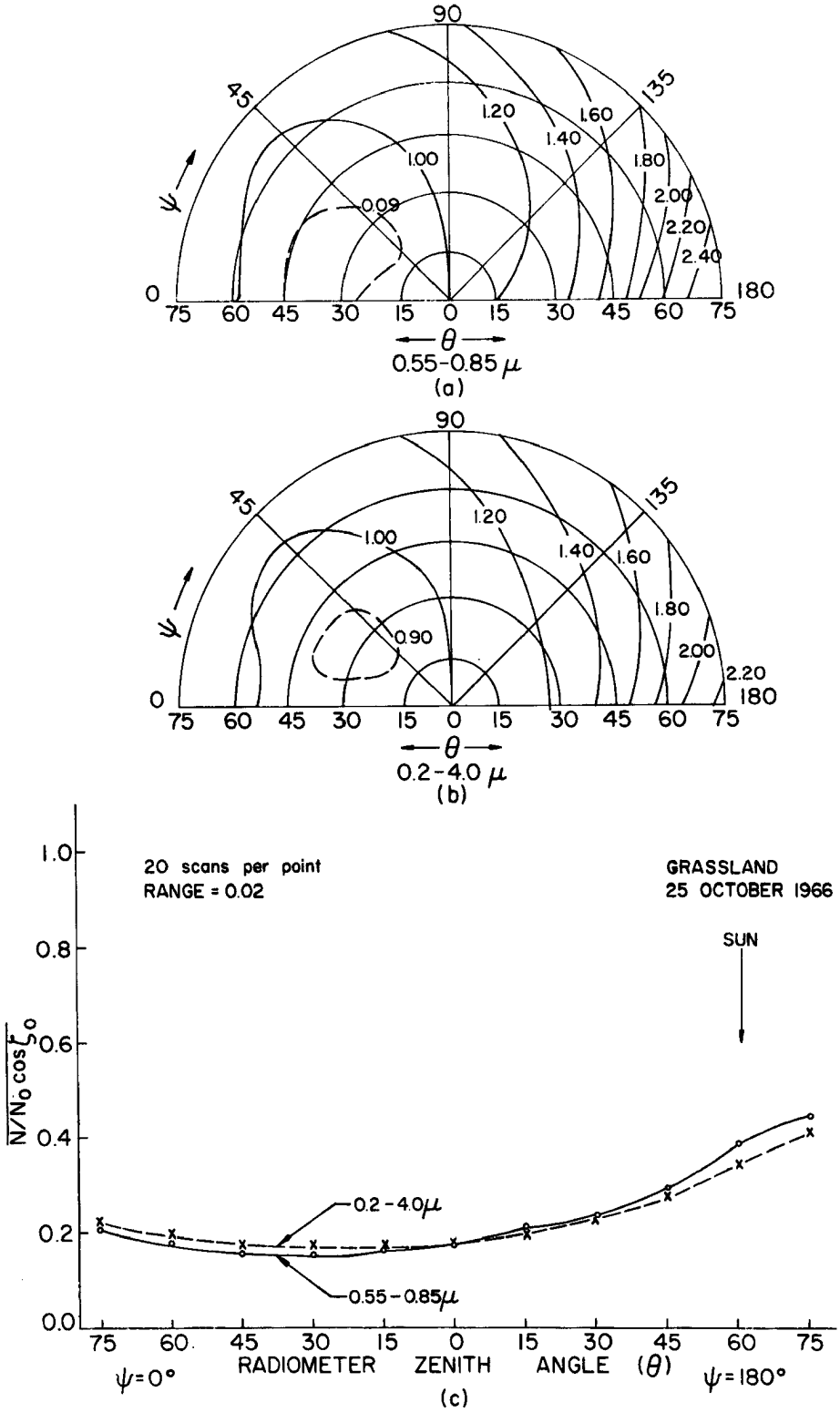

Fig. 1.6.2. Same as Fig. 1.5.1 except that the reflectances are over a grassland-sod surface near Briggsdale, Colorado, on 25 October 1966, 0934-0957 MST (ζ_o=59-62°). The height above the surface was 610 m.

and so an accurate comparison is possible. Upon examination of the figures it can be seen that an increased limb brightening effect is evident in Fig. 1.6.1 versus 1.6.2. This result occurs because of the increased altitude and the accompanying increase in the intervening air mass between the airplane and the reflecting surface. The altitude influence also appears in Column 9 of Table 1.5.2 where an increased r_D is also noted at the higher altitude due, at least in part, to the increased reflectance from the intervening air mass. It must be realized that in all of these measurements the intervening air mass is a part of the observed results although the low flight altitudes in most of the flights made the effect a small one. The influence of the intervening air mass on the observations is naturally larger the nearer an observation is to the horizon.

There were four flights made over a relatively calm ocean surface near Oceanside and Los Angeles, California. The objective of these flights was to compare the aircraft measurements with theoretical calculations of specular reflection from a still water surface. Unfortunately, the specular component of the reflected solar radiation was so large that it exceeded the limits of the calibration curves so far that only qualitative observations could be made. Fig. 1.6.3 shows the approximate distribution of the reflectance r' for the broad bandpass in the principal plane under the illumination conditions indicated. As

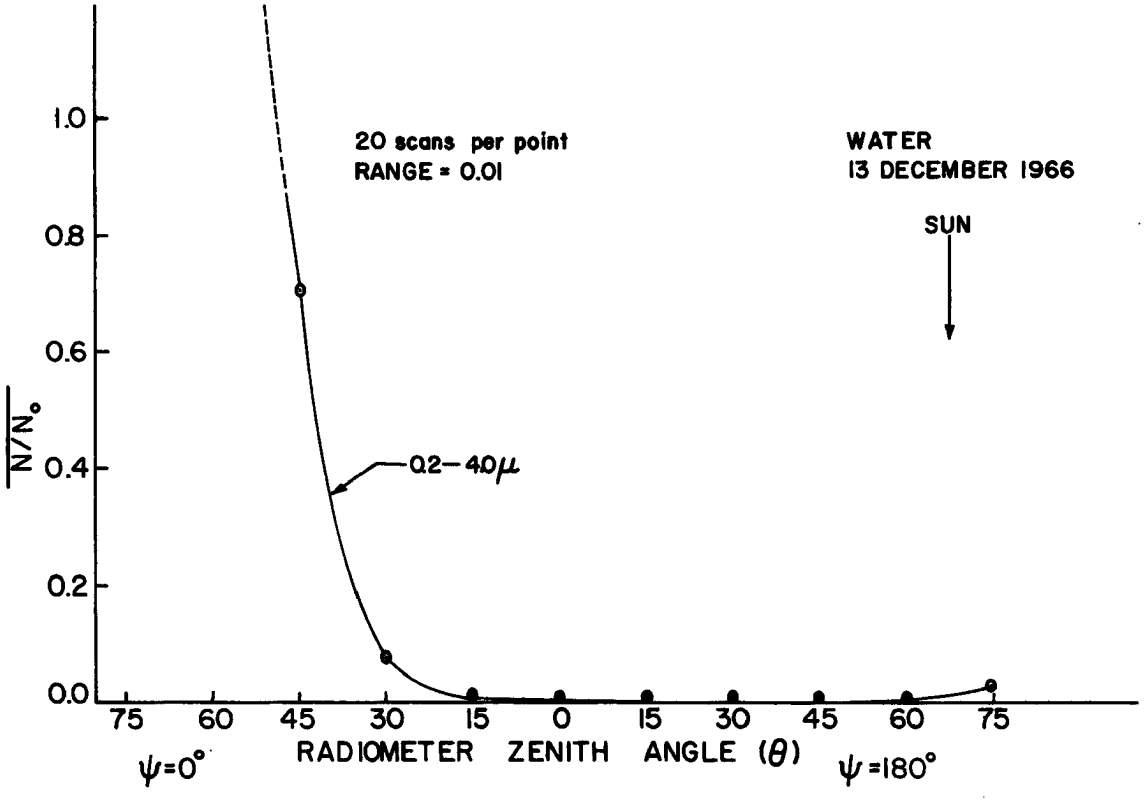

Fig. 1.6.3. The observed distribution of reflectance (r') in the principal plane over a water surface near Oceanside, California, on 13 December 1966, 0952-1020 PST (ζ_o=63-66°).

can be seen, the specular component is very large and the remainder of the reflectances are very small except near the horizon on the antisolar side where some increased reflectance was observed.

1.7. Conclusions

The results presented in this chapter show that the reflectance from surfaces representative of a majority of terrestrial surfaces is sufficiently anisotropic as to dictate that this factor be considered in attempts to ascertain the planetary albedo from satellite radiometers with a limited field of view. As an example of the importance of considering this factor and the contributions that it made in global energy balance calculations, one is referred to a study by Raschke and Pasternak (1967). In that study some of the results coming from this chapter and other sources were used to calculate a global energy balance using data from the NIMBUS II satellite and a radiometer very nearly identical to the one used in this research. The planetary albedo achieved in that study was near 30 percent. This was a definite improvement over the results achieved by Bandeen et. al. (1965).

It was also quite evident from the observations that it is very important in determining the planetary albedo from a satellite to use only the data from a bandpass admitting nearly all wavelengths in the solar spectrum such as, for example, the broad bandpass of the MRIR.

The results here show that the use of narrower bandpasses will result in values of reflectance which are dependent upon the spectral reflectivity of the surface, the spectral distribution of the incoming energy, and the spectral response characteristics of the instrument. To extrapolate such values accurately so as to determine the total solar energy reflected from a surface would require detailed knowledge of these factors and would be difficult to do for global radiation studies such as those referred to above.

The observations reviewed in this chapter were taken under completely natural conditions insofar as the illumination and character of each surface were concerned. As a result, these data are a valuable source of comparison for numerical studies attempting to simulate the transfer and distribution of solar energy at various levels in the atmosphere. It would be very interesting to determine quantitatively exactly how much of a role the scattering and absorption of the intervening air mass had on the observations. These observations suggested that scattering from the atmosphere was a significant component of the reflectances observed near the horizon. To know the role of different haze concentrations on reflectance measurements would be particularly interesting.

In as much as anisotropy was observed over the majority of surfaces considered here, it would be well to examine how this anisotropy was produced. It is important to know, for

instance, what effect the size and configuration of the elements comprising each surface have in relation to the wavelength of the incident solar energy on the resulting anisotropy. An analysis of the importance of such factors in the observed scattering from stratus clouds is given in Chapters II and III.

Chapter II

A THEORETICAL FRAMEWORK FOR ANALYZING SCATTERING FOR STRATUS CLOUDS

2.1. Introduction

In Chapter I varying degrees of anisotropy in the reflection of solar radiation from various surfaces were described. The question arises as to how this anisotropy occurs and how it may be described mathematically. In the case of reflection from sand, snow, desert soil, grassland, and vegetation, a mathematical description of the reflection properties of the surface is very difficult. The difficulty arises because of the non-uniformity and irregularity of the surfaces and the elements comprising each surface. Because of the size of these elements with respect to the wavelength of the incident light, it is clear that a geometrical-optics approach which considers the inclination of the various surfaces to the incident beam is a logical starting point. This was done by Middleton and Mungall (1952) who derived an approximate theory describing the quasi-specular reflection from snow surfaces. Beckmann and Spizzichino (1963) discuss many other important aspects of scattering from rough surfaces.

The surface which does readily lend itself to investigation of its scattering properties is the stratus cloud. The stratus cloud resembles, more closely than any other cloud form, the plane-parallel atmosphere commonly assumed

in atmospheric radiative transfer theory. Furthermore, it is composed of particles which can, for all practical purposes, be considered spherical. Thus, the interaction of electromagnetic energy with the spheres can be accurately described by what is commonly known as the Mie theory. The elements of the radiative transfer theory and scattering in polydispersed particulate volumes as they resemble a cloudy atmosphere is described in the following pages.

2.2. The Equation of Radiative Transfer

The most general mathematical description of the interaction of radiant energy with an atmospheric volume is contained within the radiative transfer theory as described by Chandrasekhar (1960), Sobolev (1963), Ambartsumyan (1958), and Busbridge (1960). It is now necessary to describe the components of the equation of radiative transfer as it applies to a scattering atmosphere.

One of the basic parameters used is the specific intensity I_ν where ν refers to the frequency of the energy being considered. I_ν is related to the spectral radiant energy E_ν by the expression

$$I_\nu = \frac{d^4E_\nu}{\cos\theta d\nu dA d\Omega dt} \qquad 2.2(1)$$

where θ is the zenith angle of the outgoing radiation (measured with respect to the outward normal to the area

element dA), $d\Omega$ is the solid angle element and dt is a unit of time. In the expression above dA, $d\Omega$, $d\nu$, and dt may approach zero in any manner.

Another fundamental quantity is the "net flux" (Chandrasekhar, 1960). This may be defined as the rate of flow of radiant energy across a unit area per unit frequency interval, and can be expressed as

$$F_\nu = \int_\Omega I_\nu \cos\theta \, d\Omega. \qquad 2.2(2)$$

For a scattering atmosphere one can define a mass-scattering coefficient κ_ν. By using this coefficient it is possible to describe the amount of energy depleted from an incident pencil of radiation passing through a cylindrical disk of thickness ds and cross section dA perpendicular to the pencil of radiation. The density of the scattering material is ρ_o. The depletion of the incident pencil of radiation of some intensity I_ν after having passed through the cylindrical element is now expressed as

$$dI_1 d\nu dA d\Omega dt = -(\kappa_\nu \rho_o ds)\ (I_\nu d\nu dA d\Omega dt). \qquad 2.2(3)$$

For a cloudy atmosphere it will be appropriate to define a volume scattering coefficient $\beta_\nu = \kappa_\nu \rho_o$. As a result

Eq. 2.2(3) appears as

$$dI_1 d\nu dA d\Omega dt = -(\beta_\nu ds)\ (I_\nu d\nu dA d\Omega dt). \qquad 2.2(4)$$

The fraction of the depleted energy scattered through an angle Θ into a solid angle $d\Omega'$ can be written as follows:

$$(\beta_\nu ds)\ (I_\nu d\nu dA d\Omega dt)\ p(\Theta). \qquad 2.2(5)$$

The phase function $p(\Theta)$ designates the distribution of the scattered energy. A comparison of 2.2(5) with 2.2(4) specifies the following normalization for the phase function:

$$\int_{\Omega'} p(\Theta)\ \frac{d\Omega'}{4\pi} = 1\ . \qquad 2.2(6)$$

The phase function can be obtained through the application of scattering theory that will be described in the next section.

One must recognize in a scattering atmosphere that energy scattered outside a volume element may proceed into the volume, be scattered again, and emerge in the direction of the incident beam. When this contribution is expressed mathematically, it is called the "source function" and can be written,

$$J_\nu = \int_{\Omega'} p(\Theta)\ I_\nu'\ \frac{d\Omega'}{4\pi} \qquad 2.2(7)$$

If the losses dI_1 and the gain J_ν are totaled, the equation of radiative transfer for the conservative case is

$$-\frac{dI_\nu}{\beta_\nu ds} = I_\nu - J_\nu. \qquad 2.2(8)$$

For radiative transfer problems it is common to apply the equation of radiative transfer to a plane-parallel atmosphere where linear distances are measured normal to the plane of stratification in the direction z (see Fig. 1.3.1). It is further common to express the equation of radiative transfer in terms of the normal optical depth τ which is related to volume scattering coefficient and length ds as follows:

$$\tau = \int_z^\infty \beta_\nu dz \qquad 2.2(9)$$

where $dz=-\cos\theta ds$. Subsequently, Eq. 2.2(8) assumes its standard form for a plane parallel atmosphere,

$$\eta \frac{dI}{d\tau} = I - J \qquad 2.2(10)$$

where n is used to designate $\cos\theta$. $A + n$ designates radiation propagated upward and a $- n$ designates radiation propagated downward. The substript ν has been dropped for convenience and monochromacity will be assumed unless otherwise noted.

Eq. 2.2(10) pertains to the total intensity derived from energy considerations and does not take into account the polarization properties of the radiation. This same equation can be extended to a matrix form that completely describes the incident and scattered light (Sekera, 1957). The intensity is replaced by a column matrix composed of the Stokes vectors, I_{ℓ}, I_{r}, U, and V. The subscripts ℓ and r designate the intensity components parallel and perpendicular to the meridional plane passing through the local vertical and the direction of propagation of the intensity vector. U and V are intensities related respectively to the plane of polarization and the ellipticity of the polarization.

When the idea in the preceding paragraph is implemented and the source function is split into a parallel beam component and a diffuse component, the equation of transfer for a scattering atmosphere may be expressed as follows:

$$\eta \frac{d\mathbb{I}(\tau;\eta,\phi)}{d\tau} = \mathbb{I}(\tau;\eta,\phi)$$

$$- \frac{1}{4\pi} \int_{-1}^{+1} \int_{0}^{2\pi} \mathbb{P}(\eta,\phi;\eta',\phi') \cdot \mathbb{I}(\tau;\mu',\phi') d\eta' d\phi'$$

$$- \frac{1}{4\pi} \mathbb{P}(\eta,\phi;\cos\zeta_o,\phi_o) \cdot \mathbf{F} \cdot \exp(-\tau/\cos\zeta_o).$$

2.2(11)

The elements of the phase matrix $\mathbb{P}$ can be obtained from scattering theory. In the first step of this process the elements of the phase matrix apply to the components of the incident and scattered waves perpendicular and parallel to the scattering plane which goes through the direction of propagation of both the incident and scattered beams. For a medium comprised of spherical scatterers it can be shown (Van de Hulst, 1957, chapter 5) that the elements of this first matrix are

$$\mathbb{P}' = \begin{vmatrix} P_{11} & 0 & 0 & 0 \\ 0 & P_{22} & 0 & 0 \\ 0 & 0 & P_{33} & P_{34} \\ 0 & 0 & P_{43} & P_{44} \end{vmatrix} \qquad 2.2(12)$$

where

$$P_{11}=P_1,\ P_{22}=P_2,\ P_{33}=P_{44}=P_3,\ \text{and}\ P_{34}=-P_{43}=P_4. \qquad 2.2(13)$$

The way in which these components may be computed from Mie theory will be described in later pages.

Once $\mathbb{P}'$ has been obtained it is necessary to transform the elements of the matrix so that it can be used in Eq. 2.2(11). This is a rather lengthy geometry problem that has been described in Chandrasekhar (1960), Zekera (1955), and Herman (1964). For the application to be described in Chapter IV only the basic matrix elements in $\mathbb{P}'$ need to be referred to here.

2.3. The Mie Theory

There are several good references which describe the diffraction of a plane electromagnetic wave by a homogeneous sphere or, as it has come to be commonly known, the Mie theory (Mie, 1908; Debye, 1909; Van de Hulst, 1957; Born and Wolf, 1959; Van Bladel, 1964; Herman, 1964; and Shifrin, 1968). The development which follows is very close to that of Born and Wolf. For a homogeneous, isotropic medium having a dielectric constant ε, magnetic permeability ξ, and electroconductivity σ, Maxwell's equations have the following form when using Gaussian units:

$$\nabla \times \underset{\sim}{H} - \frac{1}{c}\frac{\partial \underset{\sim}{D}}{t} = \frac{4\pi}{c}\underset{\sim}{j} \qquad 2.3(1)$$

$$\nabla \times \underset{\sim}{E} + \frac{1}{c}\frac{\partial \underset{\sim}{B}}{\partial t} = 0 \qquad 2.3(2)$$

$$\nabla \cdot \underset{\sim}{D} = 4\pi\rho' \qquad 2.3(3)$$

$$\nabla \cdot \underset{\sim}{B} = 0 \; . \qquad 2.3(4)$$

$\underset{\sim}{D}$ and $\underset{\sim}{B}$ are the electric displacement and magnetic induction vectors respectively, $\underset{\sim}{E}$ and $\underset{\sim}{H}$ are the electric and magnetic field vectors, $\underset{\sim}{j}$ is the current density, ρ' is the charge density, and c is the speed of light in a vacuum. For linear[2] matter there are constitutive relationships between the induction and field vectors that are often called the "material equations" because they describe the macroscopic properties which control the interaction of the matter with electromagnetic energy. For simple matter these relationships can be expressed as follows:

$$\underset{\sim}{D} = \varepsilon \underset{\sim}{E} \qquad 2.3(5)$$

---

[2]Linear matter is matter in which the relationships can be described by a linear differential equation with time. In simple linear matter only the first term, independent of time, is used as in Eqs. 2.3(5)-2.3(7).

$$\underset{\sim}{B} = \xi \underset{\sim}{H} \qquad 2.3(6)$$

$$\underset{\sim}{j} = \sigma \underset{\sim}{E} \; . \qquad 2.3(7)$$

From this point, the following assumptions, true of all isotropic, homogeneous dielectric materials, will be made for mathematical and simplicity:

a) ε, ξ, and σ are independent of time

b) The magnetic permeabilities are all 1.

c) No free charges exist in any of the particles or bodies examined.[3]

d) The electric and magnetic fields are harmonic functions of time (proportional to $e^{-i\omega t}$ where ω is the field frequency).

With these assumptions, Eqs. 2.3(1-4) can be written:

$$\nabla \times \underset{\sim}{H} = \left(\frac{4\pi\sigma}{c} - \frac{i\varepsilon\omega}{c}\right) \underset{\sim}{E} = -k_1 \underset{\sim}{E} \qquad 2.3(8)$$

$$\nabla \times \underset{\sim}{E} = \frac{i\omega}{c} \underset{\sim}{H} = k_2 \underset{\sim}{H} \qquad 2.3(9)$$

$$\nabla \cdot \underset{\sim}{E} = 0 \qquad 2.3(10)$$

---

[3] It can be shown (Stratton, 1941; Born and Wolf, 1959) that for any region with non-vanishing conductivity, the free charge decays exponentially with time and can be set to zero.

$$\nabla \cdot \underset{\sim}{H} = 0. \qquad 2.3(11)$$

By substituting the first two equations into each other, and using the vector identity $\nabla X \nabla X \underset{\sim}{A} = \nabla(\nabla \cdot \underset{\sim}{A}) - \nabla^2 \underset{\sim}{A}$ and the last two relations, the following equations are obtained:

$$\nabla^2 \underset{\sim}{E} = k^2 \underset{\sim}{E} = 0 \qquad 2.3(12)$$

$$\nabla^2 \underset{\sim}{H} + k^2 \underset{\sim}{H} = 0 \qquad 2.4(13)$$

where $k^2 = -k_1 k_2$.

If $\underset{\sim}{E}$ or $\underset{\sim}{H}$ is replaced by the scalar Y in 2.3(2), then one has the scalar wave equation,

$$\nabla^2 Y + k^2 Y = 0. \qquad 2.3(14)$$

This equation expressed in spherical coordinates will be referred to later on.

Eqs. 2.3(8) and 2.3(9) can also be written as

$$\nabla \times \underset{\sim}{H} = -ik_o m_o^2 \underset{\sim}{E} \qquad 2.3(15)$$

$$\nabla \times \underset{\sim}{E} = ik_o \underset{\sim}{H} \qquad 2.3(16)$$

where $k_o = \frac{\omega}{c}$ and

$$m_o^2 = \varepsilon + i\frac{4\pi\sigma}{\omega} = (n-in')^2 \qquad 2.3(17)$$

m_o is the complex index of refraction having a real part called the real index of refraction and an imaginary part often referred to as the absorption term.

As with any physical problem the fields, $\underset{\sim}{E}$ and $\underset{\sim}{H}$, must satisfy not only Maxwell's equations but also certain boundary conditions. In particular, Maxwell equations must be satisfied within regions that are sections of a discontinuity such as the boundary between a particle or droplet and its surrounding medium. Furthermore, the behavior of the diffracted field must behave regularly at infinity and at the origin. These requirements will be dealt with more explicitly later.

For the diffraction of a plane wave by a sphere, a spherical coordinate system is appropriate. For ease of referral a more simple and appropriate diagram than Fig. 1.3.1 is presented below.

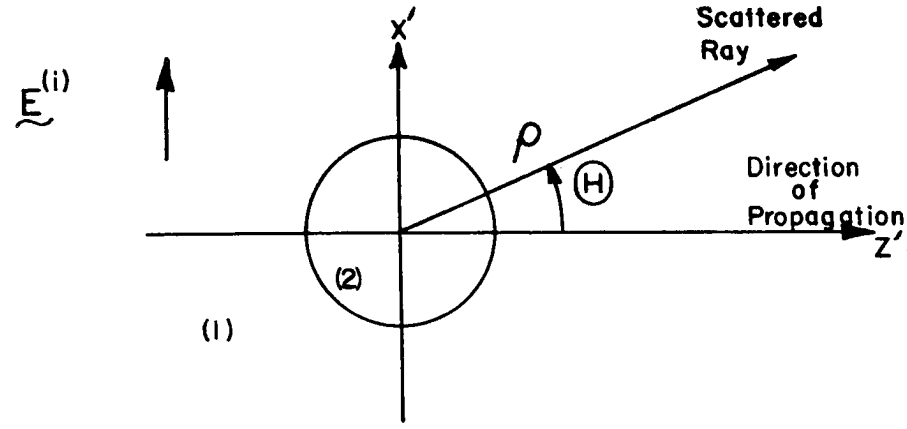

Fig. 2.3.1. A simplified spherical coordinate system.

The quantities that refer to the medium outside the sphere will be designated by the superscripted arabic numeral 1 in parentheses and those quantities associated with conditions inside the sphere will be designated in a similar manner by the arabic numeral 2.

From the geometry in Fig. 2.3.1 and the general boundary condition requirements, it is evident that the tangential components of $\underset{\sim}{E}$ and $\underset{\sim}{H}$ must be continuous across the surface of the sphere. It is further evident that the total field outside the sphere is made up of the incident and scattered fields while the total field within the sphere consists only of the transmitted component. All six components of the fields, $\underset{\sim}{E}$ and $\underset{\sim}{H}$, have the same time dependence, $e^{-i\omega t}$. This insures that the scattering occurs without a change in frequency. For convenience it will be assumed from this point on that $|E^{(i)}| = |e^{-i\omega t}| = 1$.

In essence, the solution of the scattering of a linearly polarized electromagnetic wave by a spherical particle consists of the following. The six unknown components will be expressed in terms of two functions described as electric and magnetic potentials. These potentials will be shown to be solutions of the wave equation and will be expressed in terms of the spherical coordinates by using a Fourier analysis consisting of infinite sums of special solutions with unknown coefficients. The unknown coefficients will be determined by applying the boundary conditions to the fields inside and outside the sphere.

With the above synthesis in mind, Maxwell's equations for $\underset{\sim}{E}$ and $\underset{\sim}{H}$ may be expressed in component forms appropriate for a spherical coordinate system. The proper form for the vector curl operation can be found in Godske et. al., (1957). Eqs. 2.3(8) and 2.3(9) in component form appear as follows:

$$-k_1 E_\rho = \frac{1}{\rho \sin\theta} \frac{\partial}{\partial\theta}(\sin\theta H_\Phi) - \frac{\partial H_\theta}{\partial \Phi} \qquad 2.3(18)$$

$$-k_1 E_\theta = \frac{1}{\rho \sin\theta} \frac{\partial H_\rho}{\partial \Phi} - \frac{\partial(\rho H_\phi \sin\theta)}{\partial \rho} \qquad 2.3(19)$$

$$-k_1 E_\Phi = \frac{1}{\rho} \frac{\partial}{\partial \rho}(\rho H_\theta) - \frac{\partial}{\partial \theta}(H_\rho) \qquad 2.3(20)$$

$$k_2 H_\rho = \frac{1}{\rho^2 \sin\theta} \frac{\partial(\rho E_\Phi \sin\theta)}{\partial\theta} - \frac{\partial(\rho E_\theta)}{\partial\phi} \qquad 2.3(21)$$

$$k_2 H_\theta = \frac{1}{\rho \sin\theta} \frac{\partial E_\rho}{\partial \Phi} - \frac{\partial(\rho E_\Phi \sin\theta)}{\partial \rho} \qquad 2.3(22)$$

$$k_2 H_\Phi = \frac{1}{\rho} \frac{\partial(\rho E_\theta)}{\partial \rho} - \frac{\partial E_\rho}{\partial \theta} \; . \qquad 2.3(23)$$

At $\rho=a$, the radius of the sphere, the boundary conditions require that

$$E_{\Theta}^{(1)} = E_{\Theta}^{(2)} \qquad 2.3(24)$$

$$H_{\Theta}^{(1)} = H_{\Theta}^{(2)} \qquad 2.3(25)$$

$$E_{\Phi}^{(1)} = E_{\Phi}^{(2)} \qquad 2.3(26)$$

$$H_{\Phi}^{(1)} = H_{\Phi}^{(2)}. \qquad 2.3(27)$$

The electromagnetic field may be represented as a superposition of two types of oscillations. One oscillation will have a vanishing magnetic field in the ρ direction and will be termed the electric wave. The oscillation with a vanishing electric field in the ρ direction will be called the magnetic wave. These conditions are expressed as

$$^{e}E_{\rho} = E_{\rho} \quad , \quad ^{e}H_{\rho} = 0 \quad , \qquad 2.3(28)$$

and

$$^{m}E_{\rho} = 0 \quad , \quad ^{m}H_{\rho} = H_{\rho} \quad . \qquad 2.3(29)$$

For the case of the electric wave it can be seen that in Eq. 2.3(21),

$$\frac{\partial}{\partial\Theta}\left({}^{e}E_{\Phi}\sin\Theta\right) = \frac{\partial}{\partial\Phi}\left({}^{e}E_{\Theta}\right) . \qquad 2.3(30)$$

This relationship will be satisfied if one assumes that $E_{\Phi}\sin\Theta$ and E_{Θ} are derivatives of some function Φ_{o}. This means that

$${}^{e}E_{\Phi}\sin\Theta = \frac{\partial\Phi_{o}}{\partial\Phi} \qquad 2.3(31)$$

and

$${}^{e}E_{\Theta} = \frac{\partial\Phi_{o}}{\partial\Theta} . \qquad 2.3(32)$$

When this assumption is substituted into 2.3(19-20), one obtains

$$k_{1}\frac{\partial\Phi_{o}}{\partial\Theta} = \frac{1}{\rho}\frac{\partial\left(\rho\,{}^{e}H_{\Phi}\right)}{\partial\rho} \qquad 2.3(33)$$

and

$$-k_{1}\frac{\partial\Phi_{o}}{\partial\Phi} = \frac{\sin\Theta}{\rho}\frac{\partial}{\partial\rho}\left(\rho\,{}^{e}H_{\Theta}\right). \qquad 2.3(34)$$

These last two results will be satisfied if we assume $\Phi_o = \rho^{-1}\,(\partial Y/\partial\rho)$ so that

$$e_{H_\Phi} = \frac{k_1}{\rho}\frac{\partial Y}{\partial\Theta} \qquad 2.3(35)$$

and

$$e_{H_\Theta} = \frac{-k_1}{\rho\sin\Theta}\frac{\partial Y}{\partial\Phi}\,. \qquad 2.3(36)$$

Furthermore, Eqs. 2.3(31) and 2.3(32) now have the form

$$e_{E_\Phi} = \frac{1}{\rho\sin\Theta}\frac{\partial^2 Y}{\partial\Phi\partial\rho} \qquad 2.3(37)$$

and

$$e_{E_\Theta} = \frac{1}{\rho}\frac{\partial^2 Y}{\partial\Theta\partial\rho}\,. \qquad 2.3(38)$$

Finally if one substitutes 2.3(35-38) into 2.3(18), an expression for the final component e_{E_ρ} is obtained:

$$e_{E_\rho} = \frac{1}{\rho^2\sin\Theta}\left\{\frac{\partial}{\partial\Theta}\left(-\sin\Theta\frac{\partial Y}{\partial\Theta}\right) - \frac{\partial}{\partial\Phi}\left(\frac{1}{\sin\Theta}\frac{\partial Y}{\partial\Theta}\right)\right\}\,. \qquad 2.3(39)$$

When the components (2.3.35-39) are substituted into 2.3(22-23), one gets the same result:

$$\frac{1}{\rho^2 \sin\theta}\left[\frac{\partial}{\partial\theta}\left(-\sin\theta\frac{\partial Y}{\partial\theta}\right)-\frac{1}{\sin\theta}\frac{\partial^2 Y}{\partial\Phi^2}\right]-\frac{\partial^2 Y}{\partial\rho^2}-k^2 Y=0$$

2.3(40)

By examining this last equation and having a prior knowledge of the Laplacian operator in spherical coordinates, one can see that it is advantageous to let $Y=\rho U_1$. This allows 2.3(40) to be expressed as

$$\frac{1}{\rho}\frac{\partial^2(\rho U_1)}{\partial\rho^2}+\frac{1}{\rho^2\sin\theta}\frac{\partial}{\partial\theta}\left(\sin\theta\frac{\partial U_1}{\partial\theta}\right)+\frac{1}{\rho^2\sin^2\theta}\frac{\partial^2 U_1}{\partial\Phi^2}+k^2 U_1=0\,.$$

2.3(41)

which one can recognize as 2.3(14) in spherical coordinates. This change of variable finally dictates that 2.3(35-39) have the following forms:

$$e_{E_\Phi}=\frac{1}{\rho\sin\theta}\frac{\partial^2(\rho U_1)}{\partial\rho\partial\Phi} \qquad 2.3(42)$$

$$e_{E_\theta}=\frac{1}{\rho}\frac{\partial^2(\rho U_1)}{\partial\rho\partial\theta} \qquad 2.3(43)$$

$$e_{H_\Phi} = \frac{k_1}{\rho} \frac{\partial(\rho U_1)}{\partial \Theta} \qquad 2.3(44)$$

$$e_{H_\Theta} = \frac{-k_1}{\rho \sin\Theta} \frac{\partial(\rho U_1)}{\partial \Theta} \qquad 2.3(45)$$

$$e_{E_\rho} = \frac{\partial^2(\rho U_1)}{\partial \rho^2} + k^2 \rho U_1 \ . \qquad 2.3(46)$$

Now one has expressed all the components of the electric wave terms of the function U_1 (ρ,Θ,Φ). The same can be done for the magnetic wave case where ${}^{m}E_\rho = 0$ by starting with Eq. 2.3(18), going to 2.3(22 and 23), then to 2.3(21), and finally getting the wave equation in 2.3(19-20). Expressions will be obtained which are similar to 2.3(42-46), but involve U_2, the magnetic potential, instead of U_1. The two functions U_1 and U_2 are scalar potentials that are sometimes called "Debye potentials" (Debye, 1909). Both potentials are obviously solutions to the wave equation:

$$\nabla^2 U_i + k^2 U_i = 0 \qquad (i=1,2). \qquad 2.3(47)$$

The complete fields will be made up of a combination of the electric and magnetic waves solutions. From

the procedure just outlined one can arrive at the following expressions for the field components:

$$E_\rho = {}^{e}E_\rho + {}^{m}E_\rho = \frac{\partial^2(\rho U_1)}{\partial \rho^2} + k^2 \rho U_1 \qquad 2.3(48)$$

$$E_\Theta = {}^{e}E_\Theta + {}^{m}E_\Theta = \frac{1}{\rho}\frac{\partial^2(\rho U_1)}{\partial \rho \partial \Theta} + \frac{k_2}{\rho \sin\Theta}\frac{\partial(\rho U_2)}{\partial \Phi} \qquad 2.3(49)$$

$$E_\Phi = {}^{e}E_\Phi + {}^{m}E_\Phi = \frac{1}{\rho \sin\Theta}\frac{\partial^2(\rho U_1)}{\partial \rho \partial \Phi} - \frac{k_2}{\rho}\frac{\partial(\rho U_2)}{\partial \Theta} \qquad 2.3(50)$$

$$H_\rho = {}^{m}H_\rho + {}^{e}H_\rho = k^2 \rho U_2 + \frac{\partial^2}{\partial \rho^2}(\rho U_2) \qquad 2.3(51)$$

$$H_\Theta = {}^{m}H_\Theta + {}^{e}H_\Theta = \frac{-k_1}{\rho \sin\Theta}\frac{\partial(\rho U_1)}{\partial \Phi} + \frac{1}{\rho}\frac{\partial^2(\rho U_2)}{\partial \rho \partial \Theta} \qquad 2.3(52)$$

$$H_\Phi = {}^{m}H_\Phi + {}^{e}H_\Phi = \frac{k_1}{\rho}\frac{\partial(\rho U_1)}{\partial \Theta} + \frac{1}{\rho \sin\Theta}\frac{\partial^2(\rho U_2)}{\partial \rho \partial \Phi} \qquad 2.3(53)$$

From the boundary conditions given in 2.3(24-27) and from 2.3(49-50) and 2.3 (52-53), one can see that the four quantities given below must be continuous across the surface of the sphere:

$$k_1\rho U_1, \quad k_2\rho U_2, \quad \frac{\partial}{\partial\rho}(\rho U_1), \quad \frac{\partial}{\partial\rho}(\rho U_2). \qquad 2.3(54)$$

This observation indicates the independence of the electric and magnetic waves. Because of this independence, the problem of solving the diffraction by a sphere is reduced to finding two mutually independent solutions to 2.3(47) with the stated boundary conditions.

Eq. 2.3(41) is a partial differential equation in spherical coordinates to which the standard separation of variables technique can be applied with

$$U = R(\rho)T(\theta)F_o(\phi). \qquad 2.3(55)$$

This results in the separated equations

$$\frac{d^2(\rho R)}{d\rho^2} + \left(k^2 - \frac{\alpha_1}{\rho^2}\right) \rho R = 0 \qquad 2.3(56)$$

$$\frac{1}{\sin\theta}\frac{d}{d\theta}\left(\sin\theta\frac{dT}{d\theta}\right) + \left(\alpha_1 - \frac{\beta_1}{\sin^2\theta}\right) T = 0 \qquad 2.3(57)$$

$$\frac{d^2F}{d\phi^2} + \beta_1 F_o = 0 . \qquad 2.3(58)$$

The derivation of these equations may be found in Born and Wolf (1959), or Shifrin (1968). Any of the separation constants which appear must satisfy the requirement that $\underset{\sim}{E}$ and $\underset{\sim}{H}$ are single-valued functions of position. For each of the preceding equations it is possible to write down the corresponding general equation. These equations are:

$$\frac{d^2Z}{d\bar{\rho}^2} + \frac{1}{\bar{\rho}}\frac{dZ}{d\rho} + \left[1+\frac{(\ell+1/2)^2}{(\bar{\rho})^2}\right] Z=0 \qquad 2.3(59)$$

$$\left[\bar{\rho}=k\rho\,, R(r)=\frac{1}{\sqrt{\bar{\rho}}}\, Z(\bar{\rho})\right]$$

$$(1-\eta_o^2)\frac{d^2T}{d\eta_o^2} - 2\mu\frac{dT}{d\eta_o} + \left[\ell(\ell+1) - \frac{m^2}{1-\eta_o^2}\right] T=0 \qquad 2.3(60)$$

$$(\eta_o=\cos\Theta)$$

$$a\cos\left(\beta_1^{1/2}\Phi\right) + b\sin\left(\beta_1^{1/2}\Phi\right) = 0. \qquad 2.3(61)$$

The conditions of single valuedness requires that $\beta_1=m^2$ where m is an integer, and $\alpha_1=\ell(\ell+1)$ where $\ell>|m|$. The solutions to 2.3(60) are associated Legendre polynomials of degree ℓ and order m. The solutions are finite at the poles where $\mu=\pm 1$ and they are periodic in θ. They may be expressed as

$$T = P_{\ell}^{m} (n_o). \qquad 2.3(62)$$

A convenient review of the properties of associated Legendre polynomials is given in Chapman and Bartels (1940).

The solution to 2.3(59) is a general cylindrical function of order $\ell+1/2$:

$$Z = \frac{1}{\bar{\rho}} Z_{\ell+1/2} (\bar{\rho}) . \qquad 2.3(63)$$

Of the cylindrical functions (Abramowitz and Stegun, (1963), only those of the first kind, $J_{\ell+1/2}(\bar{\rho})$ are finite at zero and can be used within the sphere. To represent the scattered field outside the sphere only the Hankel functions can be used since they vanish at infinity in the complex plane. The Hankel functions are a combination of Bessel and Neumann functions and are expressed as follows where J represents the Bessel function, N is a Neumann function, and H^1 and H^2 represent Hankel functions of the first and second kind, respectively. They can be written:

$$H_p^1 = J_p + iN_p \qquad 2.3(64)$$

$$H_p^2 = J_p - iN_p . \qquad 2.3(65)$$

Since the time factor used in this development is $e^{-i\omega t}$, a Hankel function of the first kind is appropriate because it behaves at large $\bar{\rho}$ as $e^{i\bar{\rho}}/\bar{\rho}$. Furthermore, the Riccati-Bessel functions (Van de Hulst, 1957) will be used here because they later prove to be convenient. They are defined as

$$\psi_\ell(\bar{\rho}) = [\frac{\pi\bar{\rho}}{2}]^{1/2} J_{\ell+1/2}(\bar{\rho}), \quad \chi_\ell(\bar{\rho}) = [\frac{\pi\bar{\rho}}{2}]^{1/2} N_{\ell+1/2}(\bar{\rho}),$$

2.3(66)

$$\zeta^1_\ell(\bar{\rho}) = [\frac{\pi\bar{\rho}}{2}]^{1/2} H^{(1)}_{\ell+1/2}(\bar{\rho}), \quad \zeta^2_\ell(\bar{\rho}) = [\frac{\pi\bar{\rho}}{2}]^{1/2} H^{(2)}_{\ell+1/2}(\bar{\rho}).$$

2.3(67)

The total solution must be represented in the form of a superposition of the special solutions already indicated which have some unspecified coefficients that will be determined through the use of the boundary conditions. In particular, the potentials, U_1 and U_2, will be expressed in series composed of the indicated solutions as follows from Eq. 2.3(55).

$$\rho U = \rho \sum_{\ell=0}^{\infty} \sum_{m=-\ell}^{+\ell} \{c_\ell \psi_\ell(\bar{\rho}) + d_\ell \chi_\ell(\bar{\rho})\}\{P^m_\ell(\eta_o)\}\{a\cos(m\Phi) + b\sin(m\Phi)\}.$$

2.3(68)

The incident field is a plane wave propagating in the z' direction and polarized in the x' direction (See Fig. 2.3.1). In spherical coordinates this field may be expressed as follows:

$$E_{\rho}^{(i)} = e^{ik^{(1)}\rho\cos\Theta}\sin\theta\cos\Theta \qquad 2.3(69)$$

$$E_{\Theta}^{(i)} = e^{ik^{(1)}\rho\cos\Theta}\cos\theta\cos\Phi \qquad 2.3(70)$$

$$E_{\Phi}^{(i)} = -e^{ik^{(1)}\rho\cos\Theta}\sin\Phi \qquad 2.3(71)$$

$$H_{\rho}^{(i)} = \frac{ik^{(1)}}{k_2^{(1)}} e^{ik^{(1)}\rho\cos\Theta}\sin\theta\cos\Theta \qquad 2.3(72)$$

$$H_{\Theta}^{(i)} = \frac{ik^{(1)}}{k_2^{(1)}} e^{ik^{(1)}\rho\cos\Theta}\cos\theta\sin\Phi \qquad 2.3(73)$$

$$H_{\Phi}^{(i)} = \frac{ik^{(1)}}{k_2^{(1)}} e^{ik^{(1)}\rho\cos\Theta}\cos\Phi. \qquad 2.3(74)$$

By using the expressions for E_{ρ} and H_{ρ} in 2.3(69), 2.3(72), 2.3(48), and 2.3(51), along with the expansion of a plane wave in terms of Legendre polynomials, one

can arrive at the expressions for the two potentials of the incident wave (the details are given most explicitly in Born and Wolf (1959)):

$$\rho U_1 = \frac{1}{k^{(1)^2}} \sum_{\ell=1}^{\infty} i^{\ell-1} \frac{2\ell+1}{\ell(\ell+1)} \psi_\ell(k_\rho^{(1)}) P_\ell^1(\cos\Theta)\cos\Phi \qquad 2.3(75)$$

$$\rho U_2 = \frac{1}{k^{(1)^2}} \sum_{\ell=1}^{\infty} i^{\ell} \frac{k^{(1)}}{k_2^{(1)}} \frac{2\ell+1}{\ell(\ell+1)} \psi_\ell(k^{(1)}\rho) P_\ell^1(\cos\Theta)\sin\Phi. \qquad 2.3(76)$$

Because of the nature of this solution, it establishes n=1 and b and a in 2.3(61) equal to zero for the electric and magnetic waves, respectively.

By analogy with the expressions for the incident wave and with proper consideration of the behavior of the waves at the origin and at large ρ, the potentials for the transmitted wave (superscripted (t)) and the scattered wave (superscripted (s)) can be also written:

$$\rho U_1^{(t)} = \frac{1}{k^{(2)^2}} \sum_{\ell=1}^{\infty} e A_\ell \psi_\ell(k^{(2)}\rho) P_\ell^1(\cos\Theta)\cos\Phi \qquad 2.3(77)$$

$$\rho U_2^{(t)} = \frac{i}{k^{(2)} k_2^{(2)}} \sum_{\ell=1}^{\infty} {}^{m}A_\ell \psi_\ell (k^{(2)}\rho) P_\ell^1(\cos\Theta)\sin\Phi$$

2.3(78)

$$\rho U_1^{(s)} = \frac{1}{k^{(1)2}} \sum_{\ell=1}^{\infty} {}^{e}B_\ell \zeta_\ell^1 (k^{(1)}\rho) P_\ell^1(\cos\Theta)\cos\Phi$$

2.3(79)

$$\rho U_2^{(s)} = \frac{1}{k^{(1)} k_2^{(1)}} \sum_{\ell=1}^{\infty} {}^{m}B_\ell \zeta_\ell^1 (k^{(1)}\rho) P_\ell^1(\cos\Theta)\sin\Phi \ .$$

2.3(80)

The undetermined coefficients ${}^{e}A_\ell$, ${}^{m}A_\ell$, ${}^{e}B_\ell$, and ${}^{m}B_\ell$, will be determined from the boundary conditions expressed below:

$$\left\{\frac{\partial}{\partial\rho}\left(\rho U_1^{(i)} + \rho U_1^{(s)}\right) = \frac{\partial}{\partial\rho}\left(\rho U_1^{(t)}\right)\right\}_{\rho=a}$$

2.3(81)

$$\left\{\frac{\partial}{\partial\rho}\left(\rho U_2^{(i)} + \rho U_2^{(s)}\right) = \frac{\partial}{\partial\rho}\left(\rho U_2^{(t)}\right)\right\}_{\rho=a}$$

2.3(82)

$$\{k_1^{(1)}(\rho U_1(i)+\rho U_1(s)) = k_1^{(2)}(\rho U_1(t))\}_{\rho=a}$$

2.3(83)

$$\{k_2^{(1)}(\rho U_2(i)+\rho U_2(s)) = k_2^{(2)}\rho U_2(t)\}_{\rho=a} .$$

2.3(84)

When Eqs. 2.3(75-80) are inserted into 2.3(81-84), one obtains, after eliminating ${}^{e}A_{\ell}$ and ${}^{m}A_{\ell}$, the expressions for ${}^{e}B_{\ell}$ and ${}^{m}B_{\ell}$, the scattering coefficients for the scattered wave:

$${}^{e}B_{\ell} = i^{\ell+1}\,\frac{2\ell+1}{\ell(\ell+1)}\,\frac{k_2^{(1)}k^{(2)}\psi_\ell'(k^{(1)}a)\psi_\ell(k^{(2)}a)-k_2^{(2)}k^{(1)}\psi_\ell'(k^{(2)}a)\psi_\ell(k^{(1)}a)}{k_2^{(1)}k^{(2)}\zeta_\ell^{1\prime}(k^{(1)}a)\psi_\ell(k^{(2)}a)-k_2^{(2)}k^{(1)}\psi_\ell'(k^{(2)}a)\zeta_\ell^{1}(k^{(1)}a)}$$

2.3(85)

$${}^{m}B_{\ell} = i^{\ell+1}\,\frac{2\ell+1}{\ell(\ell+1)}\,\frac{k_2^{(1)}k^{(2)}\psi_\ell(k^{(1)}a)\psi_\ell'(k^{(2)}a)-k_2^{(2)}k^{(1)}\psi_\ell'(k^{(1)}a)\psi_\ell(k^{(2)}a)}{k_2^{(1)}k^{(2)}\zeta_\ell^{1}(k^{(1)}a)\psi_\ell'(k^{(2)}a)-k_2^{(2)}k^{(1)}\zeta_\ell^{1\prime}(k^{(1)}a)\psi_\ell(k^{(2)}a)} .$$

2.3(86)

The prime ($'$) on a function denotes differentiation with respect to the argument.

The components of the field vectors of the scattered wave are obtained upon substituting 2.3(79) and 2.3(80) into 2.3(48-53). The results are:

$$E_\rho^{(s)} = \frac{1}{k^{(1)2}} \frac{\cos\Phi}{\rho=} \sum_{\ell=1}^{\infty} \ell(\ell+1)\, {}^{e}B_\ell \zeta_\ell^1(k^{(1)}\rho) P_\ell^1(\cos\theta) \qquad 2.3(87)$$

$$E_\theta^{(s)} = \frac{-1}{k^{(1)}} \frac{\cos\Phi}{\rho} \sum_{\ell=1}^{\infty} \{ {}^{e}B_\ell \zeta_\ell^{1\prime}(k^{(1)}\rho) P_\ell^{1\prime}(\cos\theta)\sin\theta \qquad 2.3(88)$$

$$-i({}^{m}B_\ell)\zeta_\ell^1(k^{(1)}\rho) P_\ell^1(\cos\theta)\frac{1}{\sin\theta}\}$$

$$E_\Phi^{(s)} = \frac{-1}{k^{(1)}} \frac{\sin\Phi}{\rho} \sum_{\ell=1}^{\infty} \{ {}^{e}B_\ell \zeta_\ell^{1\prime}(k^{(1)}\rho) P_\ell^1(\cos\theta)\frac{1}{\sin\theta} \qquad 2.3(89)$$

$$-i({}^{m}B_\ell)\zeta_\ell^1(k^{(1)}\rho) P_\ell^{1\prime}(\cos\theta)\sin\theta\}$$

$$H_\rho^{(s)} = \frac{-1}{k^{(1)}k_2^{(1)}} \frac{\sin\Phi}{\rho^2} \sum_{\ell=1}^{\infty} \{\ell(\ell+1)\, {}^{m}B_\ell \zeta_\ell^1(k^{(1)}\rho) P_\ell^1(\cos\theta)\} \qquad 2.3(90)$$

$$H_\theta^{(s)} = \frac{-1}{k_2^{(1)}} \frac{\sin\Phi}{\rho} \sum_{\ell=1}^{\infty} \{ {}^{e}B_\ell \zeta_\ell^1(k^{(1)}\rho) P_\ell^1(\cos\theta)\frac{1}{\sin\theta} \qquad 2.3(91)$$

$$+i({}^{m}B_\ell)\zeta_\ell^{1\prime}(k^{(1)}\rho) P_\ell^{1\prime}(\cos\theta)\sin\theta\}$$

$$H_\Phi^{(s)} = \frac{1}{k_2^{(1)}} \frac{\cos\Phi}{\rho} \sum_{\ell=1}^{\infty} \{ {}^{e}B_\ell \zeta_\ell^1(k^{(1)}\rho) P_\ell^{1\prime}(\cos\theta)\sin\theta \qquad 2.3(92)$$

$$+i({}^{m}B_\ell)\zeta_\ell^{1\prime}(k^{(1)}\rho) P_\ell^1(\cos\theta)\frac{1}{\sin\theta}\}.$$

If one now lets

$$x = k^{(1)}a = \frac{2\pi a}{\lambda} \qquad 2.3(93)$$

$$m_o = \frac{k^{(2)}k_2^{(1)}}{k^{(1)}k_2^{(2)}} \qquad 2.3(94)$$

$$k^{(2)}a = m_o x \qquad 2.3(95)$$

$$\sigma^{(1)} = 0 , \quad \sigma^{(2)} = \sigma \qquad 2.3(96)$$

$$\varepsilon^{(1)} = 1 . \qquad 2.3(97)$$

Then the scattering coefficients take the form:

$$e_{B_\ell} = i^{\ell+1} \frac{2\ell+1}{\ell(\ell+1)} \frac{m_o\psi_\ell'(x)\psi_\ell(m_o x)-\psi_\ell(x)\psi_\ell'(m_o x)}{m_o\zeta_\ell^{1\prime}(x)\psi_\ell(m_o x)-\zeta_\ell^1(x)\psi_\ell'(m_o x)}$$

$$= i^{\ell+1} \frac{2\ell+1}{\ell(\ell+1)} a_\ell^{(s)} \qquad 2.3(98)$$

$$m_{B_\ell} = i^{\ell+1} \frac{2\ell+1}{\ell(\ell+1)} \frac{m_o \psi_\ell(x)\psi_\ell'(m_o x) - \psi_\ell'(x)\psi_\ell(m_o x)}{m_o \zeta_\ell^1(x)\psi_\ell'(m_o x) - \zeta_\ell^{1\prime}(x)\psi_\ell(m_o x)}$$

$$= i^{\ell+1} \frac{(2\ell+1)}{\ell(\ell+1)} b_\ell^{(s)} \quad . \qquad 2.3(99)$$

In Eqs. 2.3(87) and 2.3(90) one can note the $E_\rho^{(s)}$ and $H_\rho^{(s)}$ decay as $\frac{1}{\rho^2}$ rather than $\frac{1}{\rho}$ as in the case of the other components. Therefore, at large ρ one may disregard the radial components and consider the scattered field as a spherical wave. At large ρ the expressions, $\zeta_\ell'(\bar{\rho})$ and $\zeta_\ell^{1\prime}(\bar{\rho})$ can be approximated by the following formulas:

$$\zeta_\ell^1(\bar{\rho}) \simeq (-i)^{\ell+1} e^{i\bar{\rho}} \qquad 2.3(100)$$

$$\zeta_\ell^{1\prime}(\bar{\rho}) \simeq (-i)^{\ell} e^{i\bar{\rho}}. \qquad 2.3(101)$$

When Eqs. 2.3(100-101) are substituted into 2.3(88-89), the resulting expressions are:

$$E_\theta^{(s)} = \frac{-ie^{ik^{(1)}\rho\cos\Phi}}{k^{(1)}\rho} \sum_{\ell=1}^{\infty} \frac{2\ell+1}{\ell(\ell+1)} \{b_\ell^{(s)} \frac{P_\ell^1(\cos_\Theta)}{\sin\Theta} + a_\ell^{(s)} \frac{dP_\ell^1(\cos\Theta)}{d\Theta}\}$$

$$2.3(102)$$

$$E_{\Phi}^{(s)} = \frac{ie^{ik^{(1)}\rho}\sin\Phi}{k^{(1)}\rho} \sum_{\ell=1}^{\infty} \frac{2\ell+1}{\ell(\ell+1)} \{b_{\ell}^{(s)} \frac{dP_{\ell}^{1}(\cos\Theta)}{d\Theta} + a_{\ell}^{(s)} \frac{P_{\ell}^{1}(\cos\Theta)}{\sin\Theta}\}.$$

2.3(103)

If one defines

$$\pi_{\ell}(\cos\Theta) = \frac{P_{\ell}^{1}(\cos\Theta)}{\sin\Theta} \quad ,$$

and

$$\tau_{\ell}(\cos\Theta) = \frac{d}{d\Theta} (P_{\ell}^{1}(\cos\Theta)) \quad ,$$

then 2.3(102) and 2.3(103) can be written as

$$E_{\Theta}^{(s)} = \frac{-ie^{ik^{(1)}\rho}\cos\Phi}{k^{(1)}\rho} \sum_{\ell=1}^{\infty} \frac{2\ell+1}{\ell(\ell+1)} (b_{\ell}^{(s)}\pi_{\ell} + a_{\ell}^{(s)}\tau_{\ell})$$

$$= \frac{ik_2^{(1)}}{k^{(1)}} H_{\Phi}^{(s)} = H_{\Phi}^{(s)} \qquad 2.3(104)$$

$$E_{\Phi}^{(s)} = \frac{ie^{ik^{(1)}\rho}\sin\Phi}{k^{(1)}\rho} \sum_{\ell=1}^{\infty} \frac{2\ell+1}{\ell(\ell+1)} (b_{\ell}^{(s)}\tau_{\ell} + a_{\ell}^{(s)}\pi_{\ell})$$

$$= \frac{ik_2^{(1)}}{k^{(1)}} H_{\Theta}^{(s)} = -H_{\Theta}^{(s)} \quad . \qquad 2.3(105)$$

In 2.3(104) and 2.3(105) it is now appropriate to define the following functions (Van de Hulst, 1957):

$$S_1(\Theta) = \sum_{\ell=1}^{\infty} \frac{2\ell+1}{\ell(\ell+1)} \left(a_\ell^{(s)} \pi_\ell + b_\ell^{(s)} \tau_\ell\right) \qquad 2.3(106)$$

$$S_2(\Theta) = \sum_{\ell=1}^{\infty} \frac{2\ell+1}{\ell(\ell+1)} \left(a_\ell^{(s)} \tau_\ell + b_\ell^{(s)} \pi_\ell\right) . \qquad 2.3(107)$$

These functions will be used extensively in Chapter III as the basis for computations involving intensity and polarization.

2.4. The Intensity and Polarization

The intensity of a wave is proportional to the square of its amplitude ($I \propto |E|^2$; see Born and Wolf, 1959, Chapter 1) so that one can see from 2.3(104-105) that

$$I_1 = |E_\Phi^{(s)}|^2 = \frac{I_o}{k^2 (1)^2 \rho^2} |S_1|^2 \sin^2\Phi \qquad 2.4(1)$$

$$I_2 = |E_\Theta^{(s)}|^2 = \frac{I_o}{k^2 (1)^2 \rho^2} |S_2|^2 \cos^2\Phi . \qquad 2.4(2)$$

If one lets

$$i_1 = |S_1|^2 \qquad 2.4(3)$$

$$i_2 = |S_2|^2 \qquad 2.4(4)$$

then one has for 2.4(1) and 2.4(2)

$$I_1 = \frac{I_o i_1}{k^{(1)}_{\rho^2}} \sin^2\Phi \qquad 2.4(5)$$

$$I_2 = \frac{I_o i_2}{k^{(1)}_{\rho^2}} \cos^2\Phi \qquad 2.4(6)$$

where i_1 and i_2 are the dimensionless intensity functions commonly encountered in the literature. Φ in this formulation denotes the angle between the polarized component of the incident wave and the scattering plane containing the directions of propagation of the incident and scattered rays.

If the incident radiation is natural light (unpolarized), then one has to take an average of $\cos^2\Phi$ and $\sin^2\Phi$ over all inclinations to the scattering plane. For both cases

$$\overline{\cos^2\Phi} = \overline{\sin^2\Phi} = 1/2 \; . \qquad 2.4(7)$$

Therefore, for unpolarized incident radiation,

$$I = \frac{i_1+i_2}{2k^{(1)}_{\rho^2}} I_o \; . \qquad 2.4(8)$$

The scattered light in any direction will have a partial linear polarization that can be written (Van de Hulst, 1957):

$$POL = \frac{i_1 - i_2}{i_1 + i_2} \quad . \qquad 2.4(9)$$

2.5. The Scattering Coefficient

It is frequently necessary to evaluate the total amount of light scattered by a sphere. To do this it is necessary to evaluate the Poynting vector which expresses the energy in the incident wave. The time average of the Poynting vector is given by Born and Wolf, (1959) as

$$\bar{S} = \frac{c}{8\pi} \mathrm{Re}(\underset{\sim}{E} \times \underset{\sim}{H}^*) \qquad 2.5(1)$$

where Re stands for the real part of the complex result and (*) denotes the complex conjugate. As has been indicated before, when a plane monochromatic wave strikes a particle in a dielectric medium, the field at any point in the medium (it has been assumed to be a vacuum) can be represented as the sum of the incident and scattered fields:

$$\underset{\sim}{E} = \underset{\sim}{E}^{(i)} + \underset{\sim}{E}^{(s)} \qquad 2.5(2)$$

$$\underset{\sim}{H} = \underset{\sim}{H}^{(i)} + \underset{\sim}{H}^{(s)} \quad . \qquad 2.5(3)$$

Considering this fact, the Poynting vector given above can be split into three components:

$$\bar{S} = \overline{S^{(i)}} + \overline{S^{(s)}} + \overline{S'} \quad . \qquad 2.5(4)$$

$\overline{S^{(i)}}$ is the incident flux, $\overline{S^{(s)}}$ is the scattered flux, and $\overline{S'}$ is the flux produced by the interference of the incident and scattered radiation.

If one draws about the sphere a concentric spherical surface of radium p_1, then the total flux directed outwards through this sphere will be the integral of the radial component of $\bar{S}$ with respect to the sphere. The radial component of $\bar{S}$ is:

$$\bar{S}_R = \frac{c}{8\pi} (E_\Theta H^*_\Phi - E_\Phi H^*_\Theta) \quad . \qquad 2.5(5)$$

By virtue of 2.5(2-3), this can be broken up into the three components indicated by 2.5(4):

$$\overline{S_R} = \frac{c}{8\pi} \{(E^{(i)}_\Theta H^{*(i)}_\Phi - E^{(i)}_\Phi H^{*(i)}_\Theta) + (E^{(s)}_\Theta H^{*(s)}_\Phi - E^{(s)}_\Phi H^{*(s)}_\Theta)$$

$$+ (E^{(i)}_\Theta H^{*(s)}_\Phi + E^{(s)}_\Theta H^{*(i)}_\Phi - E^{(i)}_\Phi H^{*(s)}_\Theta - E^{(s)}_\Phi H^{*(s)}_\Theta)\} \quad .$$

$$2.5(6)$$

When it is necessary to find the total energy scattered by the sphere, one integrates the second group of terms on the right of 2.5(6) over all solid angles as indicated below:

$$W_s = \frac{c}{8\pi} \mathrm{Re}\int_0^{\pi} \int_0^{2\pi} (E_\theta^{(s)} H_\phi^{*(s)} - E_\phi^{(s)} H_\theta^{*(s)}) \rho^2 \sin\theta d\theta d\phi \ . \qquad 2.5(7)$$

One then uses the expressions given by Eqs. 2.3(104-105) and the following orthogonality relationships:

$$\int_0^{\pi} \left(\frac{dP_n^1}{d\theta} \frac{dP_m^1}{d\theta} + \frac{1}{\sin^2\theta} P_n^1 P_m^1 \right) \sin\theta d\theta = \begin{cases} 0 \text{ if } n \neq m \\ \frac{2n(n+1)}{(2n+1)} \frac{(n+1)!}{(n-1)!} \text{ if } n=m \end{cases} \qquad 2.5(8)$$

and

$$\int_0^{\pi} \left(\frac{P_m^1}{\sin\theta} \frac{dP_n^1}{d\theta} + \frac{P_n^1}{\sin\theta} \frac{dP_m^1}{d\theta} \right) \sin\theta d\theta = 0 \ . \qquad 2.5(9)$$

When these manipulations are accomplished properly the expression for the scattered energy is:

$$W_s = \frac{c}{4\pi} \frac{\pi}{k^{(1)2}} \sum_{\ell=1}^{\infty} (2\ell+1) \left(|a_\ell^{(s)}|^2 + |b_\ell^{(s)}|^2\right) .$$

2.5(10)

The scattering cross-section C_5 is defined (Stratton, 1941) as the ratio of the total scattered energy per second to the energy density of the incident wave. If the energy in the incident wave is $c/8\pi$, ($|E^{(i)}|$ has been assumed equal to 1 in this development), then according to this definition above,

$$C_s = \frac{2\pi}{k^{(1)2}} \sum_{\ell=1}^{\infty} (2\ell+1) \left(|a_\ell^{(s)}|^2 + |b_\ell^{(s)}|^2\right) .$$

2.5(11)

When the ratio of C_s to the geometrical cross section (πa^2) is taken, then the efficiency factor (Van de Hulst, 1957) or normalized cross section can be written:

$$Q_s = \frac{2}{x^2} \sum_{\ell=1}^{\infty} (2\ell+1) \left(|a_\ell^{(s)}|^2 + |b_\ell^{(s)}|^2\right) . \qquad 2.5(12)$$

This is the same expression as is given by Deirmendjian and Clasen (1962).

2.6. The Scattering Coefficient and Intensity Functions for a Polydispersed Particulate Volume.

For a cloudy atmosphere it is necessary to compute the volume scattering coefficient (β_ν) that has already been discussed in section 2.1. This can be done, using the scattering cross section or efficiency factor defined above, if the particles in the volume are spaced randomly and the distance between the particles is large compared to the wavelength. These stipulations are important in order to assume that the scattering is incoherent. A mathematical expression for the volumetric scattering coefficient is

$$\beta_\nu = \int_0^\infty \pi a^2 Q_s(a) n(a) da \simeq \int_{a_1}^{a_2} \pi a^2 Q_s(a) n(a) da \qquad 2.6(1)$$

where n(a) is an expression describing the size distribution of the particles comprising the volume. More will be said in Chapter III about the selection of a size distribution that is representative of the stratus clouds discussed in Chapter I.

For a polydispersed suspension, the elements P_1 and P_2 discussed in section 2.1 can be expressed as follows using the dimensionless intensity functions i_1 and i_2,

and the volume scattering coefficient β_ν (Deirmendjian and Clasen, 1962):

$$P_j = \frac{4\pi}{\beta_\nu} \int_o^\infty n(a) i_j(m_o, a, \theta) da \qquad (j=1,2) \ . \tag{2.6(2)}$$

These intensity functions, P_j, for the volume must be properly normalized so as to employ them in the equation of radiative transfer. The required normalization condition is

$$\frac{1}{4\pi} \int_o^\pi \int_o^{2\pi} \left(\frac{P_1+P_2}{2}\right) d\Omega = 1 \tag{2.6(3)}$$

The equations and functions which have been developed and described up to this point will now be used to numerically generate single scattering results that are representative of those to be expected from stratus clouds. The procedures used and the results achieved are described in Chapter III along with comments concerning the various processes that interact to produce the anisotropy in reflected radiation over stratus clouds described in Chapter I.

Chapter III

SINGLE AND MULTIPLE SCATTERING RESULTS - COMPUTED AND OBSERVED

3.1. Difficulties in Numerically Simulating Observed Results.

From the theoretical framework given in Chapter II it is evident that in order to simulate the results given for stratus clouds in Chapter I, a valid approach would be to apply the equation of radiative transfer to a model of a cloudy atmosphere in such a way as to arrive at results similar to the ones actually observed. This process would involve finding the appropriate phase matrix (or matrices), making the elements of the phase matrix compatible to the equation of radiative transfer by expressing them in a series involving the proper coordinates, and then either finding the scattering and transmission matrices described by Chandrasekhar (1960) or integrating the equation of radiative transfer numerically through the cloud as suggested by Herman (1964) until the appropriate reflected and transmitted intensities are achieved. The essential difficulty with the above problem is that the scattering from stratus cloud droplets is highly anisotropic. This is because the incident light is scattered by particles as large or larger than the wavelength. Consequently the mathematical description and manipulation of the appropriate expressions is quite complex.

A further problem exists in that many instruments do not detect monochromatic radiation, but instead monitor the radiation over a bandwidth that may be quite wide as is the case of the broad bandpass on the MRIR. Because of the varying properties of scattering particles with relation to the radiation incident upon them, it is difficult to suggest and justify a single phase matrix which would assure that numerical representation of scattering from a model cloud would be representative of that actually observed by a bandpass spanning a wide range of wavelengths.

One final difficulty to be considered here occurs when one starts to select a droplet size distribution that is representative of the cloud, or cloud type, to be modeled. There are two contributing factors to this problem. On the one hand, the droplet size distribution in a cloud varies in both time and space depending upon the environmental conditions existing before and during the formation and evolution of the cloud. On the other hand, the accuracy of methods used to sample clouds and their associated droplet size distributions and liquid water contents are somewhat controversial (Aufm Kampe, 1950; Eldridge, 1957; Fletcher, 1962; Mason, 1957; Hodkinson, 1966; Shrifrin and Perelman, 1966).

3.2. Procedure

In view of the problems implicitly and explicitly posed above, it was decided to see how much the intensity

functions and the polarization of singly scattered light would vary for different droplet size distributions across the wavelength region defined by the narrow bandpass of the MRIR. This meant computing the functions $P_1/4\pi$ and $P_2/4\pi$ defined in Eqs. 2.6(2) in Chapter II and POL as defined in the next equation for the wavelengths and drop-size distributions to be specified:

$$POL = \frac{P_1 - P_2}{P_1 + P_2} \quad . \qquad 3.2(1)$$

The overall purpose of pursuing these objectives is to better understand the role of particle size distributions and droplet concentrations in producing the observed anisotropy over stratus clouds described in Chapter I.

The narrow bandpass was selected because the complex index of refraction m_o has only a real part across all the wavelengths from 0.55 - 0.85μ (Centeno, 1941). The value of the index of refraction to two decimal places according to the above reference is 1.33. Furthermore, the radiometer relative response curve (see Fig. 1.2.3) is sharply peaked at 0.620μ. This meant that a good evaluation of the variation in $P_1/4\pi$, $P_2/4\pi$, and POL could be achieved by examining their behavior at the wavelengths corresponding to the two 50% relative response points and the 100% relative response point. By making this strategic selection of points the necessary computer time to achieve the results

was shortened to an amount which was within the amount of time obtainable for this project.

In order to compute the functions indicated, it was necessary to find recursion relationships which could be adapted to the computer and enable one to compute the elements of Eqs. 2.5(12), 2.4(3), and 2.4(4). In particular, the recursion relationships for the functions, S_1 and S_2, in Eqs. 2.3(106) and 2.3(107) were necessary and important. The most readily available and usable recursion relationships for this purpose were those published by Deirmendjian and Clasen (1962). The derivation of the formulas listed in the above reference can be found in Lowan (1948), Gucker and Cohn (1953), Infeld (1947), and Aden (1951). The necessary computer program needed to produce the results indicated above was written by the author for the Control Data Corporation 6400 at Colorado State University. The program was checked against the results given in Deirmendjian and Clasen (1962), Gumprecht and Sliepcevich (1951), and Penndorf and Goldberg (1956). In all cases the program gave as good or better accuracy than the results given in the above references.

In order to evaluate Eq. 2.6(2) it was necessary to select a droplet size distribution that was representative of a stratus cloud. This entailed reviewing the literature to ascertain what values of drop size, droplet concentration, and liquid water content had been found in stratus clouds similar to those found on and along the western

coast of the United States. Furthermore, it was necessary to select a mathematical expression which would adequately describe the droplet size distributions observed in stratus clouds.

From Fletcher (1962), Mason (1957), Feigel'son (1966), Tverskoi (1965), Neiburger (1949), Neiburger and Wurtele (1949), Neiburger and Chien (1960), Okita (1962) Arnulf, et al. (1957), and Griggs and Marggraf (1967) it was concluded that the average liquid water content of stratus clouds were near 0.3 - 0.4 g m^{-3}. The range in droplet concentration varied widely, but was generally between 10 and 600 droplets per cm^3. The range in drop sizes varied also, but the instances where larger droplets prevailed corresponded roughly to the instances with low droplet concentrations. Commonly the droplet radii were between 1 and 40μ and the modal radii were between 4 and 10μ.

Several choices for a mathematical expression describing the observed conditions were also available including the normal, log normal, ordinary gamma, and the generalized gamma distribution (Tverskoi, 1965). The last distribution has been advocated as being the most versatile and representative of the choices and has been used by Deirmendjian (1964) to represent haze and cloud particle distributions.

The distribution has the general form:

$$n(a) = a_o a^{\alpha} \exp(-ba^{\gamma}) \cdot \qquad 3.2(2)$$

where a_o, γ, b, and α are positive constants.

By choosing α and γ one can determine a_o and b by selecting the droplet concentration and model radius of the desired droplet distribution. After choosing α and γ, one first differentiates Eq. 3.2(2) so that

$$\frac{d}{da} n(a) = a_o a^{\alpha-1} \exp(-ba^{\gamma}) \ (\alpha - \gamma b a^{\gamma}) \qquad 3.2(3)$$

When this is set equal to zero, then

$$b = \alpha/(\gamma a_m^{\gamma}) \qquad 3.2(4)$$

where a_m is the modal radius. From b, one can get a_o by integrating 3.2(2) as follows (Korn and Korn, 1968):

$$N' = \int_o^{\infty} n(a)da = \frac{a_o}{\gamma} b^{-(\frac{\alpha+1}{\gamma})} \Gamma \left(\frac{\alpha+1}{\gamma}\right) . \qquad 3.2(5)$$

N' is the droplet concentration and Γ denotes the gamma function. When one solves for a_o, the result is:

$$a_o = \frac{\gamma N' b^{-(\frac{\alpha+1}{\gamma})}}{\Gamma(\frac{\alpha+1}{\gamma})} \quad . \qquad 3.2(6)$$

In order to determine the value of the constants for a distribution that would fit as well as possible the observed properties of a stratus cloud, another computer program was written by the author which allowed systematic variation of a_o, b, α, and γ until the desired distribution was achieved. Three different distributions were eventually selected to describe a large number of the droplet size distributions and concentrations observed in stratus clouds. These distributions are shown in Fig. 3.2.1 along with their associated model drop size, droplet concentration, and liquid water content. The distributions were chosen in such a way as to have the liquid water content remain nearly constant while the model drop size and droplet concentration varied. In general, as the concentration of the droplets increased, the modal drop size and the number of large droplets decreased as would be expected.

As a further check on the computational procedure, the droplet distribution for a cumulus cloud proposed by Deirmendjian (1964) was used and β_ν $\frac{P_1}{4\pi}$, and $\frac{P_2}{4\pi}$ computed for several values of the scattering angle. This cumulus droplet size distribution has the following form:

$$n(a) = 2.373\ a^6 \exp(-1.5a) \ . \qquad 3.2(7)$$

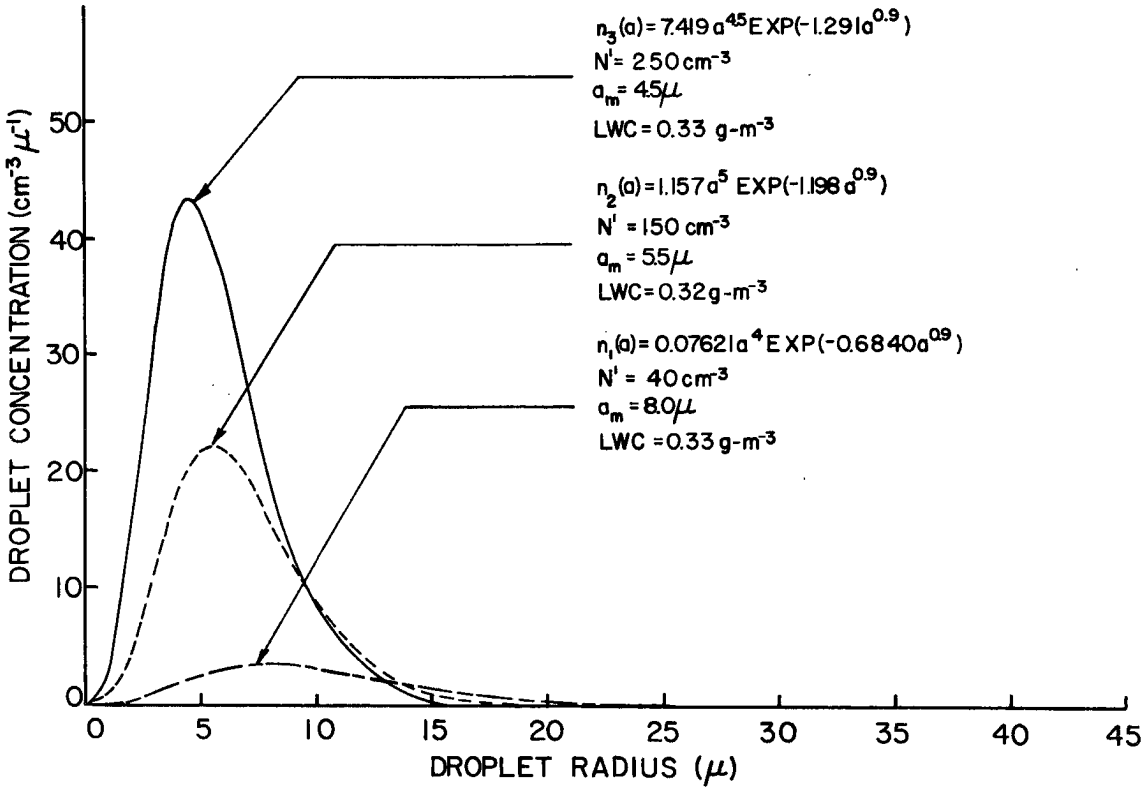

Fig. 3.2.1. Droplet size distributions used in computing intensity and polarization versus scattering angle at wavelengths of 0.573, 0.620, and 0.740 microns.

The results of this computation were checked against those in the same reference and found to agree. Deirmendjian further showed that the results will start to converge when the upper limits in the integration of Eqs. 2.6(1-2) become larger than the following:

$$a_2 > a_m\left(1+\frac{4}{\gamma}\right)^{1/\gamma} . \qquad 3.2(8)$$

This is a rather indefinite criteria; therefore, for the computations described here the upper limit of integration corresponds to the radius where the number of droplets per cm^3 per micron is slightly less than or equal to 0.01.

A few trial computations using the cumulus distribution (Eq. 3.2(7)) showed that even on a fast computer such as the CDC 6400 the resulting computations were significantly long and expensive. This was particularly true for a distribution such as n_1 shown in Fig. 3.2.1 where there were large droplets present. Therefore, to get as much significant information as possible with the least computer time, the computations were performed only at the three points on the radiometer response curve already mentioned. These points corresponded to wavelengths of 0.573, 0.620, and 0.740 microns. It was judged that the droplet distribution n_1 corresponded most closely to the stratus clouds on the western coast of the United States since these

clouds were in a maritime environment and the distribution n_1 has maritime characteristics (Fletcher, 1962). This distribution agrees most closely with cloud droplet measurements taken in maritime environments such as those by Okita (1962). Therefore, the volumetric scattering coefficients, etc., were calculated using this drop-size distribution at all three wavelengths. In order to evaluate the effect of a change in drop distributions and concentrations, the same parameters were calculated at 0.620μ using the n_2 and n_3 distributions.

To further shorten the computing time necessary to perform the computations already described, it was next necessary to decide on the method for numerically integrating Eqs. 2.6(1-2). As a first step the variable of integration was changed from a to x, the size parameter, as suggested by Deirmendjian (1964) and Bullrich (1964). When this is done, Eqs. 2.6(1-2) appear as follows:

$$\beta_\nu = \pi \int_{x_1}^{x_2} x^2 f(x,k^{(1)}) Q(m_o,x)\,dx \qquad 3.2(9)$$

$$\frac{P_j}{4\pi} = \frac{1}{\beta_\nu} \int_{x_1}^{x_2} f(x,k^{(1)})\, i_j(m_o,x,\Theta)\,dx \,. \qquad 3.2(10)$$

$$(j=1,2)$$

The function $f(x,k^{(1)})$ results from the change of variable in Eq. 3.2.1:

$$f(x,k^{(1)}) = a_o(k^{(1)})^{-3-\alpha}x^{\alpha}\exp(-b(\frac{x}{k^{(1)}})^{\gamma} \quad . \qquad 3.2(11)$$

Having accomplished the change of variable from a to x it was then necessary to choose the integration interval (s) for x and decide at which values of the scattering angle the computations should be performed. The computations at selected values of Θ were performed in the following increments:

$$\Theta = 1(1)10(5)130(2)180, \qquad 3.2(12)$$

i.e., the computations were performed in one degree increments from 1-10 degrees, five degree increments from 10-130 degrees, and two degree increments from 130-180 degrees. These choices were made so as to shorten the necessary computation time and still properly describe the resulting curves showing intensity or polarization versus scattering angle. The integration steps over x were performed as indicated in Table 3.2.1. Several trial computations were made before deciding upon these integration steps over x.

Table 3.2.1 A summary describing computations of $P_1/4\pi$, $P_2/4\pi$, and POL versus Θ for three different wavelengths and droplet size distributions.

Wavelength(μ)	Size Distribution	Range in Radius(μ)	Integration Intervals over x	Computer Time Required (min.)
0.573	n_1	0.5-33.5	5(0.5)100(1.0)250(2.0)368	60
0.620	n_1	0.5-33.5	5(0.5)100(1.0)250(2.0)340	53
0.740	n_1	0.5-33.5	5(0.5)100(1.0)250(2.0)286	45
0.620	n_2	0.5-23.5	5(0.5)100(1.0)240	37
0.620	n_3	0.1-21.5	1(0.5)100(1.0)218	30

3.3. Results and Discussion

The results of the calculations summarized in Table 3.2.1 are given in Figs. 3.3.1-5. On each diagram the size distribution, droplet concentration (N'), modal radius (a_m), liquid water content (LWC), and the volumetric scattering coefficient (β_v) are given. Examination of Figs. 3.3.1-3 reveals that very little change occurs in the intensity functions and the polarization versus scattering angle. The most readily observed changes in the intensity functions occur at $\Theta=0^o$ and $\Theta=100^o$. From the way in which the integrations were conducted, one can see that the variation observed at the three wavelengths could also have been observed at one wavelength by varying the upper limit of integration. This observation emphasizes the role of the large droplets in determining these characteristics of scattered light. The small changes and the nature of the radiometer response curve indicate that the functions $P_1/4\pi$ and $P_2/4\pi$ at 0.620μ could be used as elements of a phase matrix appropriate for further computations representing expected light scattering results observed with the narrow MRIR bandpass.

When the wavelength was held constant and the droplet size distribution varied, more noticeable changes in the intensity functions and polarization were observed (Figs. 3.3.3-5). The largest changes in the intensity functions again occurred at $\Theta=0^o$ and near $\Theta=100^o$. As the droplet concentration increased and the modal droplet

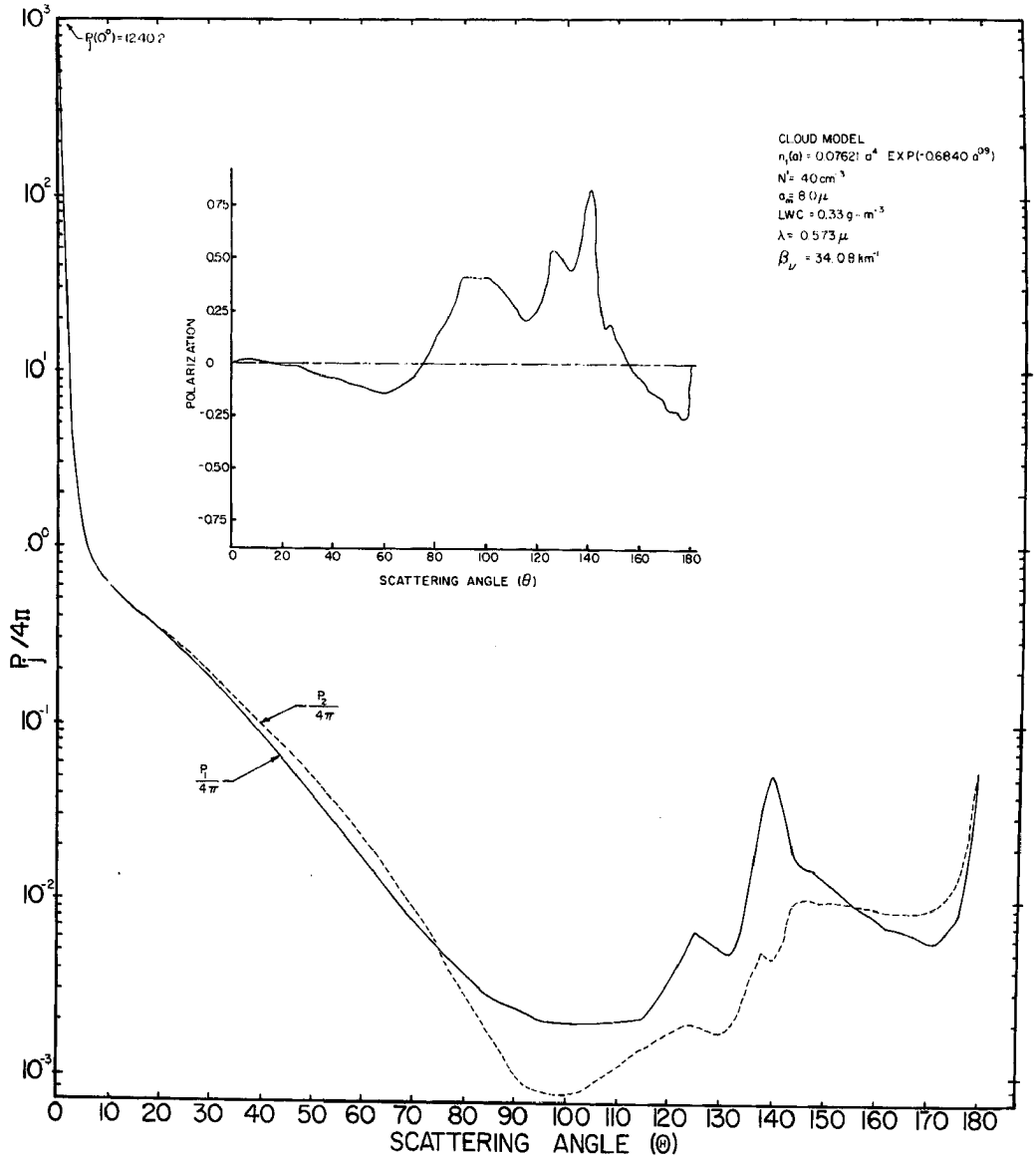

Fig. 3.3.1 The intensity functions and polarization versus scattering angle for a cloudy volume with the n_1 droplet distribution illuminated by radiation of 0.573μ wavelength.

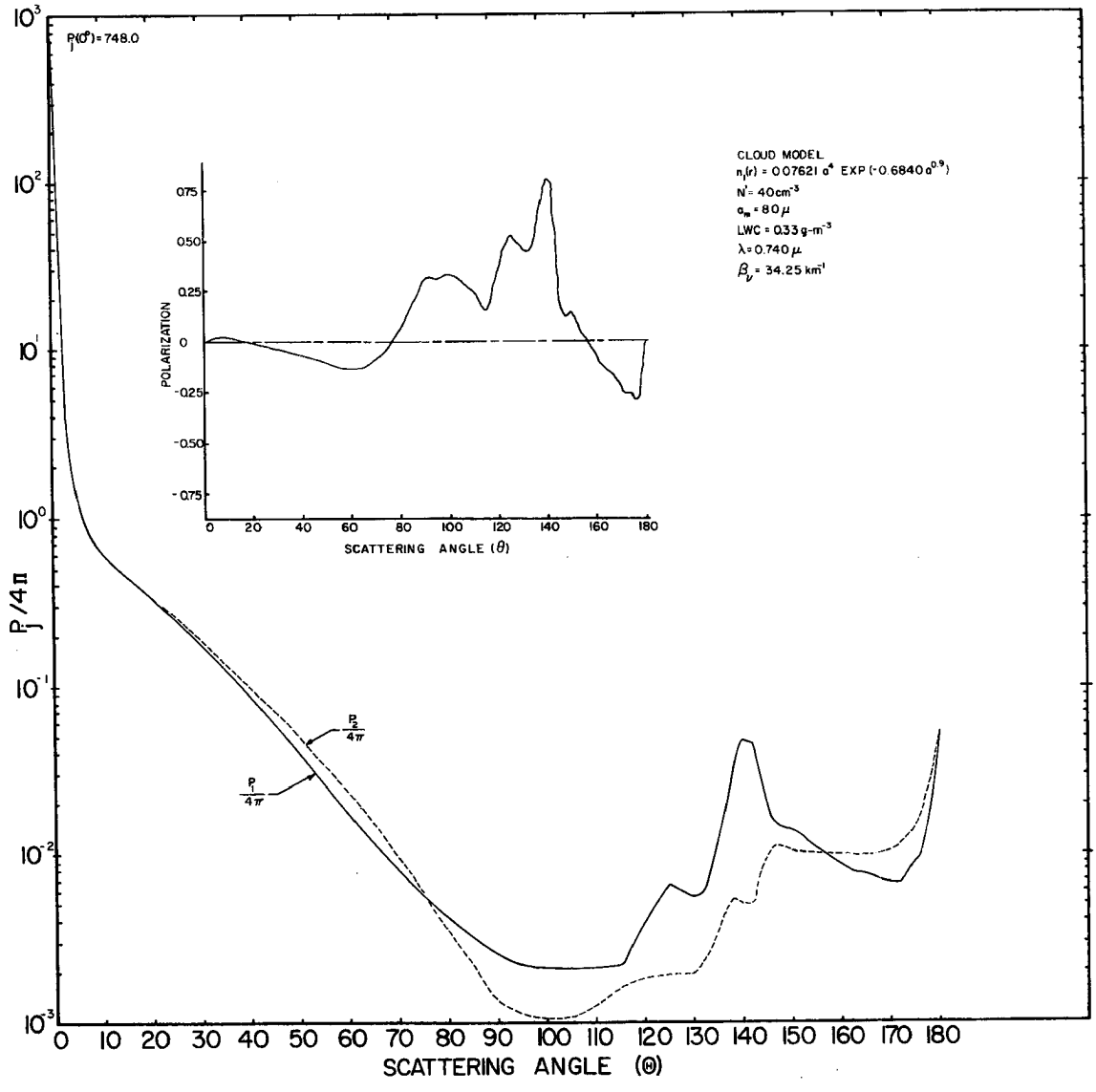

Fig. 3.3.2. The intensity functions and polarization versus scattering angle for a cloudy volume with the n_1 droplet distribution illuminated by radiation of 0.740μ wavelength.

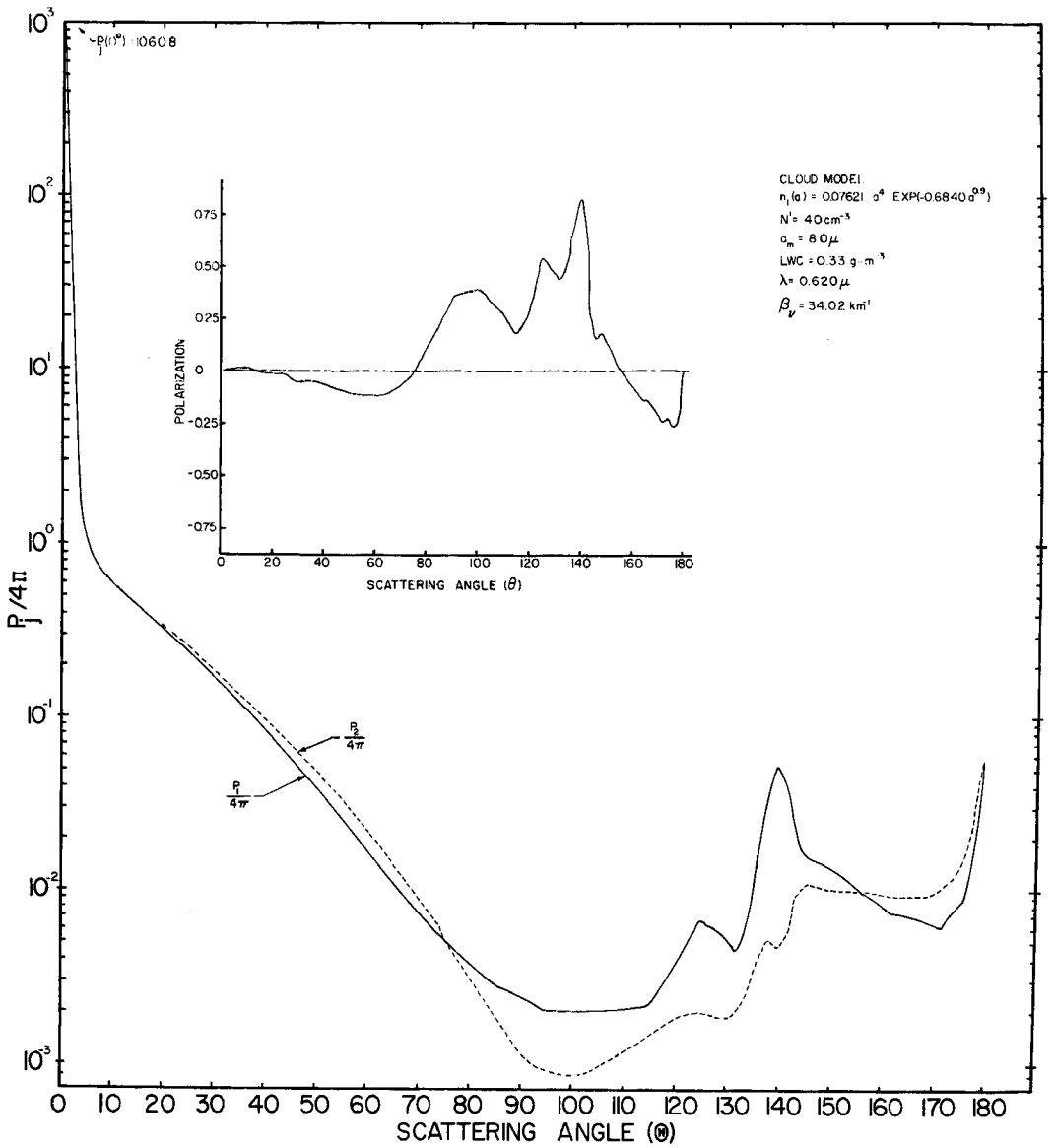

Fig. 3.3.3. The intensity functions and polarization versus scattering angle for a cloudy volume with the n_1 droplet distribution illuminated by radiation of 0.620μ wavelength.

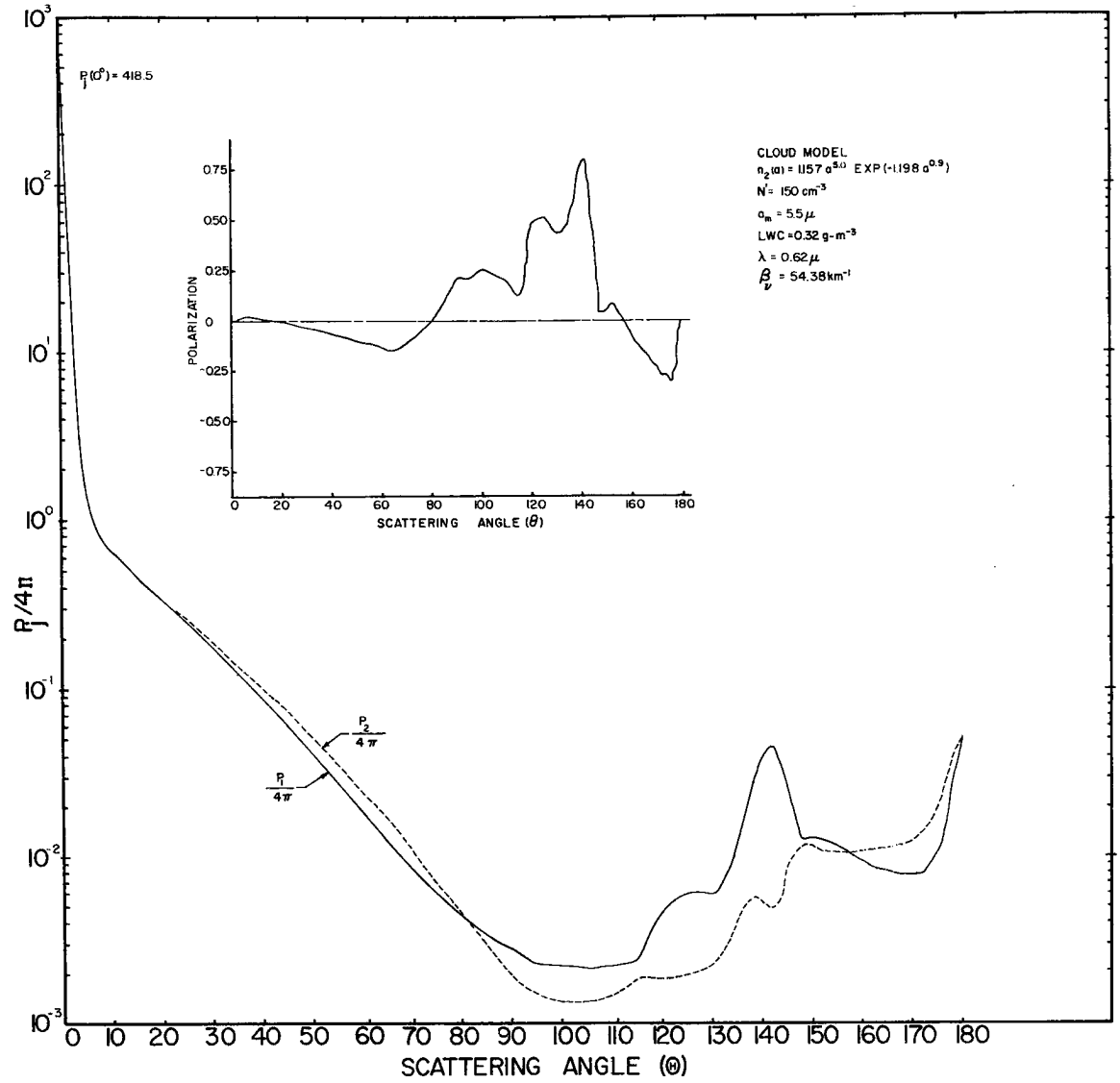

Fig. 3.3.4. The intensity functions and polarization versus scattering angle for a cloudy volume with the n_2 droplet distribution illuminated by radiation of 0.620μ wavelength.

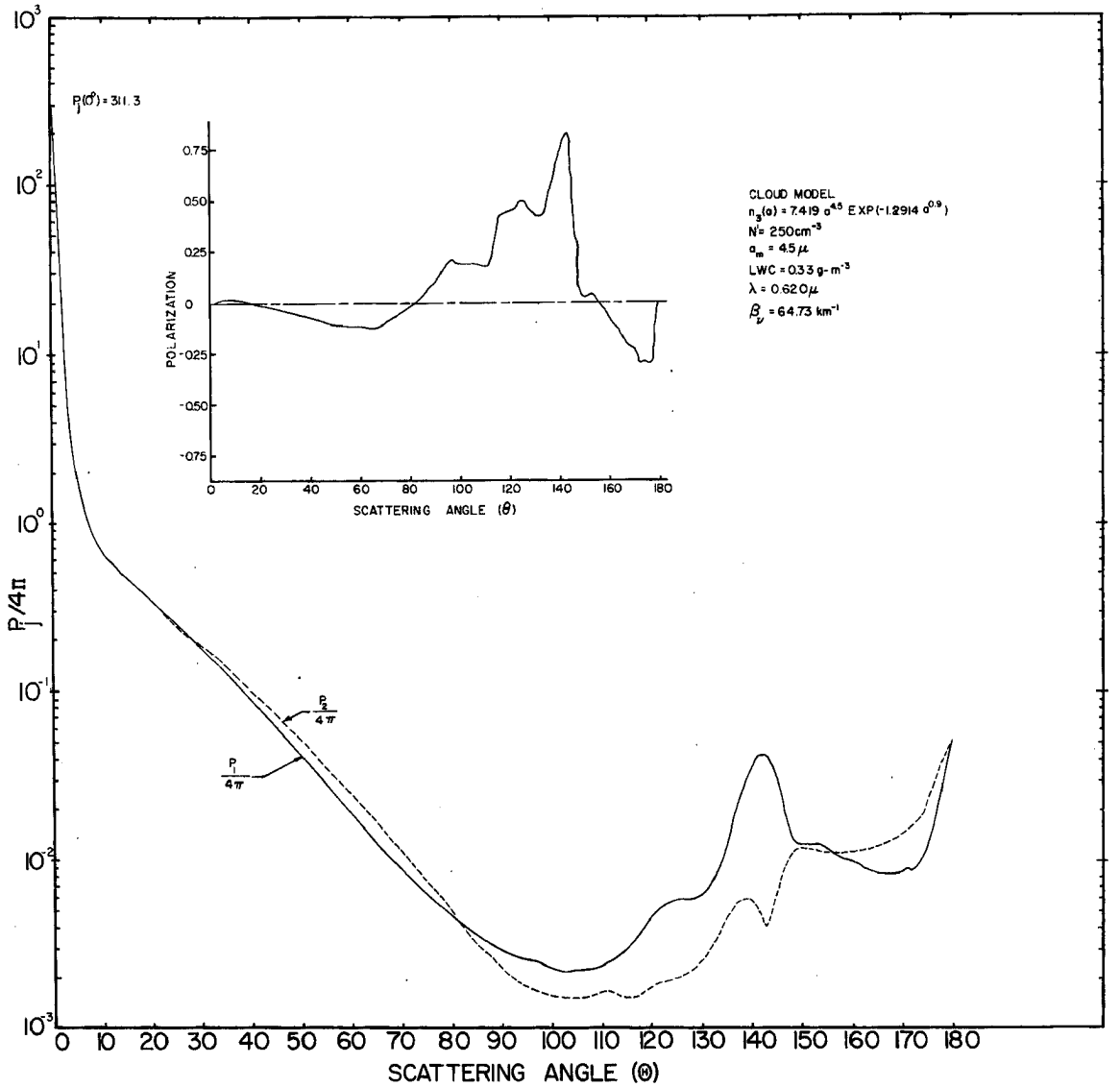

Fig. 3.3.5. The intensity functions and polarization versus scattering angle for a cloudy volume with the n_3 droplet distribution illuminated by radiation of 0.620μ wavelength.

size became smaller, the forward peak intensity dropped, the intensity near $\Theta=100^{o}$ increased, and the maximum in $P_1/4\pi$ near $\Theta=125^{o}$ became less pronounced. The most pronounced polarization changes occurred near $\Theta=100^{o}$. The polarization in the fogbow (Minnaert, 1954) near 140-143^{o} and the intensity and polarization near $\Theta=180^{o}$ changed very little.

It is clear from the observations stated above that if one angle were to be chosen at which the most change would be observed for the purposes of remotely detecting changes in droplet distribution, an angle near $\Theta=100^{o}$ would have to be that choice for these wavelengths since both the intensity and polarization were observed to change at this location. If only intensity were to be observed, the greatest changes would occur at, or near, $\Theta=0^{o}$ for the types of variations seen here. A greater number of diagrams such as those in Figs. 3.3.1-5 need to be produced at other wavelengths extending into the near infrared before any definite conclusions can be made as far as remote sensing possibilities are concerned. Computations involving several other drop size distributions and liquid water contents need to be made also.

The results do serve to emphasize a point made by Bullrich (1964) who pointed out that in order to use scattered light characteristics to infer such parameters as particle size distribution, liquid water content, etc., it is very helpful to make measurements of the polarization

of the scattered light. If the characteristics of scattered light are to be used to infer all the unique characteristics of a particulate volume, it is likely that measurements will have to be made at several angles with respect to the incident beam and at several wavelengths. However, under carefully specified conditions it may not be necessary to go to the degree of complexity implied above depending upon the accuracy and amount of information desired (Davies, 1966, pp. 350-351).

3.4. A Comparison of Observed and Computed Results

There are some obvious differences between the single scattering results described in this chapter and the observed results over stratus clouds in Chapter I. One notable difference is the absence in the observed results of the maxima in the computed single scattering results near $\Theta=140^{o}$. This latter feature was looked for very carefully in the observed results inasmuch as the white fogbow has occasionally been observed under natural conditions (Minneart, 1954). No such fogbow could conclusively be observed, however, even when the results were converted so as to show reflectance versus scattering angle. Deirmendjian (1964) has pointed out that there would be many more coronas, fogbows, etc., in the single scattering results if the size distribution were uniform. The non-uniform particle size distribution serves to minimize or cause the disappearance of many of these effects.

Multiple scattering apparently plays a predominant role in producing the lesser anisotropy in the observed results versus the single scattering results. This hypothesis can be substantiated by a comparison of numerical results simulating multiple scattering in a model cloud and the observed results which are affected by multiple scattering. There are very few published theoretical results involving multiple scattering from clouds because of the complexity of the problem. Some recent results of this kind, however, have been published by Twomey et. al. (1967), Plass and Kattawar (1968), and Kattawar and Plass (1968a,b). In the last cases authored by Kattawar and Plass, the elegant approach outlined by Chandrasekhar (1960) and suggested in Chapter II has been bypassed and an approach used which utilizes the powerful Monte Carlo statistical method. This approach enables simulation of multiple scattering in clouds at nearly any optical depth, no matter how anisotropic the single scattering intensity function.

A comparison of the computed results by Kattawar and Plass (1968a,b) was performed in order to see how much agreement exists. The results of this comparison are illustrated in Figs. 3.4.1-3. In the Kattawar and Plass results all reflected radiances within 90^{o} of the incident beam had been averaged in order to get the distributions shown in Figs. 3.4.1-3. This was also done for the observed results. Since droplet size

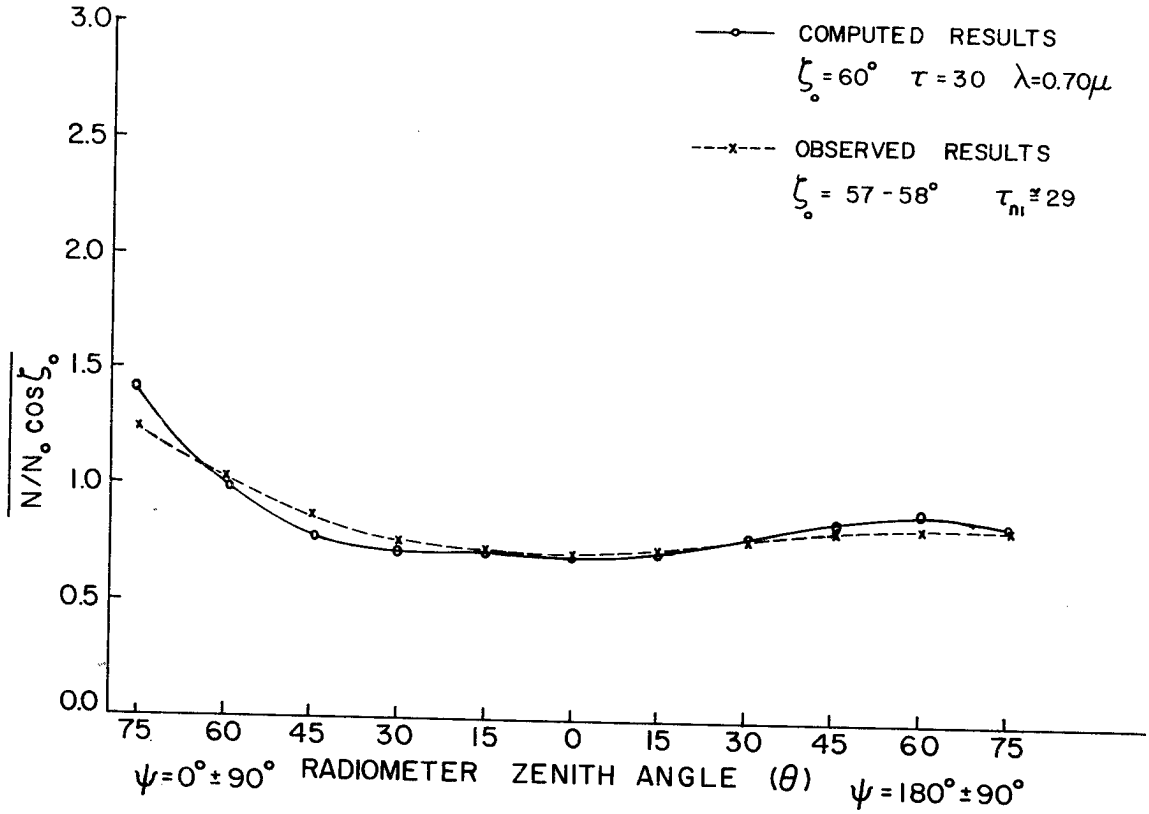

Fig. 3.4.1. A comparison of the results observed by the narrow bandpass of the MRIR over stratus clouds on 14 December 1966 and computed multiple scattering results from Kattawar and Plass (1968a, Fig. 3) using a cumulus cloud droplet distribution.

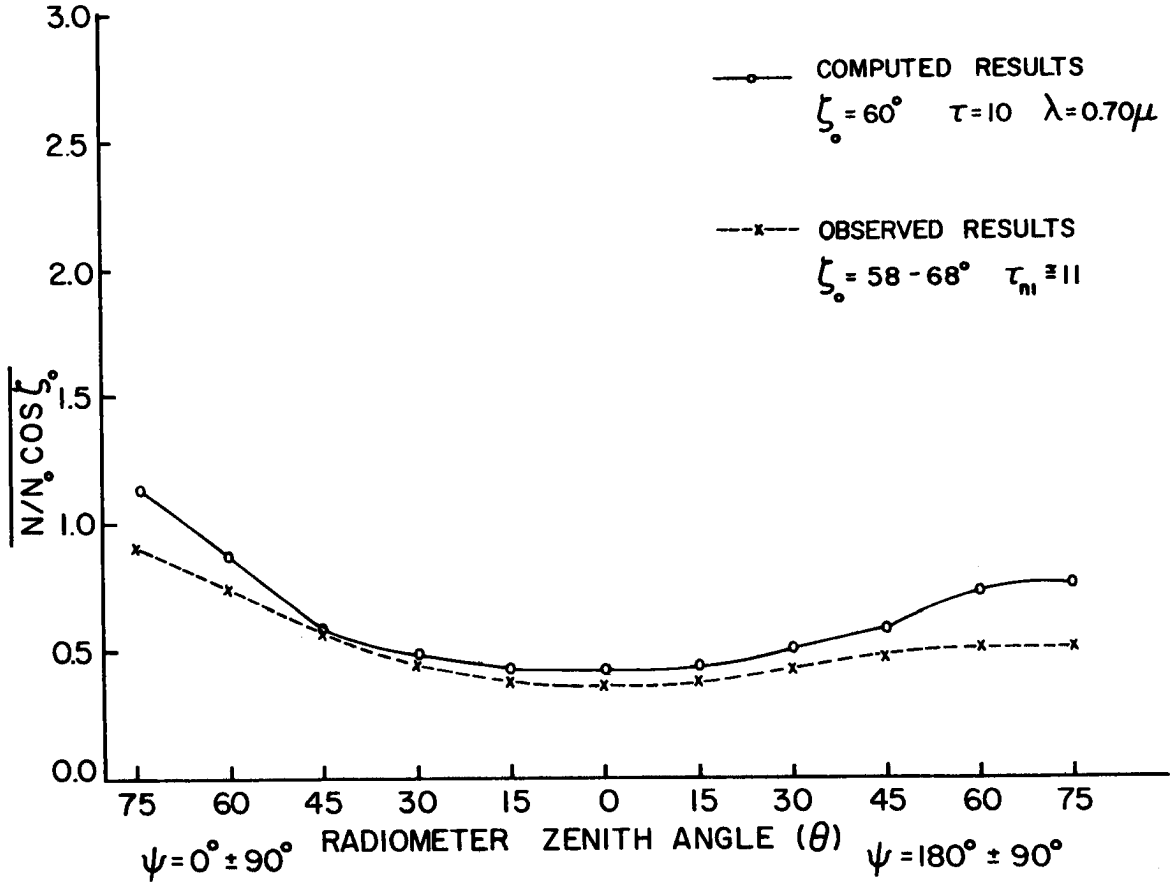

Fig. 3.4.2. A comparison of the results observed by the narrow bandpass of the MRIR over stratus clouds on 11 June 1965 and computed multiple scattering results from Kattawar and Plass (1968a, Fig. 3) using a cumulus cloud droplet distribution.

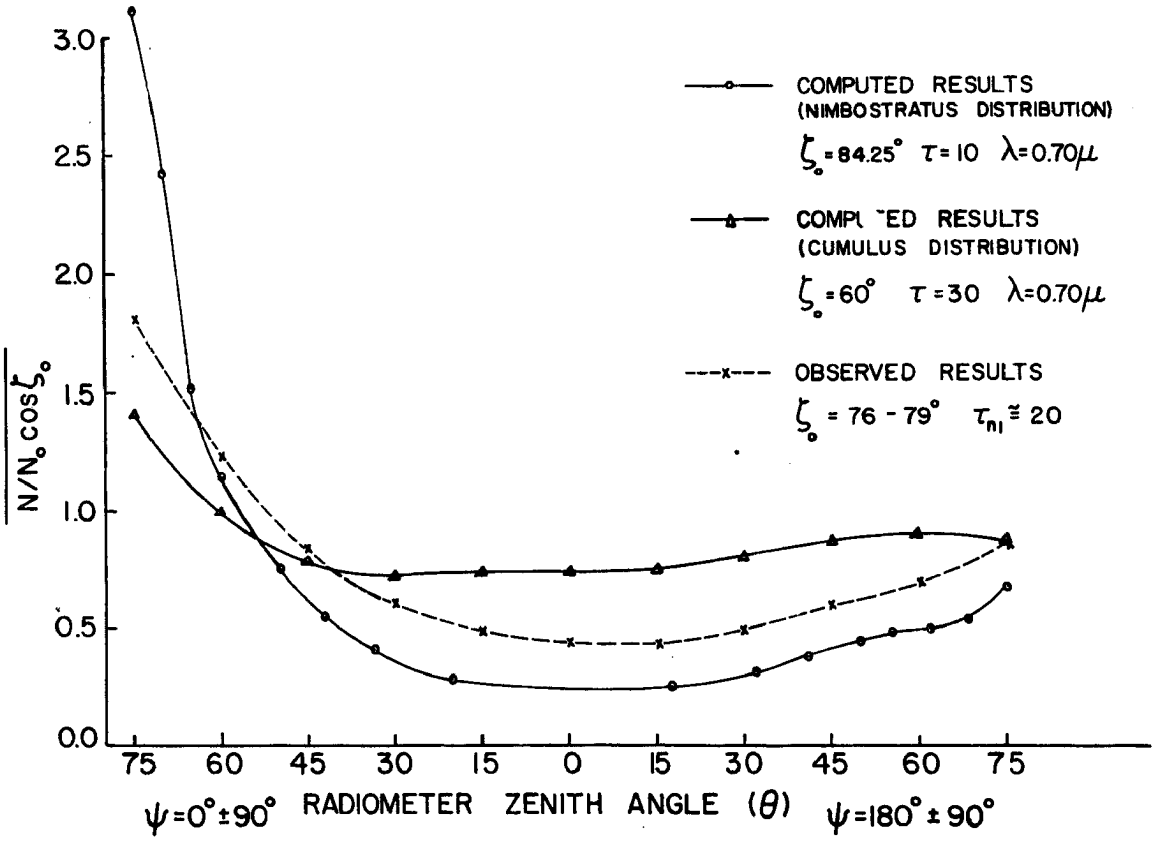

Fig. 3.4.3. A comparison of the results observed by the narrow bandpass of the MRIR over stratus clouds on 15 December 1966 and computed multiple scattering results from Kattawar and Plass (1968a, Fig. 3; 1968b, Fig. 8) using cumulus and nimbostratus cloud droplet distributions.

distribution n_1 was believed to be the most representative of stratus clouds on the western coast of the United States, this distribution and the computed β_ν were used to estimate the optical depth τ of the observed clouds. This was done by using the equation,

$$\tau = \beta_\nu h \qquad 3.4(1)$$

where h is the thickness of the cloud in kilometers. The result of this computation is given in each of the diagrams referred to above.

Figs. 3.4.1-3 show good agreement between the observed and calculated results. The agreement is much better in the cases shown here than in previously published comparisons of the same kind (Ruff et.al., 1968). The closer agreement demonstrated here is largely due to a better match of the actual cloud characteristics and the cloud model used in the computed results. The agreement is rather remarkable insofar as the amount of anisotropy in the observed and computed results is concerned. If it were possible to define more accurately the illumination conditions and the existing characteristics of the observed clouds, it is felt that even more consistent agreement between the two situations would be evident.

The agreement of the results above certainly emphasizes the predominant role that multiple scattering has in smoothing out single scattering effects and reducing

the anisotropy in single scattering results. At large optical depths the relative insensitivity of the reflectance distributions to different particle size distributions is evident in Figs. 3.4.1-3. This observation agrees with conclusions and results published by Twomey et. al. (1967) and by Kattawar and Plass (1968b).

Chapter IV

A SUMMARY AND RECOMMENDATIONS FOR FURTHER RESEARCH

4.1. Summary

In Chapter I observational results were presented which showed that appreciable anisotropy in reflected solar radiation exists for a wide variety of surfaces contributing substantially to the planetary albedo. This directional variation in reflectance was found to be different for each surface, but was consistently related to the features characterizing each individual reflecting surface. The anisotropy for all surfaces was observed to increase with increasing solar zenith angle. Clouds and snow at large solar zenith angles exhibited pronounced reflection going away from the sun and stratus clouds also exhibited a lesser increase in reflection back toward the sun.

The magnitude of the reflectances in isolated portions of the solar spectrum were observed to change from surface to surface. These changes were primarily influenced by the spectral reflectivity of the surfaces, but were also influenced by atmospheric attenuation and the spectral response characteristics of the observing radiometer.

It was concluded that scattering from the atmosphere itself had a small, but significant, influence on the observed results. This influence was most evident in reflectivities observed near the horizon that were higher

than might be predicted from laboratory measurements of reflected radiances over similar surfaces.

In the case of scattering from stratus clouds, it was observed that the thickness of the clouds and the reflectivity of the surface beneath the clouds affected the directional reflectance distributions and their magnitudes. The reflectances over stratus clouds underlain by snow were observed to be much higher than those from stratus clouds underlain by water. When the thickness of a cloud increased, the integrated directional reflectances were also observed to increase. Varying thicknesses in the observed clouds were found to also affect the relative differences between reflectances observed in different portions of the solar spectrum.

It was clear from these observations that in order for accurate evaluation of the albedo of individual surfaces, or of the planetary albedo, to be made from satellite radiometers with a limited field of view, the effects of anisotropy, spectral reflectivity, and the intervening atmosphere must be considered and evaluated. The relative importance of each of these effects depends upon the particular way in which the data from the satellite radiometer is to be applied.

In Chapter II the theory that is necessary in order to appreciate and understand the mathematical complexity involved in describing radiative transfer in cloudy atmospheres was outlined and developed in some detail. The

developments given were linked together and described in sufficient detail to provide the required background and equations for numerically evaluating the major factors and processes which interact and produce the anisotropy in the reflected radiances over stratus clouds in a maritime environment.

Chapter III described the way in which the theory and equations developed in Chapter II were used to generate single scattering results that showed the effects of different droplet size distributions, droplet concentrations, and wavelengths on intensity and polarization results. These results were found to be the most sensitive at scattering angles near 0 and 100 degrees to changes in the characteristics of a cloudy volume. The variation in intensities and polarization across the wavelengths defined by the narrow bandpass of the MRIR were observed to be relatively small. The variation was small enough to conclude that the intensity functions computed at the 100 percent relative response point corresponding to this bandpass could be used in any future attempts to simulate numerically the narrow bandpass observations over stratus clouds.

A comparison of the observed results and some published multiple scattering results showed that multiple scattering exerts a pronounced smoothing influence on the reflected intensities predicted by single scattering results from polydispersed particulate volumes. The observed and calculated results agreed closely enough to conclude that

if the characteristics of a cloud model and the observed clouds were matched, the correspondence would be very close. The comparisons that were made showed particularly good agreement between the anisotropy predicted by the theoretical results and that observed over stratus clouds.

4.2. Recommendations

It is clear that more airborne observations of the anisotropy and the spectral variation in reflectance from a variety of surfaces is desirable. Measurements with a polarimeter of the characteristics of light reflected and transmitted by clouds would be invaluable. Concurrent measurements of the droplet size distributions, droplet concentrations, and liquid water content need to be made so as to define the structure of a cloud as it exists at the time that observations of reflected and transmitted radiances are made.

Measurements defining more precisely the influence of the intervening atmosphere between an airborne radiometer and the reflecting surface need to be made also. If measurements were made of intensity, polarization, and haze particle concentrations and sizes at several levels in the atmosphere, the eventual results would be of great interest.

All the measurements suggested above should be supported by further theoretical calculations describing the scattering of absorption of solar radiation in the atmosphere. More

studies need to be made evaluating the effects of various distributions and concentrations of haze on the transfer of solar radiation in theoretical models of the atmosphere. The calculations should also include the effects of multiple scattering and the anisotropic reflectance and absorption of the many different terrestrial surfaces existing at the lower boundary of the earth's atmosphere.

The results of the studies suggested above should be applied to any and all studies utilizing satellite observations to determine the albedo of individual terrestrial surfaces and the planetary albedo.

REFERENCES

Abramowitz, M., and I.A. Stegun, 1964: Handbook of mathematical functions. Applied Mathematics Series No. 55, National Bureau of Standards, U.S. Department of Commerce, 953 pp.

Aden, A.L., 1951: Electromagnetic scattering from spheres with sizes comparable to the wavelength. Journal of Applied Physics, 22, 601-605.

Ambartsumyan, V.A., 1958: Theoretical Astrophysics, London, Pergamon Press, 645 pp.

Arnulf, A., J. Bricard, E. Air'e, and C. Ve'ret, 1957: Transmission by haze and fog in the spectral region 0.35 to 10 microns. Journal of the Optical Society of America, 47, 491-498.

Aufm Kampe, H.J., 1950: Visibility and liquid water content in clouds in the free atmosphere. Journal of Meteorology, 7, 54-57.

Bandeen, W.R., H. Halev, and I. Strange, 1965: A radiation climatology in the visible and infrared from TIROS meteorological satellites. National Aeronautics and Space Administration, Washington, D.C., Technical Note D-2534, 30 pp.

Bartman, F.L., 1966: The calibration of and interpretation of data from 0.55-0.85 micron and 0.2-4.0 micron channels of the F-1 and F-4 MRIR radiometers. Ann Arbor, University of Michigan, Technical Report, Contract NASr 54(03), 86 pp.

_____, 1967: The reflectance and scattering of solar radiation by the earth. Ann Arbor, University of Michigan, Technical Report, Contract NASr-54(03), 257 pp.

Beckmann, P., and A. Spizzichino, 1963: The Scattering of Electromagnetic Waves from Rough Surfaces, New York, Pergamon Press, 503 pp.

Born, M., and E. Wolf, 1959: Principles of Optics, New York, Pergamon Press, 803 pp.

Bullrich, K., 1964: Scattered radiation in the atmosphere. Advances in Geophysics, 10, 99-260.

Busbridge, I.W., 1960: The Mathematics of Radiative Transfer, London, Cambridge University Press, 143 pp.

Centeno, M., 1941: The refractive index of liquid water in the near infra-red spectrum. Journal of the Optical Society of America, 31, 244-247.

Chandrasekhar, S., 1960: Radiative Transfer, New York, Dover Publications Inc., 393 pp.

Chapman, S., and J. Bartels, 1940: Geomagnetism, Volume II, Oxford, Clarendon Press, pp. 606-638.

Chen, Hsi-shu, C.R. Nagaraza Rao, and Z. Sekera, 1967: Investigations of the polarization of light reflected by natural surfaces. Los Angeles, University of California, Department of Meteorology, Contract AF 19(628)-3850, Project No. 7621, Task No. 762103, Scientific Report No. 2, 96 pp.

Coulson, K.L., 1966: Effects of reflection properties of natural surfaces in aerial reconnaissance. Applied Optics, 5, 905-917.

_____, G.M. Bouricus, and E.L. Gray, 1965: Optical reflection properties of natural surfaces. Journal of Geophysical Research, 70, 4601-4611.

_____, E.L. Gray, and G.M. Bouricus, 1966: Effect of surface reflection on planetary albedo. Icarus, 5, 139-148.

Davies, C.N., 1966: Aerosol Science, New York, Academic Press, 468 pp.

Debye, P., 1909: De lichtdruck auf kugeln von beliebegem material. Annalen Der Physik, 30, 57-136.

Deirmendjian, D., 1964: Scattering and polarization properties of water clouds and hazes in the visible and infrared. Applied Optics, 3, 187-196.

_____, and R.J. Clasen, 1962: Light scattering on partially absorbing homogeneous spheres of finite size. Santa Monica, The Rand Corporation, Report No. R-393-PR, 44 pp.

Dirmhirn, I., 1967: On the applicability of silicon cells in atmospheric radiation studies. Fort Collins, Colorado State University, Department of Atmospheric Science, Paper No. 113, 33 pp.

Eldridge, R.G., 1957: Measurement of cloud drop size distributions, Journal of Meteorology, 14, 55-59.

Feigel'son, E.M., 1966: Light and Heat Radiation in Stratus Clouds, Jerusalem, Israel Program for Scientific Translations, 245 pp.

Fletcher, N.H., 1962: The Physics of Rain Clouds, London, Cambridge University Press, 386 pp.

Godske, C.L.S., T. Bergeron, J. Bjerknes, and R.C. Bundgaard, 1957: Dynamic Meteorology and Weather Forecasting, Boston, American Meteorological Society, 800 pp.

Griggs, M., and W.A. Marggraf, 1967: Measurement of cloud reflectance properties and the atmospheric attenuation of solar and infrared energy. San Diego, Convair Division of General Dynamics, Final Report, Contract No. AF 19(628)-5517, Project No. 6698, Task No. 669803, Work Unit No. 66980301, 153 pp.

Gucker, F.T. Jr., and S.H. Cohn, 1953: Numerical evaluation of the Mie scattering functions; table of the angular functions π_n and τ_n of orders 1 to 32 at 2.5^0 intervals. Journal of Colloid Science, 8, 555-561.

Gumprecht, R.O., and C.M. Sliepcevich, 1951: Light Scattering Functions for Spherical Particles, Ann Arbor, University of Michigan, Michigan Engineering Research Institute, 574 pp.

Hapke, B., and H. Van Horn, 1963: Photometric studies of complex surfaces with application to the moon. Journal of Geophysical Research, 68, 4545-4570.

Herman, B.M., 1964: A numerical solution to the equation of transfer for particles in the Mie region, Ph.D. dissertation, Department of Meteorology, University of Arizona, 130 pp.

Hodkinson, J.R., 1966: Particle sizing by means of the forward scattering lobe. Applied Optics, 5, 839-844.

Hovis, W.A. Jr., 1966: Infrared spectral reflectance of some common minerals. Applied Optics, 5, 245-248.

Infeld, L., 1947: The influence of the width of the gap upon the theory of antennas. Quarterly Journal of Applied Mathematics, 5, 113-132.

Kattawar, G.W., and G.N. Plass, 1968a: Radiant intensity of light scattered from clouds. Applied Optics, 7, 699-704.

Kattawar, G.W., and G.N. Plass, 1968b: Influence of particle size distribution on reflected and transmitted light from clouds. Applied Optics, 7, 869-878.

Korn, G.A., and T.M. Korn, 1968: Mathematical Handbook for Scientists and Engineers, New York, McGraw-Hill Book Co., 1130 pp.

Kozlov, V.P., and E.O. Federova, 1962: The spatial distribution of brightness in the lower deck clouds. Bulletin of the Academy of Sciences, U.S.S.R., Geophysics Series, No. 7, 619-620.

List, R.J., 1963: Smithsonian Meteorological Tables, Washington, D.C., Smithsonian Institution, Sixth Revised Edition, 527 pp.

Lowan, A.N., 1948: Table of scattering functions for spherical particles. Applied Mathematics Series No. 4, Washington, D.C., U.S. Department of Commerce, National Bureau of Standards.

MacDonald, T.H., 1951: Some characteristics of the Eppley pyrheliometer. Monthly Weather Review, 79, 153-159.

Mason, B.J., 1957: The Physics of Clouds, Oxford, Clarendon Press, 481 pp.

Middleton, W.E.K., and A.G. Mungall, 1952: The luminous directional reflectance of snow. Journal of the Optical Society of America, 42, 572-579.

Mie, G., 1908: Beigrage zur optik truber medien speziell kolloidaler metallosungen. Annalen der Physik, 25, 377-445.

Minnaert, M., 1954: The Nature of Light and Colour in the Open Air, New York, Dover Publications Inc., 362 pp.

Neiburger, M., 1949: Reflection, absorption, and transmission of insolation by stratus clouds. Journal of Meteorology, 6, 98-104.

_____, and C.W. Chien, 1960: Computations of the growth of cloud drops by condensation using an electronic computer. Physics of Precipitation, Geophysical Monograph No. 5, Washington, D.C., American Geophysical Union, pp. 191-210.

_____, and W.G. Wurtele, 1949: On the nature and size of particles in haze, fog, and stratus of the Log Angeles region. Chemical Reviews, 44, 321-335.

Okita, T., 1962: Observations of the vertical structure of a stratus cloud and radiation fogs in relation to the mechanism of drozzle formation. Tellus, 14, 310-322.

Penndorf, R., and B. Goldberg, 1956: New tables of Mie scattering functions for spherical particles. Geophysical Research Papers No. 45, Parts 1-6, U.S. Air Force Cambridge Research Center, Geophysics Research Directorate.

Plass, G.N., and G.W. Kattawar, 1968: Monte Carlo calculations of light scattering from clouds. Applied Optics, 7, 415-419.

Raschke, E., and M. Pasternak, 1967: The global radiation balance of the earth atmosphere system obtained from radiation data of the meteorological satellite NIMBUS II. Preliminary report X-622-67-383, Goddard Space Flight Center, Greenbelt, Maryland, 19 pp.

Ruff, I., R. Koffler, S. Fritz, J.S. Winston, and P.K. Rao, 1968: Angular distribution of solar radiation reflected from clouds as determined from TIROS IV radiometer measurements. Journal of the Atmospheric Sciences, 25, 323-332.

Sekera, Z., 1955: Scattering matrix for spherical particles and its transformation. Los Angeles, University of California, Department of Meteorology, Final Report, Contract No. AF 19(122)-239, Appendix D, 15 pp.

_____, 1957: Polarization of skylight. Handbuch der Physik, 48, 288-328.

Selcuk, V., and J.I. Yellott, 1962: Measurement of direct, diffuse and total radiation with silicon photovoltaic cells. Solar Energy, 6, 155-163.

Shifrin, K.S., 1968: Scattering of Light in a Turbid Medium, NASA Technical Translation, NASA TT F-477, Washington, D.C., National Aeronautics and Space Administration, 212 pp.

_____, and A.Y. Perelman, 1966: Determination of particle spectrum of atmosphere aerosol by light scattering. Tellus, 18, 566-572.

Sobolev, V.V., 1963: A Treatis on Radiative Transfer, Princeton, D. Van Nostrand Company, 317 pp.

Stratton, J.A., 1941: Electromagnetic Theory, New York, McGraw-Hill Book Company, 615 pp.

Study Conference on the Global Atmospheric Research Programme, Stockholm, 28 June - 11 July 1967, A report to the ICSU/IUGG and the World Meteorological Organization by the Committee on Atmospheric Sciences, B. Bolin, chairman, 144 pp.

Tverskoi, P.N., 1965: Physics of the Atmosphere, Jerusalem, Israel Program for Scientific Translations, 560 pp.

Twomey, S., H.B. Howell, and H. Jacobwitz, 1967: Light scattering by cloud layers. Journal of the Atmospheric Sciences, 24, 70-79.

Van Bladel, J., 1964: Electromagnetic Fields, New York, McGraw-Hill Book Company, pp. 259-267.

Van de Hulst, H.C., 1957: Light Scattering by Small Particles, New York, John Wiley and Sons, Inc., 470 pp.

Viezee, W., and P.A. Davis, 1965: Evidence of dependence of reflected solar radiation on viewing geometry in a TIROS IV radiation-data sample. Journal of Applied Meteorology, 4, 637-640.

APPENDIX

FURTHER REFLECTANCE RESULTS OVER VARIOUS SURFACES

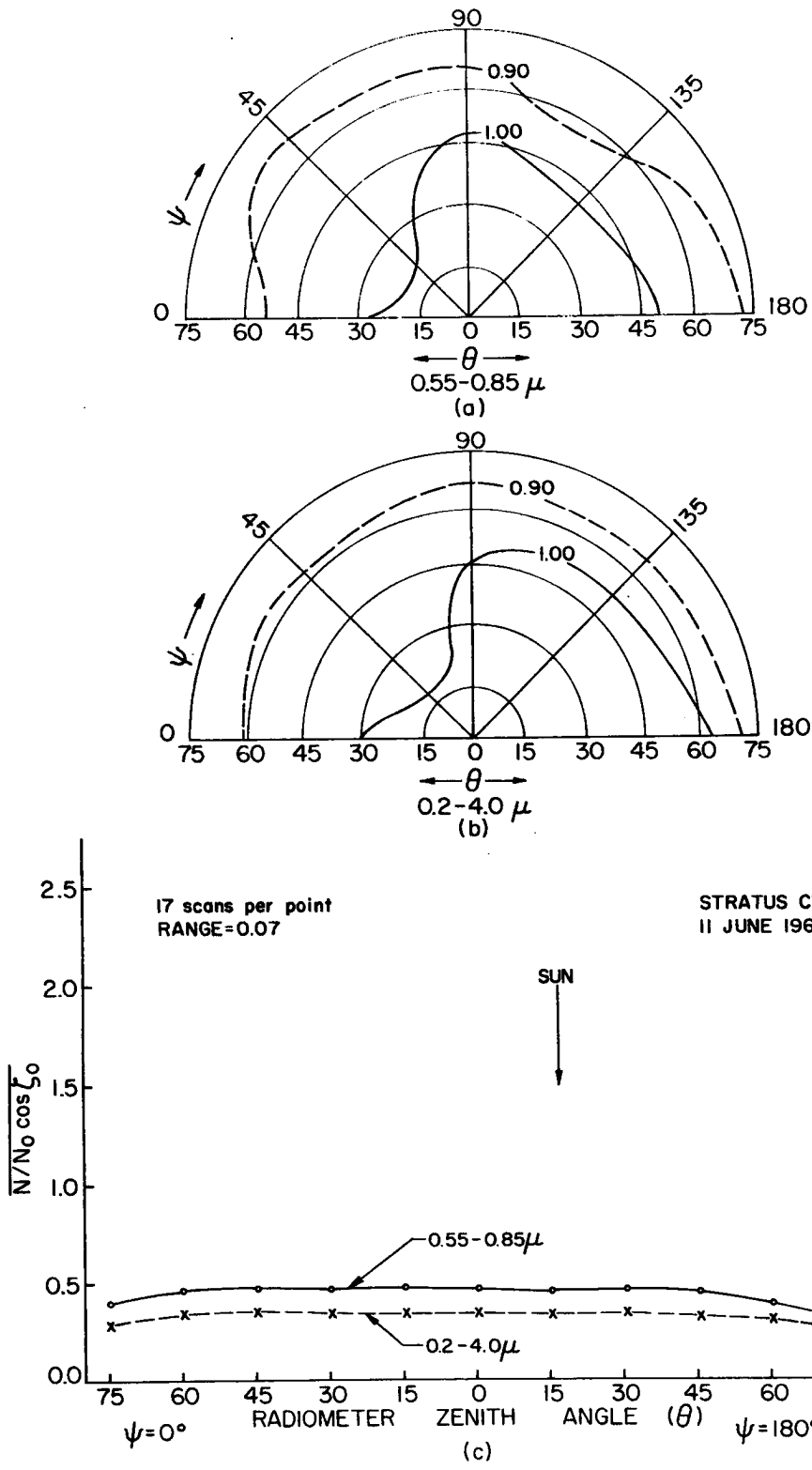

Fig. A.1. Same as Fig. 1.5.1 except that the reflectances are over stratus clouds near San Francisco, California, on 11 June 1965, 1146-1226 PST (ζ_0=16-17^0).

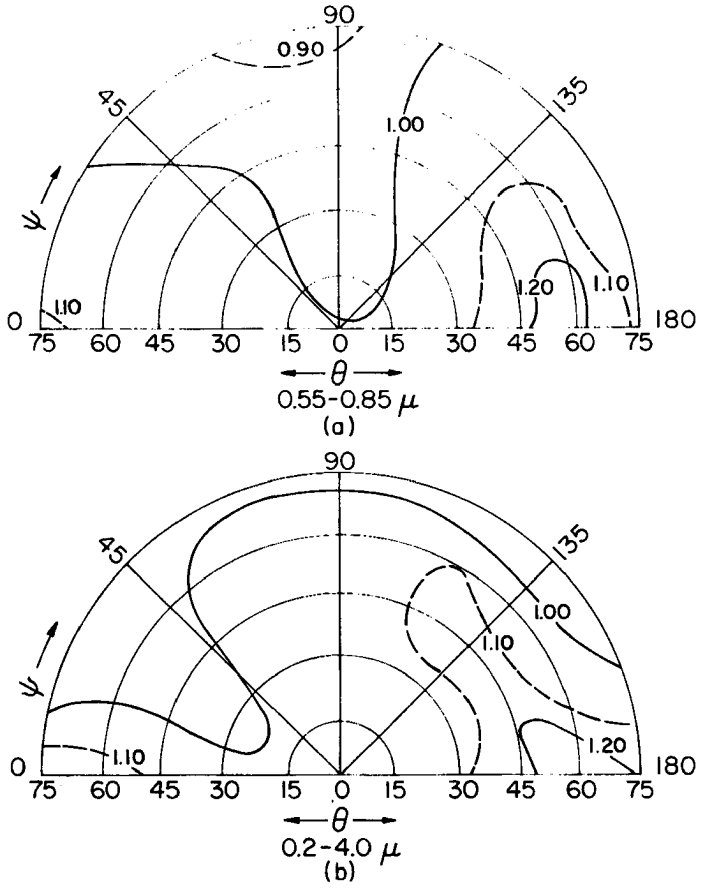

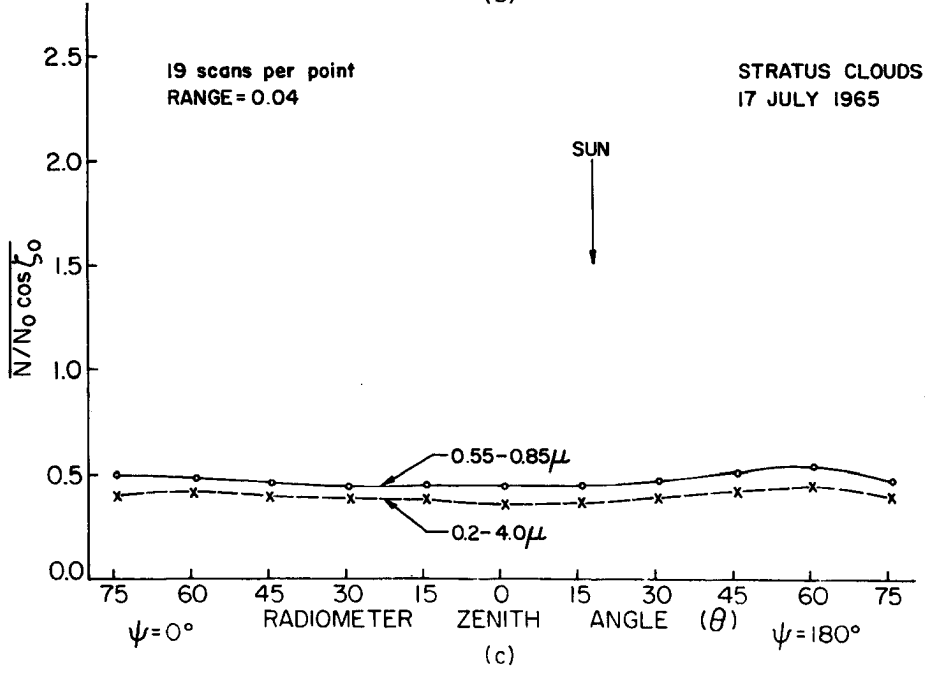

Fig. A.2. Same as Fig. 1.5.1 except that the reflectances are over stratus clouds near San Francisco, California, on 17 July 1965, 1137-1225 PST (ζ_o=17-18°).

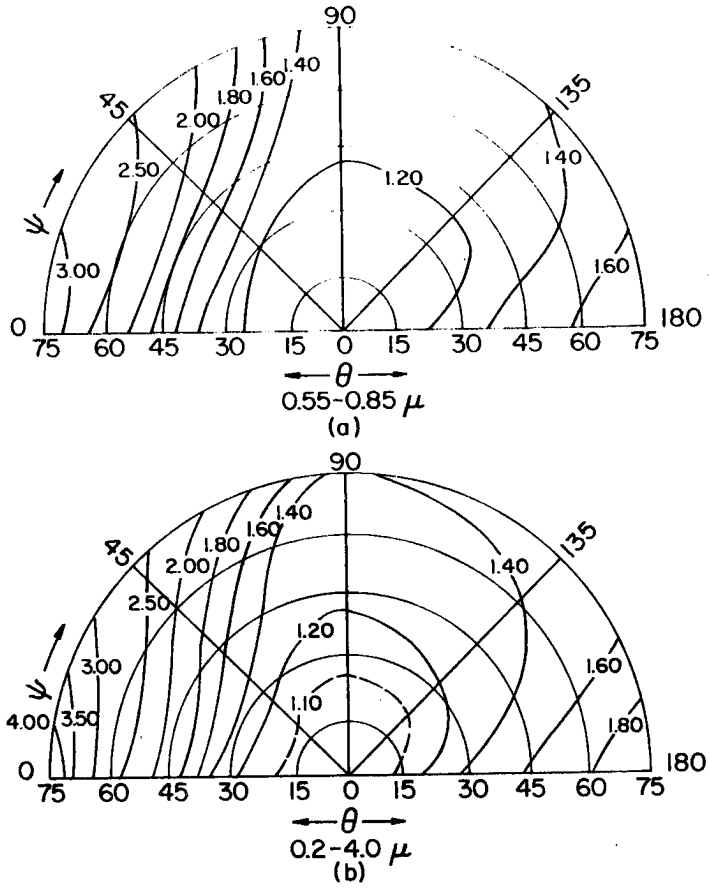

Fig. A.3. Same as Fig. 1.5.1 except that the reflectances are over stratus clouds near San Francisco, California, on 11 June 1965, 0646-0734 PST (ζ_o=58-68°).

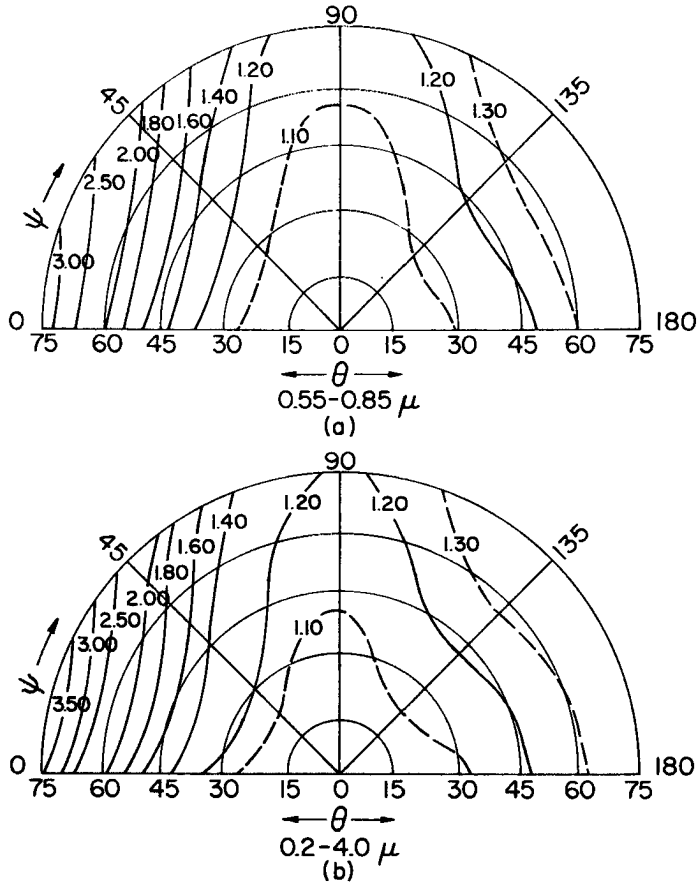

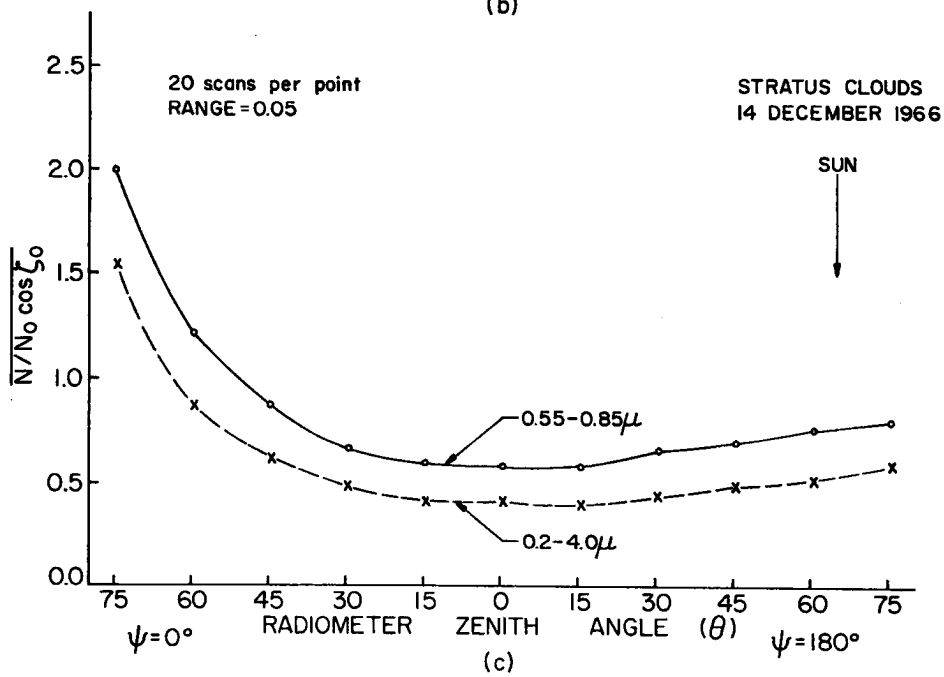

Fig. A.4. Same as Fig. 1.5.1 except that the reflectances are over stratus clouds near Bakersfield, California, on 14 December 1966, 1352-1415 PST (ζ_o=63-66°).

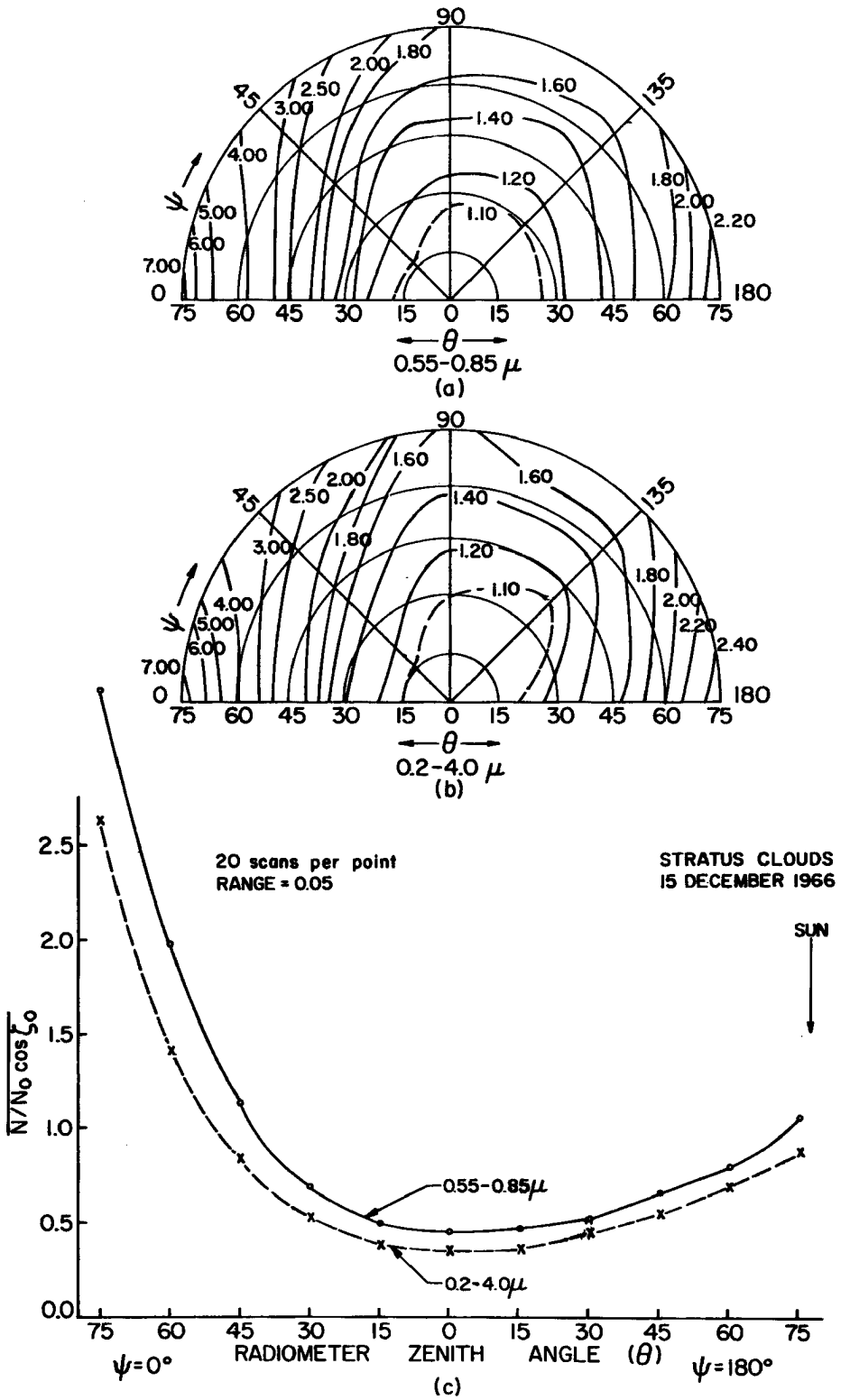

Fig. A.5. Same as Fig. 1.5.1 except that the reflectances are over stratus clouds near Bakersfield, California, on 15 December 1966, 0818-0839 PST (ζ_o=76-79°).

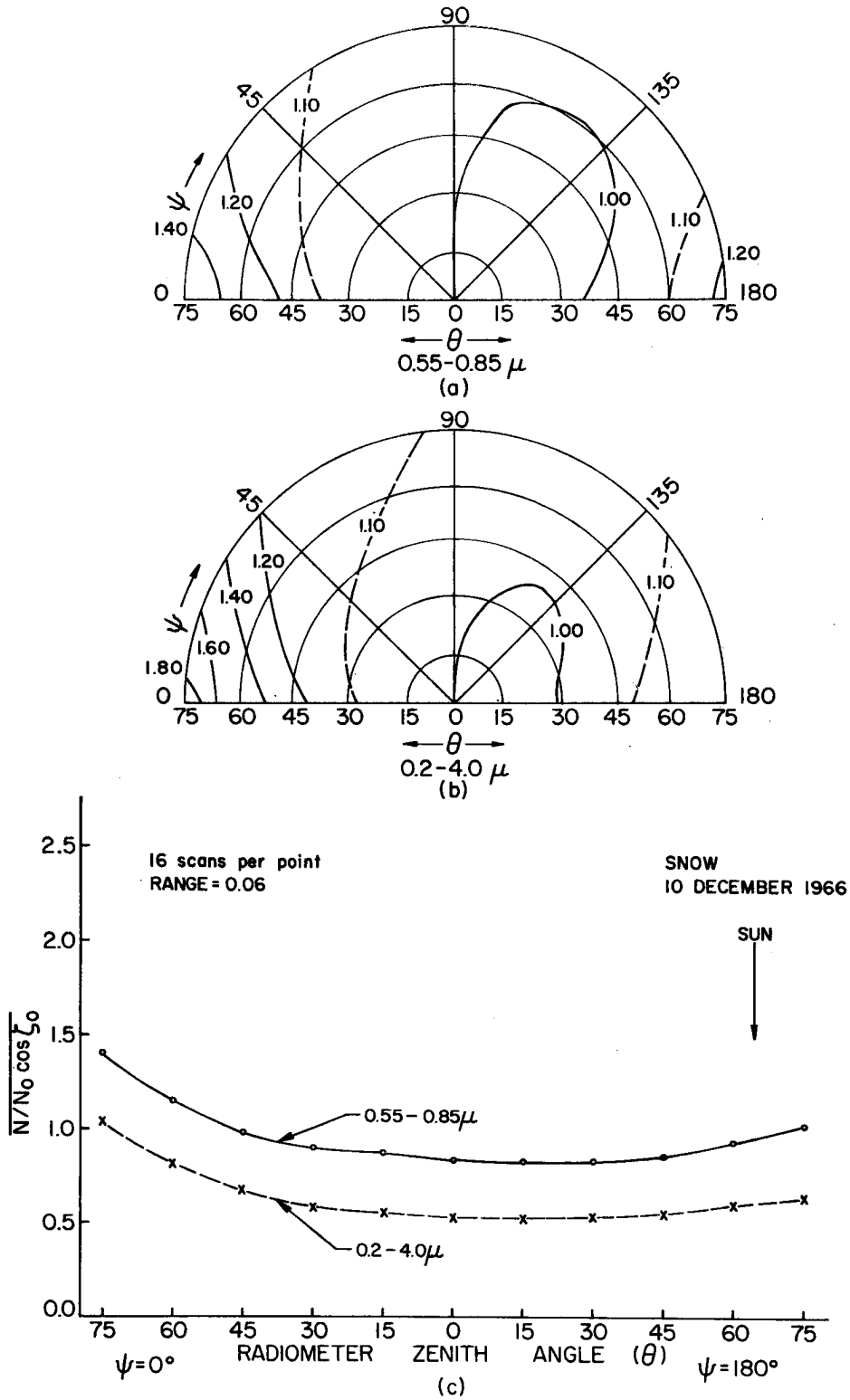

Fig. A.6. Same as Fig. 1.5.1 except that the reflectances are over snow near Laramie, Wyoming, on 10 December 1966, 1040-1112 MST (ζ_o=63-65^o).

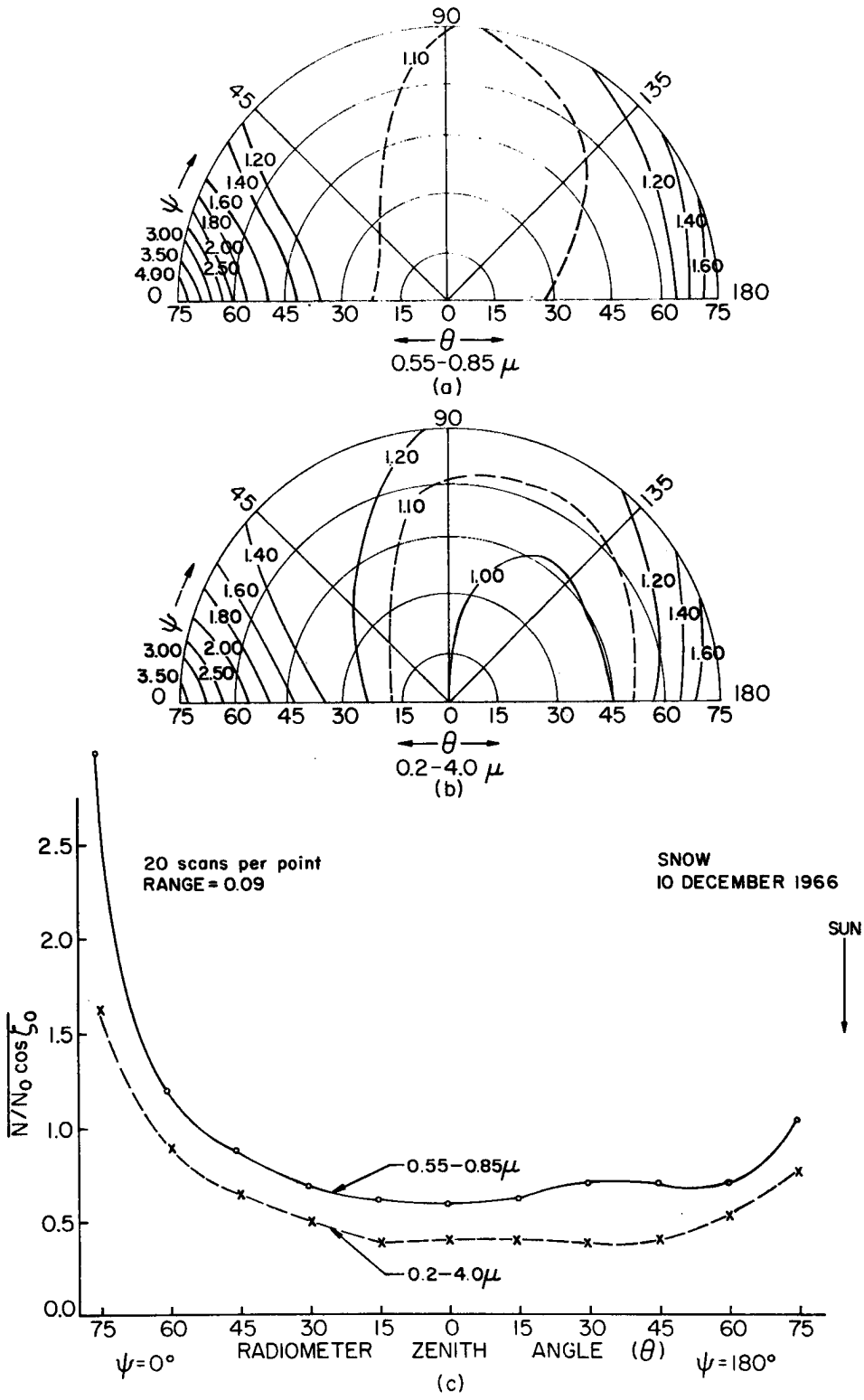

Fig. A.7. Same as Fig. 1.5.1 except that the reflectances are over snow near Laramie, Wyoming, on 10 December 1966, 0715-0818 MST (ζ_o=82-86°).

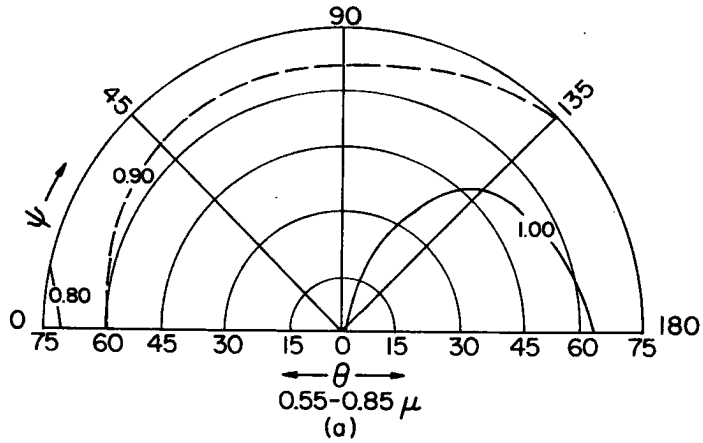

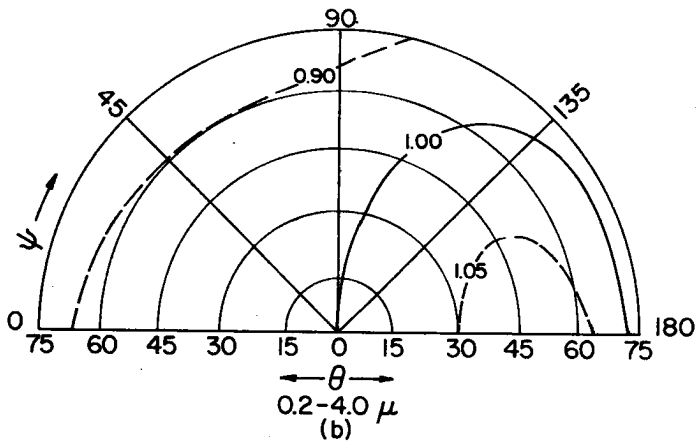

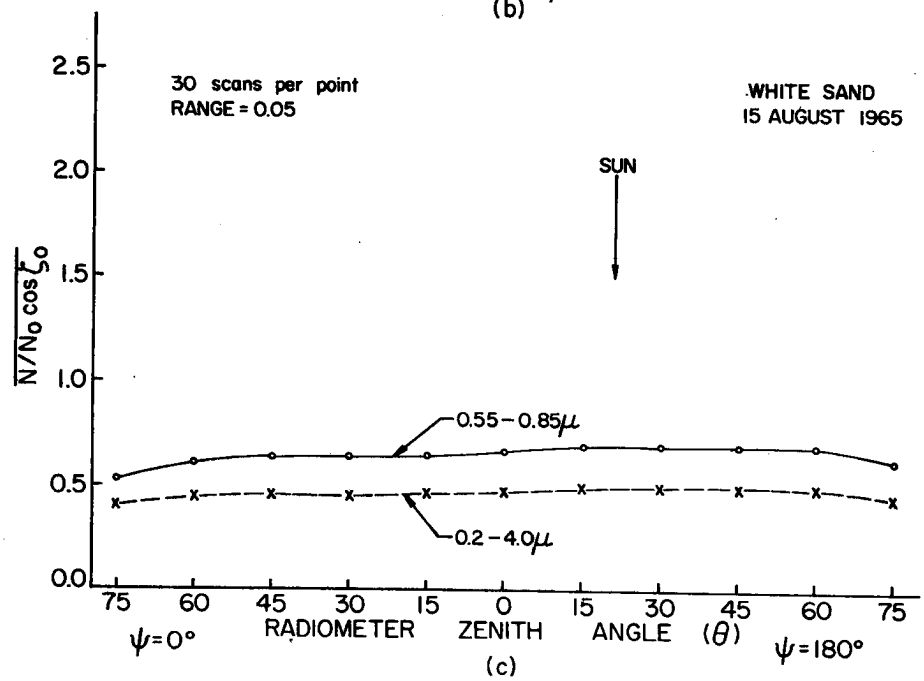

Fig. A.8. Same as Fig. 1.5.1 except that the reflectances are over white gypsum sand near Alamogordo, New Mexico, on 15 August 1965, 1120-1153 MST (ζ_o=20-22°).

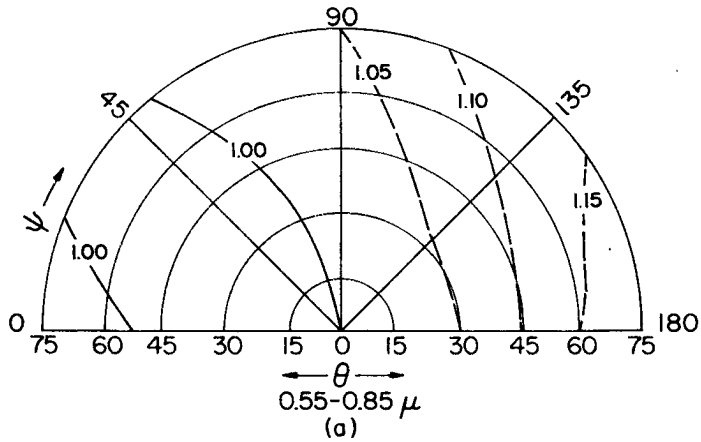

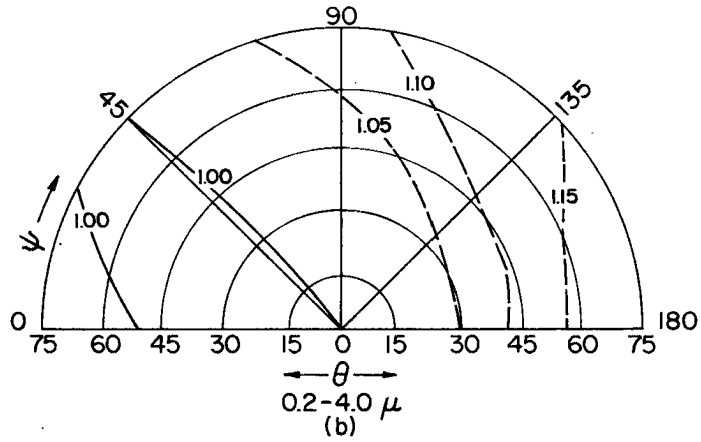

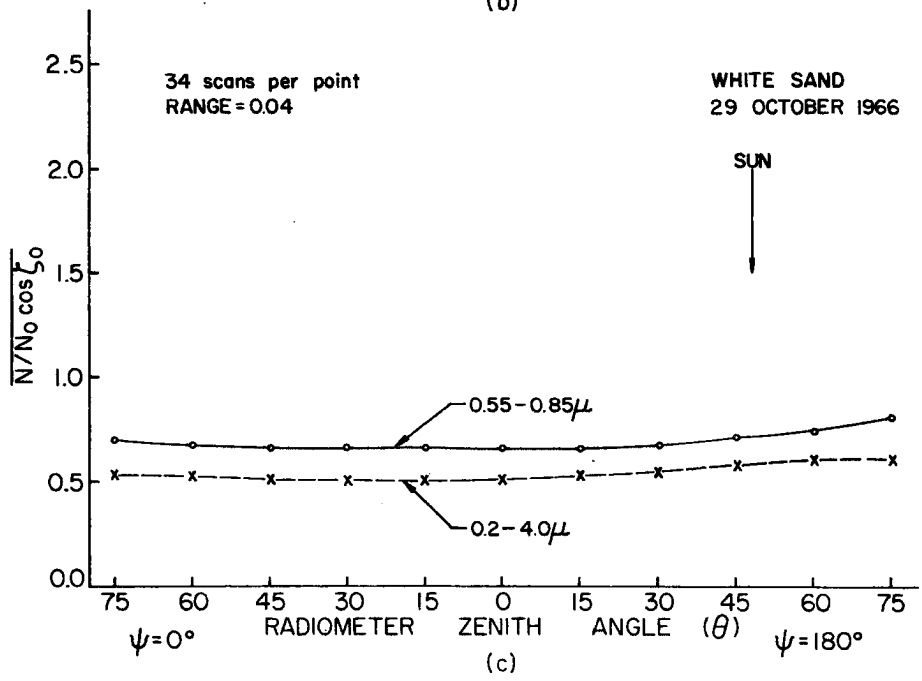

Fig. A.9. Same as Fig. 1.5.1 except that the reflectances are over white gypsum sand near Alamogordo, New Mexico, on 29 October 1966, 1155-1231 MST (ζ_0=47-49°).

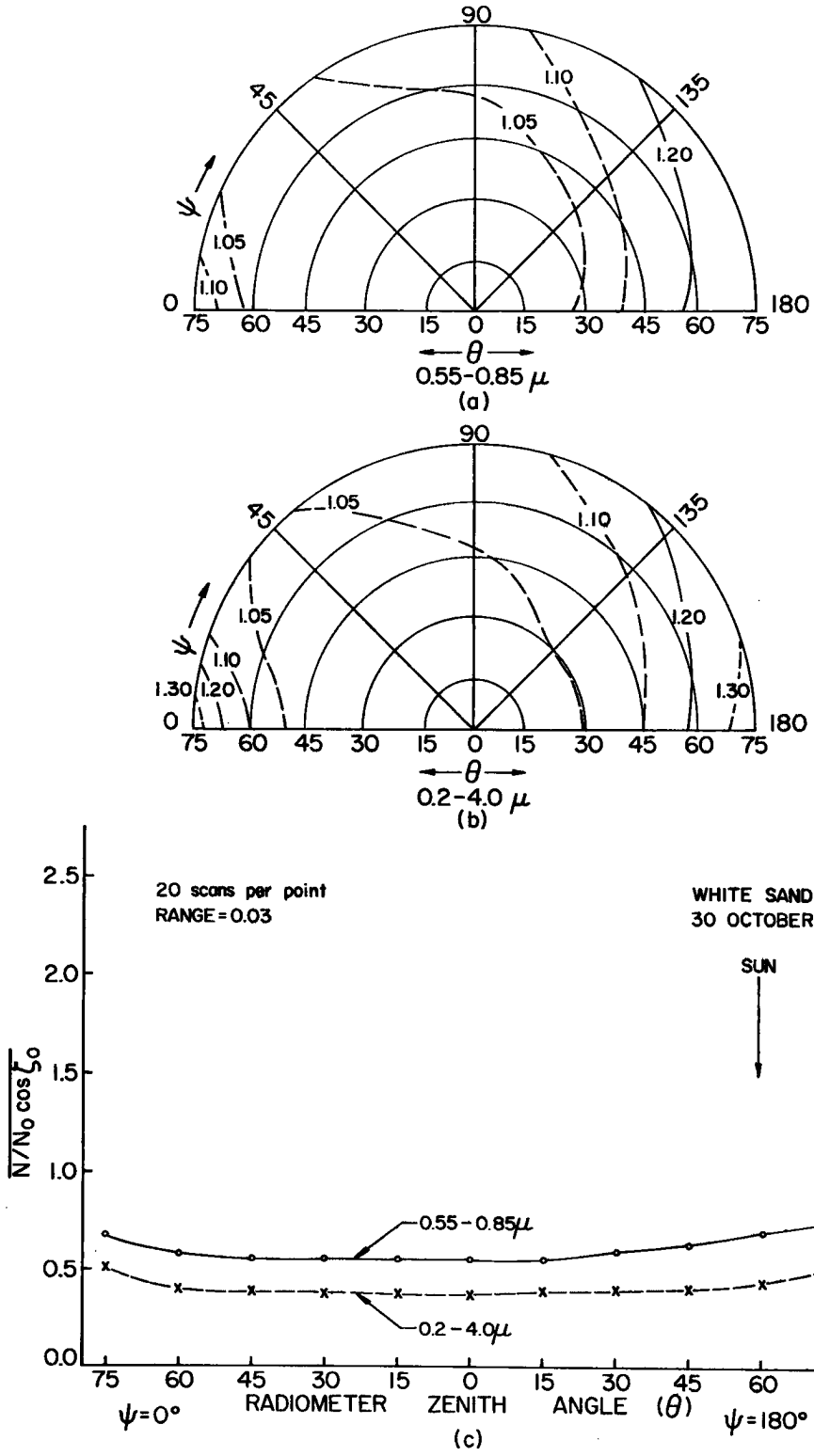

Fig. A.10. Same as Fig. 1.5.1 except that the reflectances are over white gypsum sand near Alamogordo, New Mexico, on 30 October 1966, 0913-0939 MST (ζ_o=47-49°).

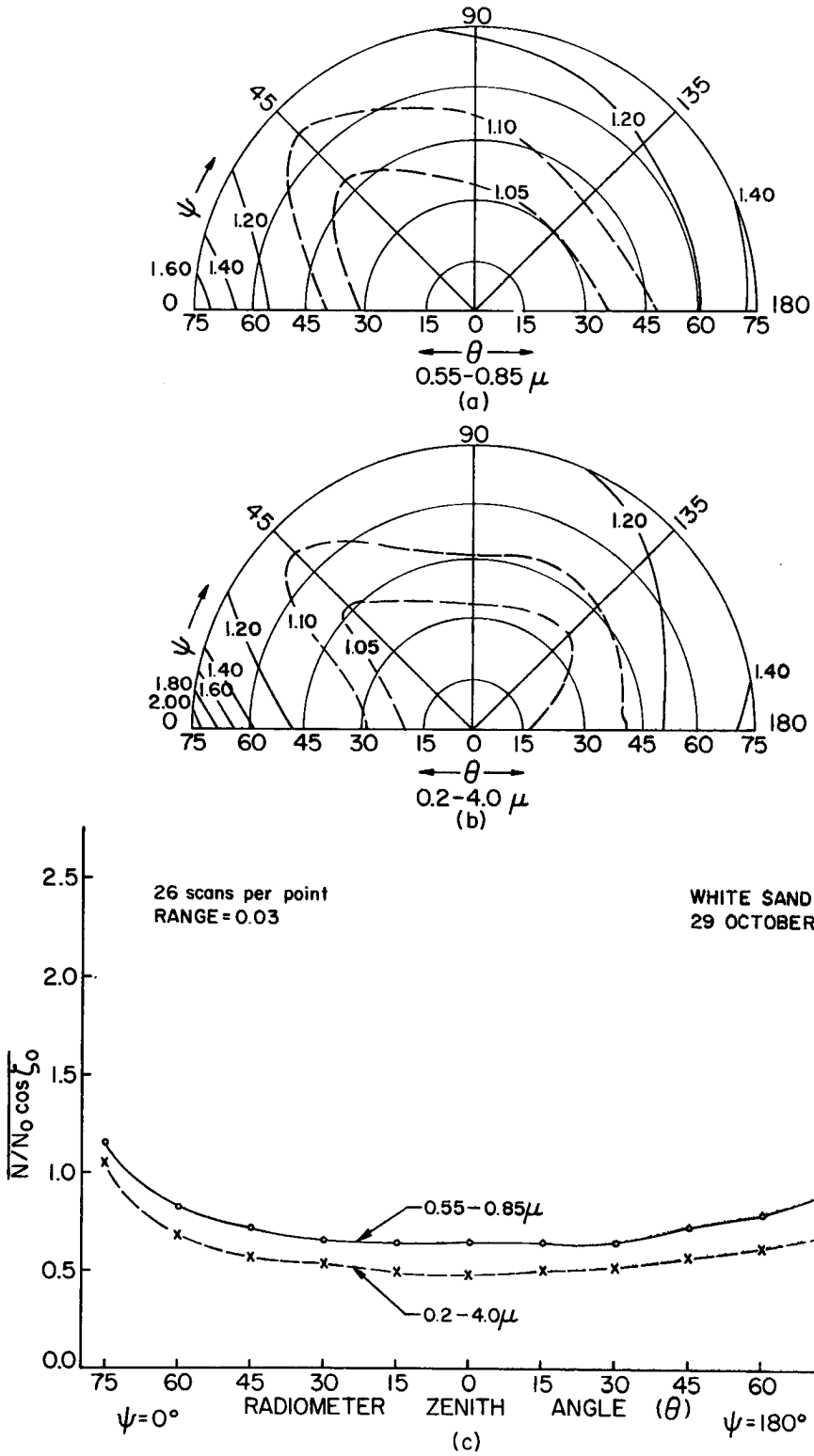

Fig. A.11. Same as Fig. 1.5.1 except that the reflectances are over white gypsum sand near Alamogordo, New Mexico, on 29 October 1966, 0706-0749 MST (ζ_o=76-82°).

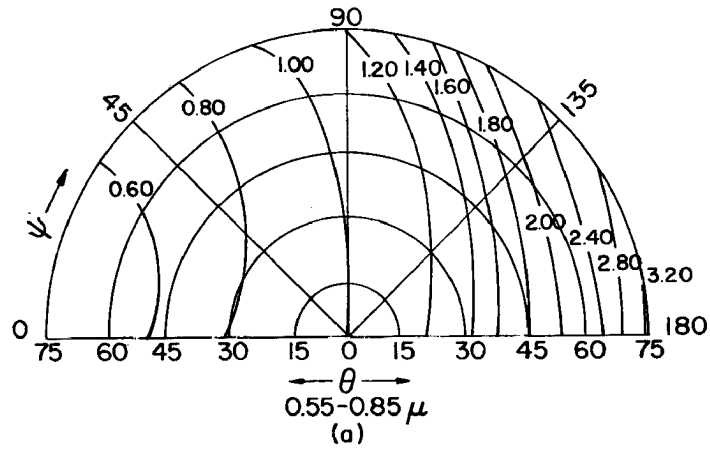

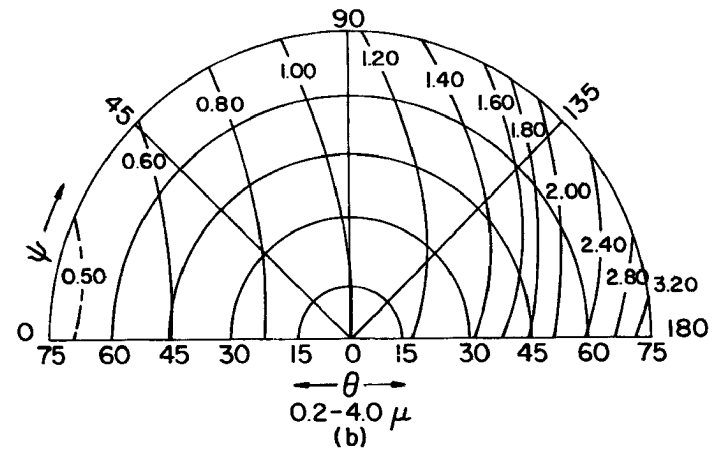

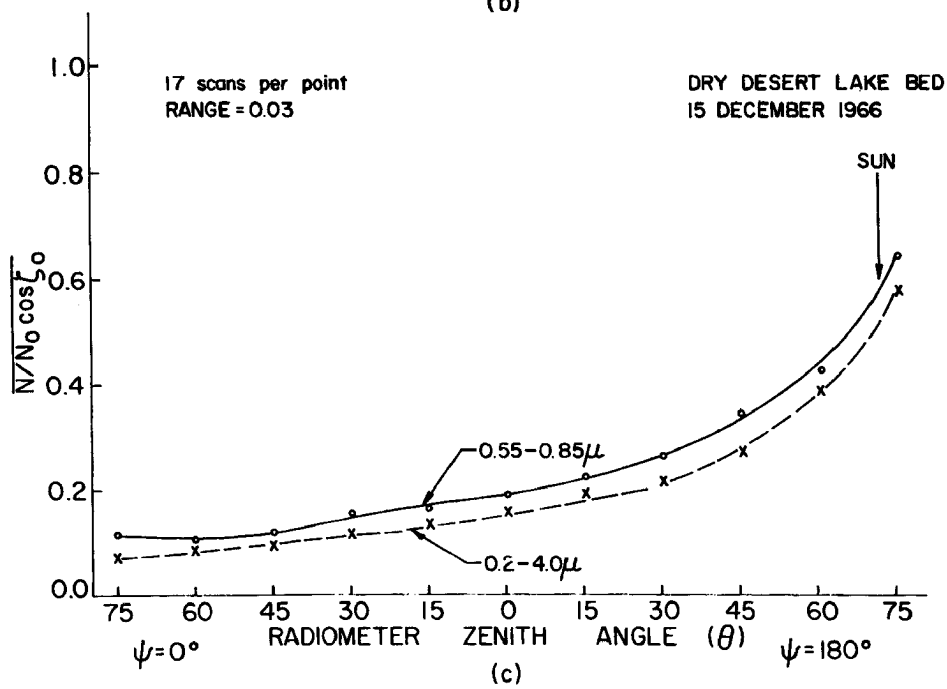

Fig. A.12. Same as Fig. 1.5.1 except that the reflectances are over Bristol Lake, northeast of Twenty-nine Palms, California, on 15 December 1966, 1445-1504 PST (ζ_0=70-73°).

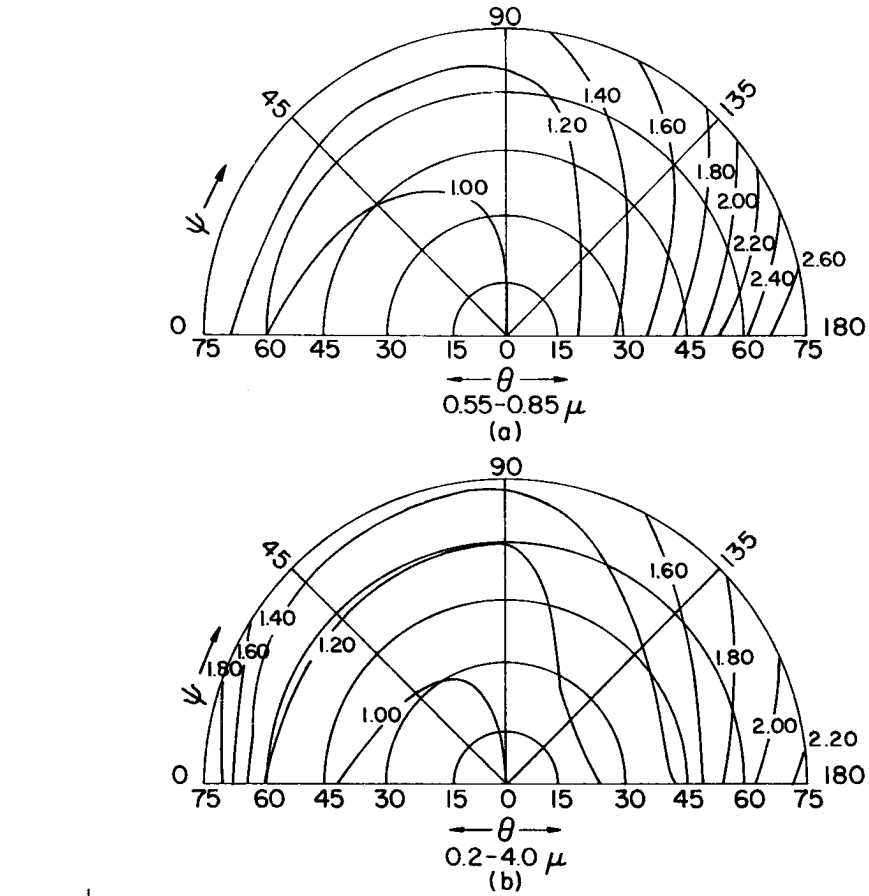

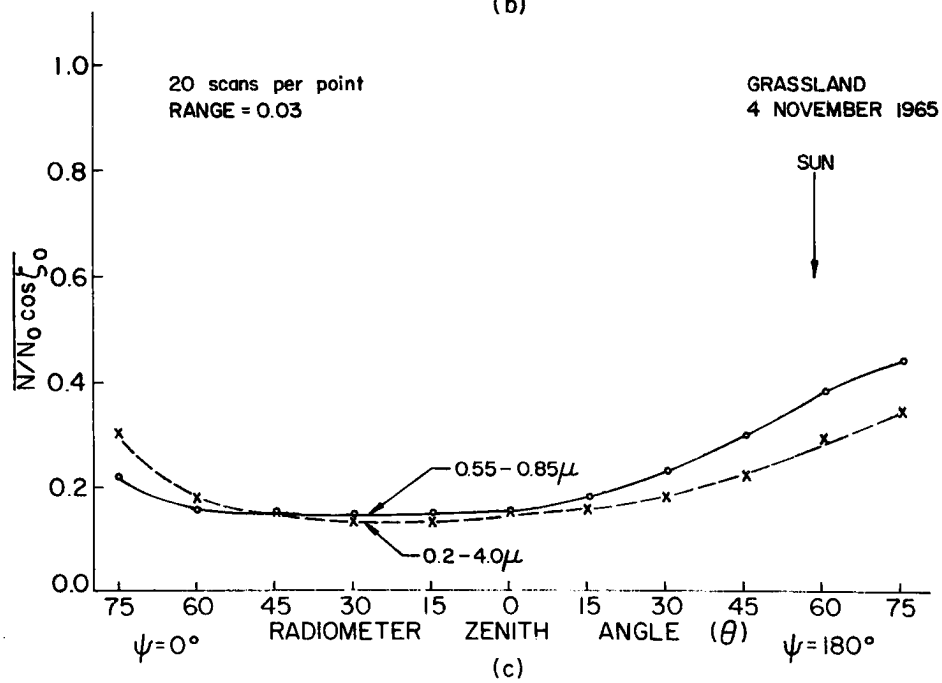

Fig. A.13. Same as Fig. 1.5.1 except that the reflectances are over a grassland-sod surface near Briggsdale, Colorado, on 4 November 1965, 1253-1316 MST (ζ_0=57-59°).

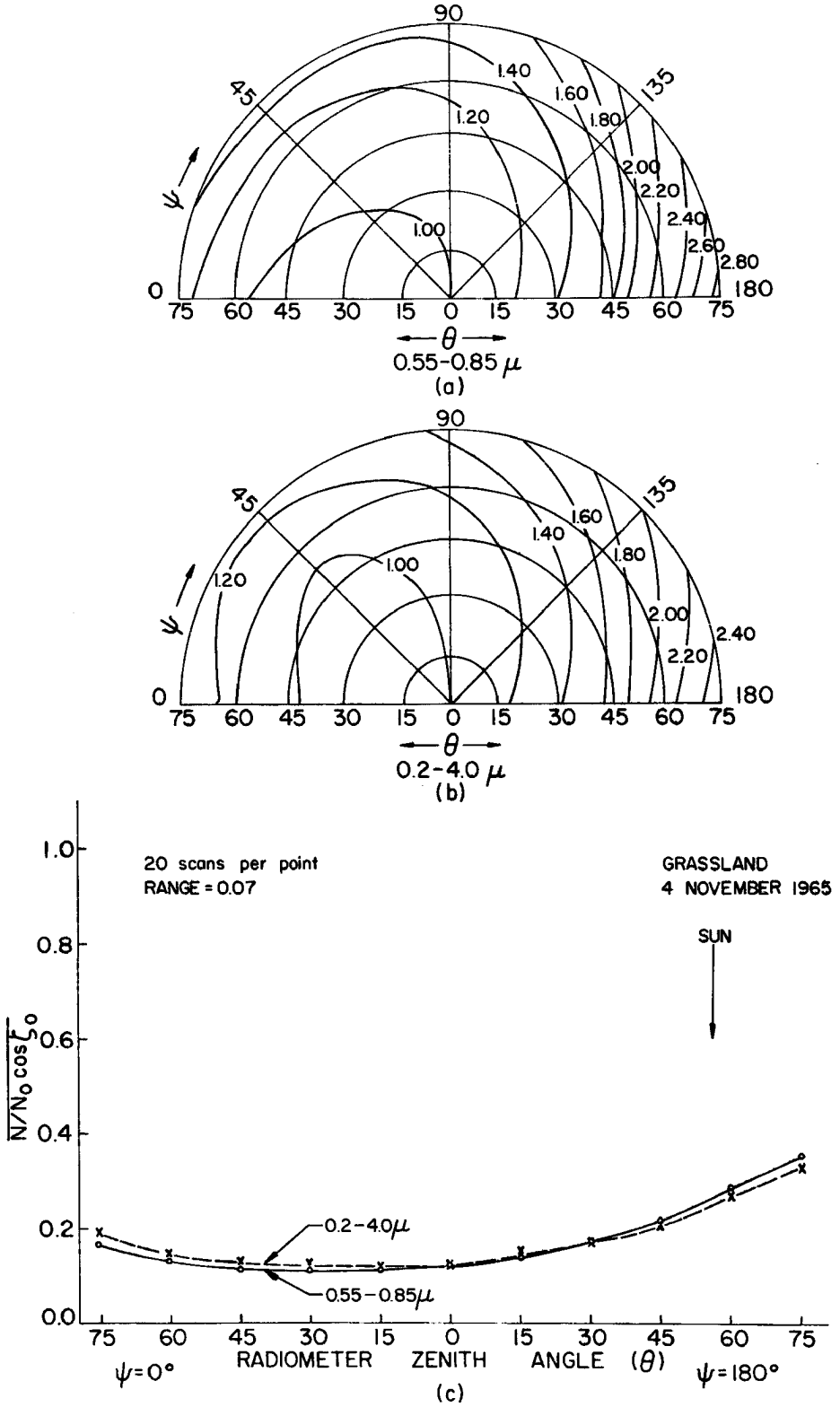

Fig. A.14. Same as Fig. 1.5.1 except that the reflectances are over a grassland-sod surface near Briggsdale, Colorado, on 4 November 1965, 1337-1354 MST (ζ_0=55-57°).

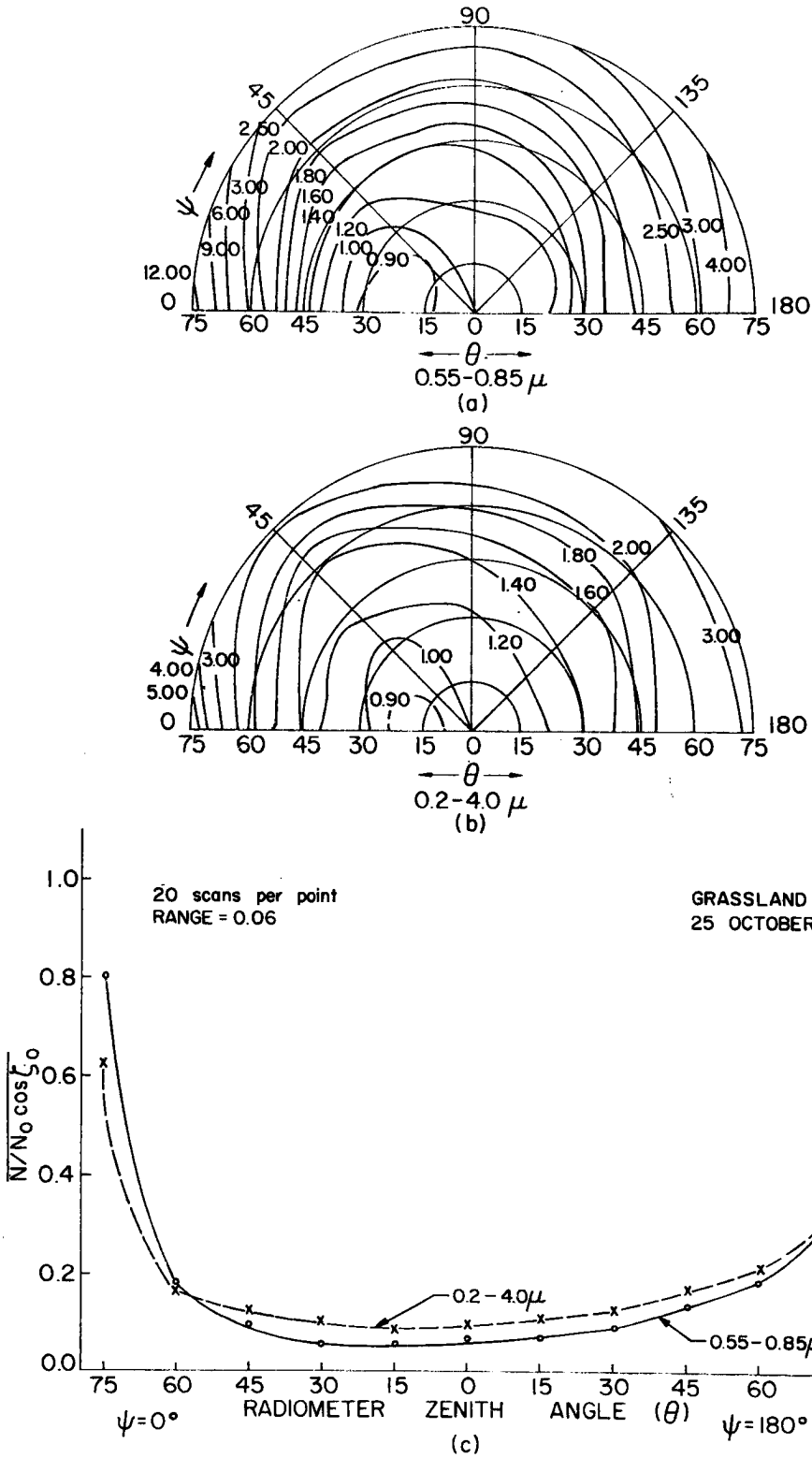

Fig. A.15. Same as Fig. 1.5.1 except that the reflectances are over a grassland-sod surface near Briggsdale, Colorado, on 25 October 1966, 1606-1630 MST (ζ_0=78-82°).

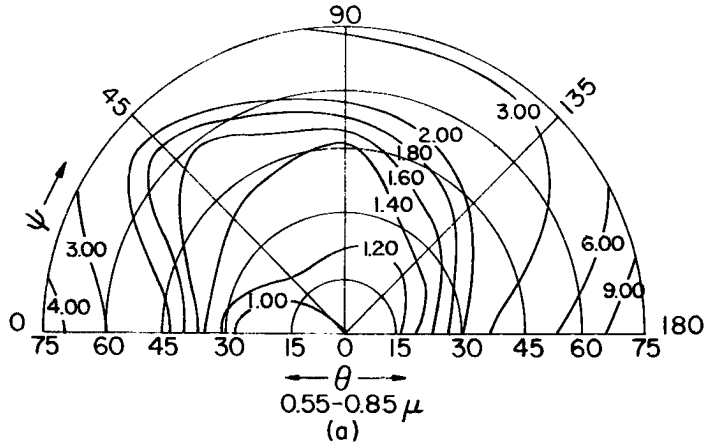

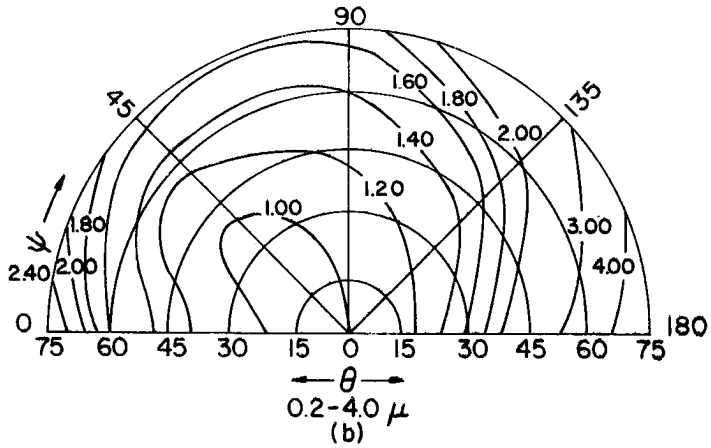

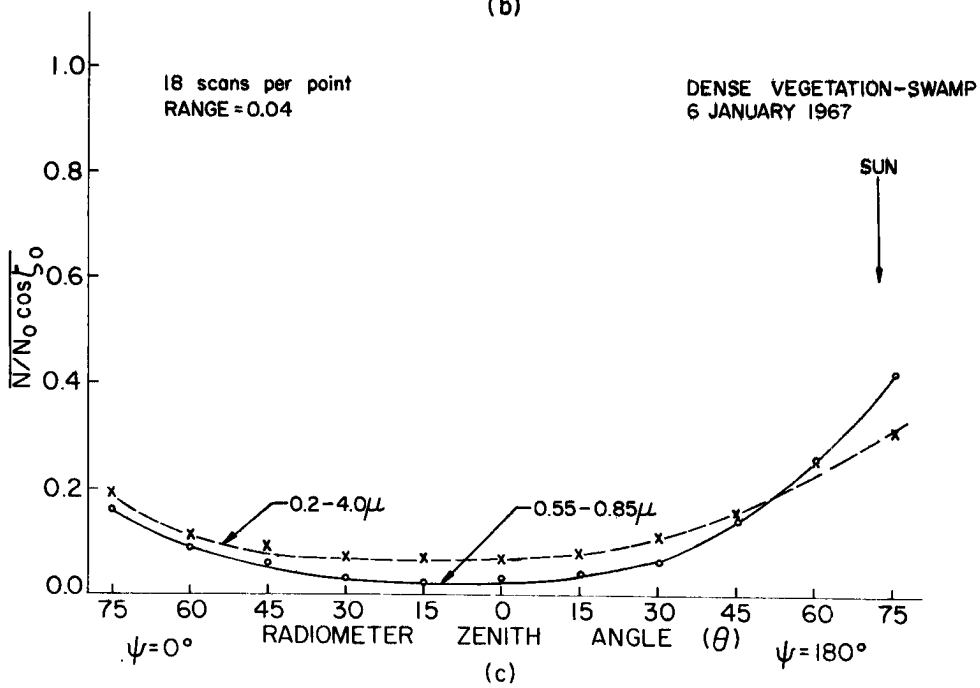

Fig. A.16. Same as Fig. 1.5.1 except that the reflectances are over a swampy, dense vegetation surface near Tallahassee, Florida, on 6 January 1967, 1555-1617 EST (ζ_o=70-73°).